労災疾病臨床研究事業費補助金

革新的高次脳機能治療法の樹立　（１４０５０１０１）

平成27年度　総括・分担研究報告書

研究代表者　石内　勝吾

平成２８（２０１６）年　５月

目　　次

Ⅰ.労災疾病臨床研究事業費補助金
（総括）研究報告書

革新的高次脳機能治療法の樹立に関する研究

研究代表者 石内 勝吾

研究要旨　革新的な高次脳機能障害の診断法と治療の労災補償行政の施策等への活用の可能性を目的に抜本的な高次脳機能障害に対する治療法の樹立に向けて,大脳･小脳を含む神経回路網の機能的ネットワークの再生と同時に海馬機能の回復が重要とする我々の仮説に基づき､脳機能イメージングの手法を駆使して大規模ネットワーク内での相互作用の解析と同時によりスケールダウンした海馬体に焦点を絞った研究を行った。

平成２７年度は fMRI 対応 EEG system (EGI 社) を用いて 75 症例 (86 解析) 海馬課題 804 症例の解析を施行した。tDCS 施行症例は重度及び中等度の海馬機能障害症害例 12 例を含む 30 症例に行い､非競合的なＮＭＤＡ受容体拮抗薬を用いた高次機能障害患者に対する薬物療法は 30 名に施行した。その結果､海馬神経新生能が途絶した海馬機能障害分類で重度障害(grade III)の患者においても顕著なスコアの改善が認められ情報処理速度、注意機能、遂行機能などの高次脳機能の回復が随伴した。これ等の所見はヒトにおいて白質伝導速度の回復､実行系を司る複数の神経回路網のネットワーク機能の回復が示唆される。臨床研究からは,薬物療法、経頭蓋刺激療法 (tDCS)ともに有害事象は発生しておらず高次脳機能障害患者に対するこれ等療法の効果と安全性を確認するため 28 年度はランダム化臨床試験を準備する。同時に fMRI－EEG 解析から導き出された海馬機能の新たなバイオマーカーN1000 についてもその臨床的有用性の検証を行う。

研究分担者氏名・所属研究機関名及び所属研究機関における職名

菅原健一・琉球大学医学部・講師
渡邉孝・琉球大学医学部・講師
外間洋平・琉球大学医学部・助教
西村正彦・琉球大学医学部・助教
土田幸男・琉球大学医学部・特命助教
宇杉竜一・琉球大学医学部・大学院生

Ａ．研究目的

本研究の目的は労災による1) 交通事故, 転倒・転落事故等によるびまん性軸索損傷, 2) 過労により発症した心筋梗塞や脳卒中による低酸素脳症 3) 炭塵爆発事故による遷延化した一酸化中毒を対象に疾患により引き起こされた高次脳機能障害の革新的な治療法の確立を目的にする。

Ｂ．研究方法

本研究では高次脳機能障害を小脳と海馬および前頭前野を含む神経回路網のネットワーク障害として捉える仮説を提示する(*Cerebellum 2015*)。高性能3T MRIを用いて安静時脳活動を評価しまた神経回路網の形態を拡散テンソル画像を用いて視覚化した。これらの基盤情報に基づいて経頭蓋直流電流刺激法と薬物療法を組み合わせる最新のニューロリハビリを施行する事で海馬の神経新生能を促進し，同時に小脳・大脳・脳幹の神経回路網を修復し脳の可塑性を高めることで高次機能の革新的な回復を実現することを目的とした。さらに治療効果は独自に開発した海馬機能評価法を応用して機能的な磁気共鳴画像（ fMRI ）を用いてリアルタイムにモニタリングした。

海馬機能評価法にて海馬新性能低下判明した場合は脳の可塑性を高める方法として安全性が高く汎用性,効果も高いtDCS(transcranial Direct current stimulation)（DC-STIMULATOR Plus;neuroConn）を用い安全性が確立している１日１回1mA, 30分間まで左側DLPFC(dorsolateral prefrontal cortex)を陽極刺激し右側DLPFCに陰極電極を留置し１クール５回とし，最大２クールまで施行した。

尚、海馬機能は機能的磁気共鳴画像（3T Discovery,GE社）による独自に開発したLure taskを用いて海馬パターン分離及びパターン補完を評価する事で神経新生能力を４段階で評価した。最も重症なのは神経新生能が途絶したGrade IIIで経頭蓋的電気刺激法や薬物による賦活治療の適応となる。これにより神経新生の促進が期待できる。Grade II は神経新生能の途絶はしていないが機能低下が１ヶ月以上継続している患者で内服薬や経頭蓋的電気刺激法の適応である。Grade Iは1ヶ月以内の最近の新生機能低下が示唆されライフスタイル等の改善で根本原因を除去するだけで回復が期待できる。Grade0 は新生機能が正常範囲にあるタイプである。

本研究は患者の脳機能解析・神経心理解析に対して倫理を重んじ患者利益を損ない事の無いよう配慮を行なうとともに琉球大学倫理委員会の承認を受け、患者本人、およびその家族に対して十分な説明を行い書面にて同意を得ている。尚、本研究では非競合的な NMDA 受容体拮抗薬 memantine 5mg または 10mg 1 日１回の内服を原則とした。

Ｃ．研究結果

本年度紹介された高次脳機能障害患者は 223 例です。その内訳は頭部外傷 14 例(6%)，脳血管障害 15 例(7%)，脳腫瘍 158 例(71%)，その他 36(16%)例であった。高次脳機能障害を認めた患者は 57 名であり、内訳としては、頭部外傷（4 名：7 %）脳血管障害（6 名：11 %）、頭部外傷（4 名：7 %）、脳腫瘍（43 名：75 %）、その他（神経梅毒 2 名、血管炎 1 名、脳症 1 名：7 %）であった。当科では全般性認知スクリーニング検査として MMSE（Mini-mental state examination）、記憶機能評価に HDS-R（長谷川式簡易知能評価スケール）、情報処理速度評価に WAIS-R の Digit symbol test、注意・作業記憶の評価に WAIS-R の Digit span test、遂行機能評価に Trail Making Test、Stroop test、視空間構成機能評価に WAIS-R の

Block test、Cube copying test を用いた評価を実施し MMSE、HDS-R においてはカットオフ値以下、Digit span test、Digit symbol test、Trail making test 、Stroop test においては－2SD 以下の成績を認知機能の低下と定義している。高次脳機能障害患者の各認知領域の低下の様相をまとめたところ、遂行機能の低下が最も多く（28 人：49 %)、次いで情報処理速度の低下（24 人：42 %)、視空間構成機能の低下（23 人：40 %)、記憶機能の低下（22 人：39 %)、全般性認知機能（16 人：28 %)、注意機能の低下（8 人：14 %）を示していることが明らかとなった。主な高次機能障害の症状とその頻度に関しては、前年度同様、遂行機能障害、記憶障害、失行・失認症、行動と情緒の障害を症状として多く認めている。平成 27 年度の新規治療患者数は 19 例, 平成 26 年度の 11 例と合わせての tDCS 治療患者数は 30 症例となった。16 例に対して f MRI lure task にて海馬パターン分離能(lure 正答率)及びパターン補完能(same 正答率)を評価した。また薬物療法の安全性および有効性の確認を目的に非競合的なＮＭＤＡ受容体拮抗薬 memantine を用いた高次機能障害患者に対する薬物療法は 30 名に施行し年齢 53.8±16.8 歳、男女比は 13：17 名で治療前の海馬神経新生機能は 15.4±21.4%, このうち海馬神経新生能が 0%の重度障害は 12 名でうち 7 名で顕著な改善があり, さらに tDCS を併用した 5 名に関しては改善期間が薬物療法単独（30.1±34.3%）(n=25)に比較して 72.6±23.9%（n=5)と長く、海馬新生能スコアでは tDCS 単独治療群 23.5±22.6 %tDCS+memantine 併用群 43.6±17.0%と改善した。28 年度は脳賦活学の樹立を目的に動物モデルによる基盤解析とともに、最適条件の確定を行い、ランダム化試験への準備を完了する予定である。

Ｄ．考察

今回症例を重ねヒトにおいて海馬歯状回部のシナプス機能の回復が高次脳機能障害の回復に本質的な役割を果たす可能性が示唆された。海馬神経新生機能が低下した高次脳機能障害患者のtDCS治療は左側DLPFCを陽極刺激で治療すると全例で海馬神経新生能の回復と高次脳機能の回復が得られたばかりではなく，さらに非競合的なＮＭＤＡ受容体拮抗薬memantineを用いた高次機能障害患者に対する薬物療法を併用することで grade IIIの海馬新生機能の途絶した患者群においてもヒト認知機能とりわけ記憶の根幹を形成するパターン分離能の再生を促す事が判明した。これ等の知見は, 様々な脳疾患で海馬機能に障害を受けている患者においても神経幹細胞を神経前駆細胞へ動因をする事で海馬機能の回復が図れるばかりではなく高次脳機能の賦活を実現できるという臨床的なエビデンスが得られた。

Ｅ．結論

海馬神経新生機能が低下した高次機能障害患者１１名にtDCSに左側DLPFCを陽極刺激で治療すると全例で海馬神経新生能の回復と高次脳機能の回復が得られた。非競合的なＮＭＤＡ受容体拮抗薬memantineを併用した患者群においては海馬機能の増強期間の優位な延長を認めた。新規ニューロリハビリテーションの基盤となる脳疾患による高次脳機能障害患者に対する脳賦活治

療に関する重要な知見が得られた。

Ｆ．健康危険情報

研究代表者、研究分担者等本研究事業に参画したものは特に研究環境の安全衛生面での問題はなかった。研究対象者に対しては検査時間の短縮に努めると同時にマイクロホンによる検査施行中の意思疎通に努め、予め承諾を得た上でのテレビカメラによるモニターを行い患者が安全に検査が受けられる環境の形成に努める配慮を行い有害事象の発生はない。

Ｇ．研究発表

1.　論文発表

①Cerebellar Contribution to Pattern Separation of Human Hippocampal Memory Circuits.
Shiroma A, Nishimura M, Nagamine H, Miyagi T, Hokama Y Watanabe T, Murayama S, Tsutsui M, Tominaga D & Ishiuchi S
Cerebellum (London, England) doi:10.1007/s12311-015-0726-0. 2015.

②SLC44A1-PRKCA fusion in papillary and rosette-forming glioneuronal tumors.
Nagaishi M, Nobusawa S, Matsumura N, Kono F, Ishiuchi S, Abe T, et al.
Journal of clinical neuroscience : official journal of the Neurosurgical Society of Australasia doi:10.1016/j.jocn.2015.04.021.

③A novel insulinotropic mechanism of whole grain-derived γ-oryzanol via the suppression of local dopamine D2 receptor signaling in mouse islet.
Kozuka C, Sunagawa S, Ueda R, Higa M, Ohshiro Y, Tanaka H, et al.
British journal of pharmacology doi:10.1111/bph.13236. 2015.

④Effect of caffeine contained in a cup of coffee on microvascular function in healthy subjects.
Noguchi K, Matsuzaki T, Sakanashi M, Hamadate N, Uchida T, Kina-Tanada M, et al.
Journal of pharmacological sciences 127 (2): 217-22. doi:10.1016/j.jphs.2015.01.003. 2015.

⑤Gamma-oryzanol protects pancreatic β-cells against endoplasmic reticulum stress in male mice.
Kozuka C, Sunagawa S, Ueda R, Higa M, Tanaka H, Shimizu-Okabe C, et al.
Endocrinology: en20141748. doi:10.1210/en.2014-1748. 2015.

⑥Ca2+-permeable AMPA –type glutamate receptors and glioblastomas
Ishiuchi S
Progress in Neuro-Oncology 22-2 1-8. 2015.

⑦Effect of caffeine contained in a cup of coffee on microvascular function in healthy subjects.
Noguchi K, Matsuzaki T, Sakanashi M, Hamadate N, Uchida T, Kina-Tanada M, Kubota H, Nakasone J, Sakanashi M, Ueda S, Masuzaki H, Ishiuchi S, Ohya Y, Tsutsui M.
J Pharmacol Sci. 2015 Feb;127(2):217-22.

⑧Progression of cerebellar chronic encapsulated expanding hematoma during late pregnancy after gamma knife radiosurgery for arteriovenous malformation.

Watanabe T, Nagamine H, Ishiuchi S.
Surg Neurol Int. 2014 Dec 30;5(Suppl 16):S575-9.

⑨Identification of a novel cell-penetrating peptide targeting human glioblastoma cell lines as a cancer-homing transporter.
Higa M, Katagiri C, Shimizu-Okabe C, Tsumuraya T, Sunagawa M, Nakamura M, Ishiuchi S, Takayama C, Kondo E, Matsushita M.
Biochem Biophys Res Commun. 2015 Feb 6;457(2):206-12.

⑩Development of an experimentally useful model of acute myocardial infarction: 2/3 nephrectomized triple nitric oxide synthases-deficient mouse.
Uchida T, Furuno Y, Tanimoto A, Toyohira Y, Arakaki K, Kina-Tanada M, Kubota H, Sakanashi M, Matsuzaki T, Noguchi K, Nakasone J, Igarashi T, Ueno S, Matsushita M, Ishiuchi S, Masuzaki H, Ohya Y, Yanagihara N, Shimokawa H, Otsuji Y, Tamura M, Tsutsui M.
J Mol Cell Cardiol. 2014 Dec;77:29-41.

⑪Usefulness of the apparent diffusion coefficient (ADC) for predicting the consistency of intracranial meningiomas.
Yogi A, Koga T, Azama K, Higa D, Ogawa K, Watanabe T, Ishiuchi S, Murayama S.
Clin Imaging. 2014 38:802-7.

⑫Enhanced expression of proapoptotic and autophagic proteins involved in the cell death of glioblastoma induced by synthetic glycans.
Faried A, Arifin MZ, Ishiuchi S, Kuwano H, Yazawa S.
J Neurosurg. 2014 120:1298-308.

⑬神経膠芽腫に対するAktを標的とした分子標的療法　渡邉孝，　菅原健一，長嶺英樹，石内勝吾，琉球医学会雑誌 33（1～3）1～8，2014

⑭慢性期中枢神経障害患者への経頭蓋直流電気刺激による治療介入が筋力と脳活動に及ぼす効果―シングルケースによる検討―
西村正彦，石内勝吾，沖縄県作業療法研究，
2015

⑮固有名詞漢字の音読が保たれた失読失書の１例，宇杉竜一，石内勝吾，神経心理学，2015

⑯Ibe Y, Tosaka M, Horiguchi K, Sugawara K, Miyagishima T, Hirato M, Yoshimoto Y. Resection extent of the supplementary motor area and post-operative neurological deficits in glioma surgery. Br J Neurosurg. 2016 Jun;30(3):323-9

⑰Iijima K, Hirato M, Miyagishima T, Horiguchi K, Sugawara K, Hirato J, Yokoo H, Yoshimoto Y. Microrecording and image-guided stereotactic biopsy of deep-seated brain tumors. J Neurosurg. 2015 Oct;123(4):978-88.

2.　学会発表

①石内勝吾、脳の加齢と海馬新生能-特別講演、2014年3月5日、東北大学加齢研究所

②石内勝吾、Gliomagenesis and GRIA2 – An Integrated vertical study　-from gene to disease-会長招聘講演、第５８回日本神

経化学大会、2015 年 9 月 13 日、大宮ソニックシティ
③石内勝吾、ロボットスーツHALを用いたニューロリハビリテーション-基調講演、第4回日本脳神経　HAL　研究会、2015年12月26日、京都国際会館
④石内勝吾、特別講演第16回、ブレインサイエンス研究会「分子を基盤とした神経機能と病態」、「神経幹細胞とグリオーマ遺伝子から疾患までの垂直的統合研究」、2014年6月28日、沖縄かりゆしアーバンリゾート・ナハ
⑤石内勝吾、記念講演、脳科学に基づいた脳神経外科学の発展をめざして、Development of neurological surgery based on brain science一、群馬大学医学部脳神経外科同門会講演、2014年6月21日、マーキュリーホテル前橋
⑥石内勝吾、特別講演、脳科学に基づいた脳神経外科学の発展をめざして、第8回奈良脳腫瘍研究会、2014年10月3日、スイス南海大阪
⑦石内勝吾、シンポジウム「放射線神経生物学の夜明け」、「中枢神経系への放射線照射によって生じる高次機能障害の評価及びその予防法」、第36回日本生物学的精神医学会第57回日本神経化学会合同年会、2014年9月30日、奈良県新公会堂
⑧石内勝吾、シンポジウム中枢神経系への放射線照射によって生じる高次機能障害の評価及び予防法、第73回日本脳神経外科学会学術総会、2014年10月10日、グランドプリンスホテル高輪
⑨菅原健一、金城雄生、小林繁貴、長嶺英樹、外間洋平、宮城智央、田村貴光、渡邉孝、石内勝吾、「先天性第XI因子欠損症を合併した中心前回膠芽腫の一例」、第 32 回日本脳腫学会学術集会、2014 年 11 月 30 日、シェラトン・グランデ・トーキョーベイ・ホテル（舞浜）
⑩宮城智央、小林繁貴、金城雄生、長嶺英樹、外間洋平、西村正彦、田村貴光、菅原健一、渡邉孝、石内勝吾、「3次元CG支援による脳神経外科」、第73回日本脳神経外科学会学術総会、2014年10月10日、グランドプリンスホテル高輪
⑪Katagiri C, Matsushita M, Ishiuchi S. Hyperbaric oxygenation treatment improves radioresponse in glioblastoma xenograft mouse model. The 5th International Society of Radiation Neurobiology Conference, 2015
⑫田村貴光、石内勝吾、神経線維腫症 1 型に合併した椎骨動静脈瘻の治療 1 例～再発なく長期経過良好な治療例～、第 30 回日本脳神経血管内治療学会学術総会、2014 年 12 月、パシフィコ横浜
⑬田村貴光、石内勝吾、Balloon occlusion test in carotid body tumors、第 73 回日本脳神経外科学会学術総会、2014 年 10 月、グランドプリンスホテル高輪
⑭石内勝吾、公開シンポジウム-倫理が育む健康・福祉に貢献する研究-招待講演、Neurological surgery based on brain science 2014年3月8日、OIST
⑮西村正彦、石内勝吾、「ロボットスーツ HAL 単関節上肢タイプによる上肢機能訓練の有効性について」、第 49 回日本作業療法学会、2015 年 6 月 20 日、神戸ポートピアホテル・神戸国際展示場
⑯Katagiri C. Hyperbaric oxygenation treatment prevent cellular hypoxic

response by radiotherapy in glioblastoma. The 6th international society of radiation and neurobiology conference, Oral presentation, Feb 2016, Nagasaki

⑰片桐千秋、長嶺英樹、松下正之、石内勝吾、「Hyperbaric oxygenation treatment effects on radioresponse in malignant glioblastoma.」第58回日本神経化学会大会、2015、大宮、ポスター

⑱片桐千秋、石内勝吾、「Hyperbaric oxygenation treatment effects on radioresponse in malignant glioblastoma.」第74回日本癌学会学術総会、2015、名古屋、ポスター

⑲渡邉孝、外間洋平、小林繁貴、金城雄生、石内勝吾、「成長ホルモン産生下垂体腺腫に対する内視鏡下経蝶形骨洞手術と薬物療法を併用した治療成績」、第25回　日本間脳下垂体学会、2015年2月27日、京都

⑳渡邉孝、外間洋平、小林繁貴、金城雄生、石内勝吾、「琉球大学における成長ホルモン産生下垂体腺腫に対する治療成績」、沖縄間脳下垂体腫瘍研究会、2015年4月24日

⑳渡邉孝、菅原健一、金城雄生、小林繁貴、長嶺英樹、外間洋平、宮城智央、石内勝吾、「主要硬膜静脈洞に浸潤する髄膜腫の摘出術」、日本脳神経外科学会第74回学術総会、2015年10月15日、札幌

㉑Shiroma A, Kobayashi S, Kinjo Y, Hokama Y, Miyagi T, Sugawara K, Watanabe T, Tominaga D, Ishiuchi S. Measures cognitive function predict survival in patient with high- grade glioma. The 6th International Society of Radiation Neurobiology Conference, Feb 12-13 3016, Nagasaki.

㉒Ibe Y, Tosaka M, Horiguchi K, Sugawara K, Miyagishima T, Hirato M, Yoshimoto Y. Resection extent of the supplementary motor area and post-operative neurological deficits in glioma surgery. Br J Neurosurg. 2016 Jun;30(3):323-9

㉓菅原健一、金城雄生、小林繁貴、長嶺英樹、外間洋平、宮城智央、田村貴光、渡邉孝、石内勝吾、「当院における低磁場術中MRIを併用した脳腫瘍手術」、第15回 日本術中画像情報学会、2015年6月20日、川崎

㉔菅原健一、金城雄生、小林繁貴、外間洋平、宮城智央、渡邉孝、石内勝吾、「当院における低磁場術中MRIを併用した画像誘導手術 Image-guided surgery using low field intraoperative MRI system in our hospital」、第167回琉球医学会例会、2015年10月27日、沖縄

㉕菅原健一、石内勝吾、「悪性脳腫瘍に対する術中MRIを併用した画像誘導手術」、第116回　四金会、2016年2月19日、沖縄

㉖菅原健一、金城雄生、小林繁貴、長嶺英樹、外間洋平、宮城智央、田村貴光、渡邉孝、石内勝吾、「当院における低磁場術中MRIを併用した画像誘導手術 Image-guided surgery using low field intraoperative MRI system in our hospital」、一般社団法人・日本脳神経外科学会第74回学術総会、ポスター、2015年10月14日、札幌

㉗小林繁貴, 渡邉孝, 菅原健一, 金城雄生, 長嶺英樹, 外間洋平, 石内勝吾、「術前診断に苦慮した、造影効果の乏しい

central neurocytoma の MRS 所見」、日本脳神経外科学会第 74 回学術総会、2015 年 10 月 15 日、札幌

㉘小林繁貴，菅原健一，金城雄生，上原卓実，外間洋平，宮城智央，渡邉孝，石内勝吾、「クロナゼパムが有効であった Hemiballism and hemichorea の症例」、四金会、2015 年 12 月 13 日

Ⅱ-1. 労災疾病臨床研究事業費補助金
（分担）研究報告書

革新的高次脳機能治療法の樹立に関する研究
―ニューロリハビリテーション治療の樹立―

研究分担者　　菅原健一, 渡邉孝

研究要旨：革新的高次脳機能治療法の樹立を目的に高次脳機能障害患者に対して脳の可塑性を高める方法として tDCS(transcranial Direct current stimulation)を用いて 1mA, 30 分間左側 DLPFC(dorsolateral prefrontal cortex)を標的に 3 例に直流電流刺激を施行した。全例で海馬パターン分離機能と記憶障害、注意障害等の高次脳機能障害の回復が得られた。

Ａ．研究目的

本研究の目的は労災による1) 交通事故, 転倒・転落事故等によるびまん性軸索損傷, 2) 過労により発症した心筋梗塞や脳卒中による低酸素脳症 3) 炭塵爆発事故による遷延化した一酸化中毒を対象に疾患により引き起こされた高次脳機能障害の革新的な治療法の確立を目的に経頭蓋直流電流刺激法の確立および薬物療法の安全性および有効性について探索を目的とする。

Ｂ．研究方法

脳の可塑性を高める方法としては rTMS(repetitive Transmagnetic stimulation)と tDCS(transcranial Direc current stimulation)があり本研究ではより安全性が高く汎用性,効果も高い tDCS を用いた。1mA, 30 分間左側 DLPFC(dorsolateral prefrontal cortex)を標的に陽極電極を置き、反対側右側側 DLPFC に陰極電極を留置して直流電流刺激を施行した。海馬機能評価は独自に開発した behavioral task にて非侵襲的に fMRI を用いてパターン分離能およびパターン補完能を算定し治療前後で比較検証を行いました。また BOLD 機能をパターン解析および %BOLD 変化の算定、P1 (initial positive peak), P2 (isecond positive peak), N1 (initial negative peak), N2 (second negative peak)の amplitude, latency を算定し海馬歯状回新生ニューロンのシナプス機能を評価した。

Ｃ．研究結果

平成27年度の新規治療患者数は19例平成26年度の11例と合わせてのtDCS治療患者数は30症例。16例に対してｆMRI lure taskにて海馬パターン分離能（lure 正答率）及びパターン補完能(same 正答率)を評価した。治療前のnew 正答率, lure 正答率, same 正答率はそれぞれ74.3±28.3%, 17.7±11.5%, 77.1±25.4%であった。重症度でみてみるとGrade Ⅰが2名、Grade Ⅱが9名、Grade Ⅲが5名であった。16症例にtDCS(左側DLPFCを陽極刺激し陰極を青を右側DLPFCに置いた）を施行した。その結果, new 正答率, lure 正答率, same 正答率は82.3±22.4%、43.1±18.1%、81.8±13.4%とすべて

の課題で改善し特にlure正答率は有意差をもって改善した（p<0.001）。重症度ではGrade0は9名，Grade Ⅰが3名，Grade Ⅱが4名，Grade Ⅲが0名となり、Grade Ⅱ，Ⅲの人数が減りGrade0の正常者が大きく増えた（p<0.05）。代表例（case 9）の海馬歯状回のactivation mapとBOLD patternを図に示す。治療前では歯状回の活性は陰性を示し、BOLDは下向きのピークを示していたが、治療後は正常群と同様のパターンに改善され、歯状回の活動性も改善された。

D．考察

海馬機能は機能的磁気共鳴画像（3TDiscovery,GE 社）による我々が独自に開発した Lure task（添付資料；海馬評価法参照）を用いて海馬 パーターン分離及びパターン補完を評価する事で神経新生能力を 4 段階で評価できる。最も重症なのは神経新生能が途絶した Grade III で経頭蓋的電気刺激法や薬物による賦活治療の適応となる。これにより神経新生の促進が期待できます。本症例では Case4 がこれに相当する。Grade II は神経新生能は途絶はしていないが機能低下が 1 ヶ月以上継続している患者群では海馬機能評価法で神経新生能は途絶していないが長期にわたる新生障害がありパターン補完能の機能異常を伴う。今回重症機能障害患者に対して海馬神経前駆細胞の神経新生を促進する作用が確認されている NMDA（N-メチル-D-アスパラギン酸）受容体拮抗薬メマンチンの併用効果が明らかになり治療終了後には grade III の海馬新生能の途絶者は皆無となり逆に grade 0 正常機能症例が 9 名となった。重篤な副作用は生じておらず平成 28 年度は引き続き症例を増やしその安全性や有効性を評価したいと考えている。

E．結論

海馬神経新生機能が低下した高次機能障害患者３名にtDCSにて左側DLPFCを陽極刺激で治療すると全例で海馬神経新生能を反映するパターン分離機能の改善とシナプス機能を反映するBOLDパターンの正常化が得られた。また機能改善にはtDCS1mA, 30分間左側DLPFC陽極電極刺激に加え海馬神経前駆細胞の神経新生を促進する作用が確認されているNMDA（N-メチル-D-アスパラギン酸）受容体拮抗薬メマンチンの併用が効果的であった。これにより有効なニューロリハビリテーションの治療法が確立できるものと思われる。

Ⅱ-2.労災疾病臨床研究事業費補助金
（分担）研究報告書

革新的高次脳機能治療法の樹立に関する研究
―高次脳機能解析―

研究分担者　外間洋平, 宇杉竜一

研究要旨：本年度紹介された高次脳機能障害患者は 28 例その内訳は頭部外傷 8 例(42,1%), 脳血管障害 7 例(36.8%),低酸素脳症 2 例(10.5%), 蘇生後脳症 2 例(10.5%)であった。神経心理学的検査の各 domain の成績低下比率は psychomotr speed 28%,excecutive function 22%, memory 17%,working memory 14%,attention 11%,globalcognitive function 8%でした。中等度以上の海馬機能障害が示唆されｔＤＣＳを施行した３例に全例で海馬パターン分離機能の改善が認められさらに内２例で記憶障害、注意障害等の高次脳機能障害の回復が得られた。

Ａ．研究目的

本研究の目的は労災による1) 交通事故, 転倒・転落事故等によるびまん性軸索損傷, 2) 過労により発症した心筋梗塞や脳卒中による低酸素脳症 3) 炭塵爆発事故による遷延化した一酸化中毒を対象に疾患により引き起こされた高次脳機能障害の神経心理学的評価を目的とする。

Ｂ．研究方法

脳疾患を有する9症例（平均46.9歳、女性7、男性2、脳腫瘍6例、くも膜嚢胞１例、線維筋痛症１例、交通外傷１例）、健常被験者42名（平均34.5y ±16.9　女性21名,男性21名）に対してDiffusion Tensor Image(DTI)を撮像し、高次機能と神経線維束の関連を検討した。症例は治療前後にかけて継次的に症状の把握とDTIデータを取得した。DTI解析方法は、GE 3T Discoveryを用いパラメータとしてsingle-shot spin-echo EPI sequence, TE=82.4,TR=9500ms, FOV=240mm, matrix size128*128, slice thickness=2mm,no spacing, NEX=1, MPG=29direction,b-value=1000s/mm2 にて撮像したデータをFiber tracking解析ソフト（Medinria1.9）を用いてtwo_ROI method（Wakana2007）に基づき、帯状回、海馬傍回、錐体路、前視床放線、上縦束、弓状束、下縦束、前頭後頭束、鉤状束、大鉗子、小鉗子、そして新たにFrontal Aslant Tract（以下FAT,Catani2012)の左右各12線維束の拡散テンソルtractgraphyを作成した。描出された各神経線維束のFA(Fractionated anisotropy)値、MD(Mean diffusivity)値を算出し集計した。

Ｃ．研究結果

《語列挙とFAT》右利き健常者9名の各神経線維束のFA値と語列挙能力との関連を調査した。左側のFATのみ語列挙との有意な相関関係（r=0.73,P=0.03）がみられた。また左半球の前頭側頭葉領域の腫瘍の症例においてFATの描出が乏しい症例は、語列挙数も比例して低下がみられ、左側FATと語の流暢性との関連が示唆された（図1）。FATが通過

する左前頭葉内側面損傷群では左背外側損傷群とは異なり、語列挙のみが障害されるという報告（大槻2003）と一致する結果となった。

《症例1》75歳女性、膠芽腫症例。左前頭葉腫瘍により、術前DTIでは左側FATの描出が困難で、重度の失語症によりコミュニケーションが極めて困難であった。術後３ヶ月時のフォローアップ時のDTIでは左FATの描出が可能となり、失語症状の改善がみられ、実用的なコミュニケーション能力を獲得することが出来た。特に自発話の流暢性と呼称能力の改善が著しく、FATは流暢性との関連を示唆した（図2）。

《症例2》51歳女性、線維筋痛症症例。tDSCによる治療を実施後にDTIによる解析を実施。tDCS治療後は疼痛緩和が得られ、症例の帯状回の神経線維束のStream number（神経線維束数）の増加がみられた（図3）。疼痛と帯状回との関連性については以前から報告が散見されるが、tDCSを用いた治療により疼痛緩和が得られた事は興味深く、疼痛緩和と帯状回の神経線維束との関連性を示唆する症例であった（図２）。

Ｄ．考察

脳疾患症例と健常被験者を対象に、左右各12線維束の拡散テンソルtractgraphyを作成し、高次脳機能との関連を検討した。疼痛緩和や言語機能の改善とともに、神経線維束の形態的変化を捉える事が可能であった。代表的な神経線維束に焦点を当てた解析を継続しながら、大脳皮質の全領域間を交錯する神経回路網についてグラフ理論を応用した解析を用いて検討していく予定である。

Ｅ．結論

多様な脳疾患により失語症、疼痛など様々な症状が出現する。今後，高次脳機能障害患者における多様な症状と白質の統合性との関連をグラフ理論の手法を用いて解析することでヒト脳機能の統合性に関する理解が深まるものと思われる。

図1　Frontal aslant tractと　語列挙との関連

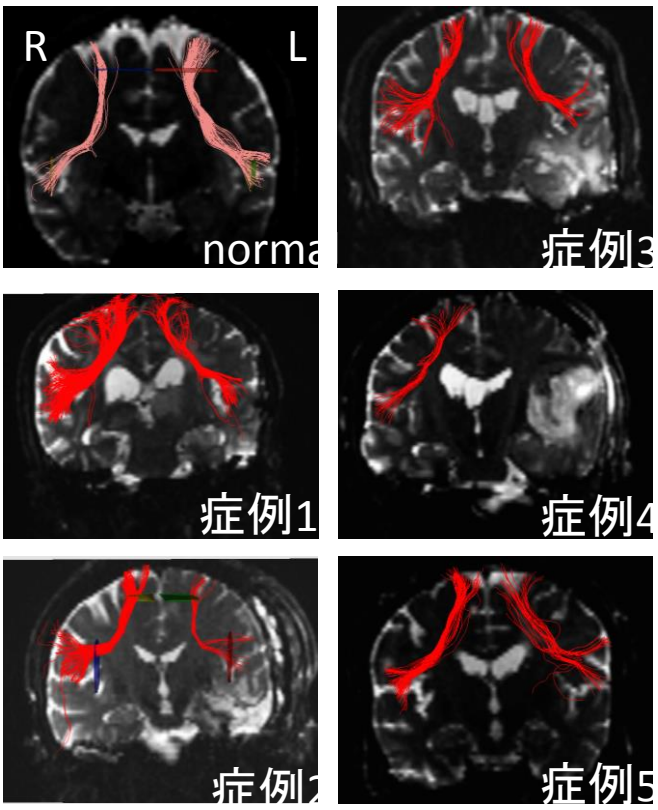

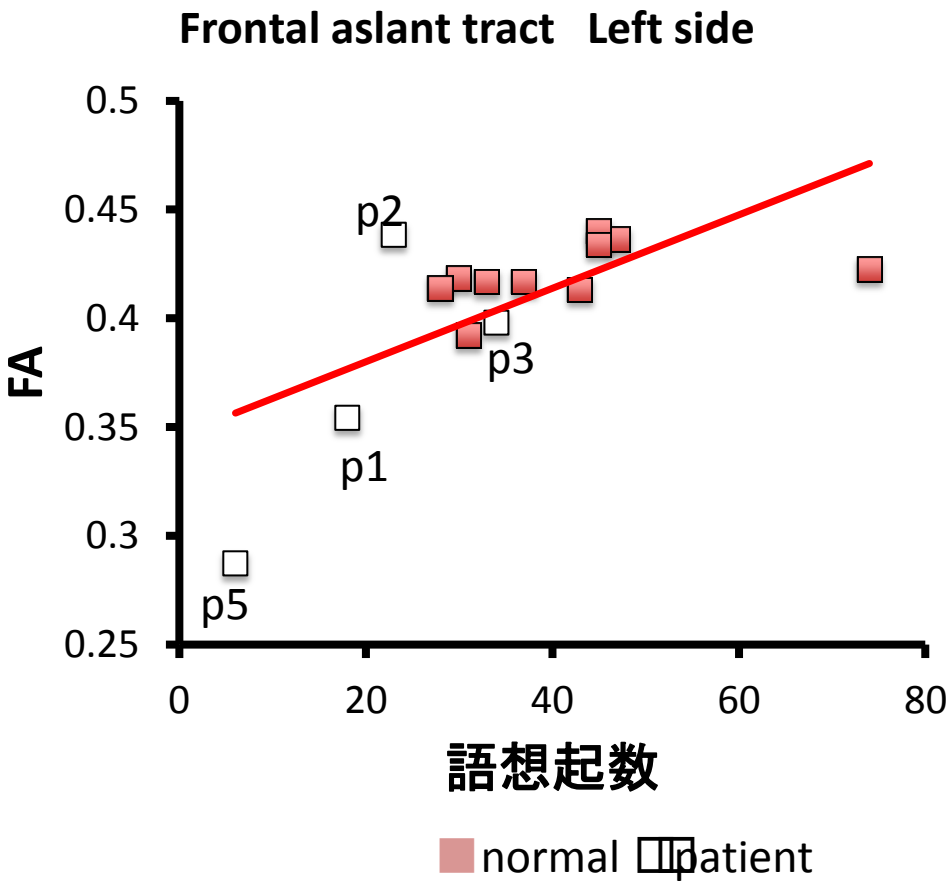

図2　症例1 75歳　女性　膠芽腫　Frontal Aslant Tract と言語機能

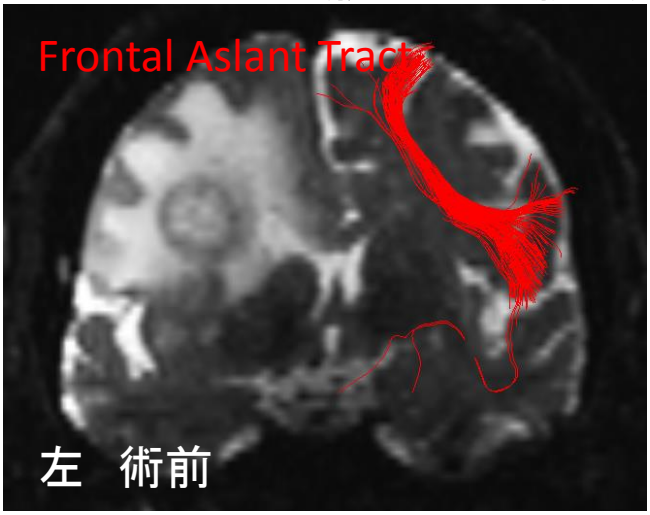

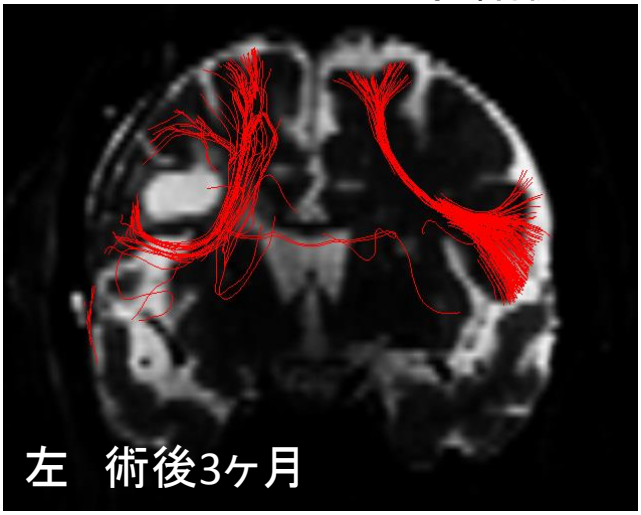

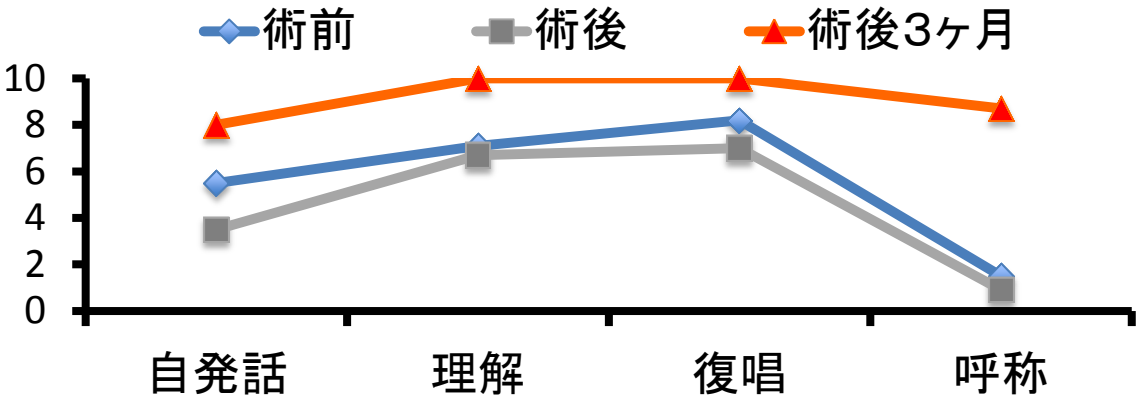

図3　症例2, 51歳　女性　線維筋痛症　tDCS後の帯状束

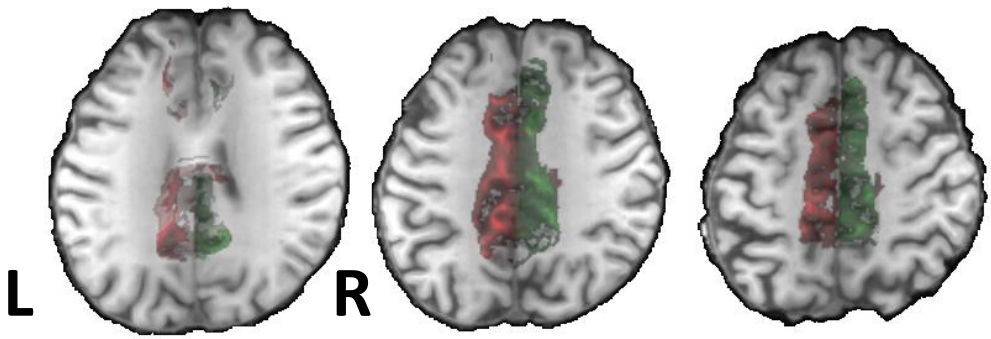

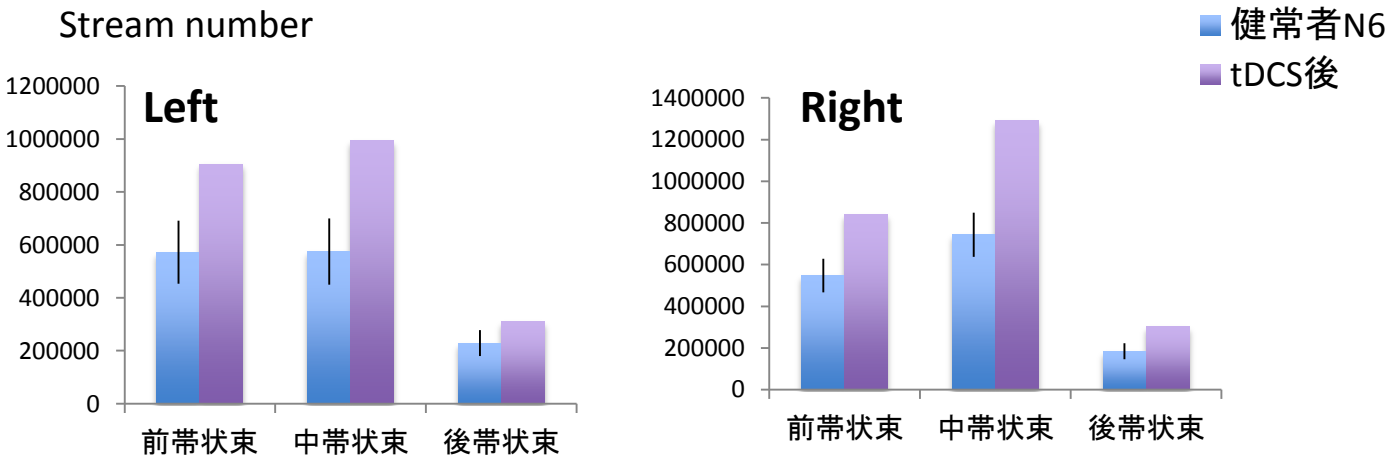

Ⅱ-3. 労災疾病臨床研究事業費補助金
（分担）研究報告書

革新的高次脳機能治療法の樹立に関する研究
―グラフ理論解析の応用による機能的ネットワーク解析―

研究分担者　西村正彦

研究要旨：革新的高次脳機能治療法の樹立を目的に高次脳機能障害患者30例に対しtDCS(transcranial Direct current stimulation)を用いて1mA, 30分間左側DLPFC(dorsolateral prefrontal cortex)を標的に直流電流刺激を施行した。lure taskを施行した16例にBOLD解析を行った。また安静時脳活動を利用した機能的ネットワーク解析について提示する。

Ａ．研究目的

本研究の目的は労災による1) 交通事故, 転倒・転落事故等によるびまん性軸索損傷, 2) 過労により発症した心筋梗塞や脳卒中による低酸素脳症 3) 炭塵爆発事故による遷延化した一酸化中毒を対象に疾患により引き起こされた高次脳機能障害に対する革新的な治療法の樹立をめざす。本研究では高次脳機能障害を小脳と海馬および前頭前野を含む神経回路網のネットワーク障害として捉える仮説を提示する（*Cerebellum submission* ）。高性能3T MRIを用いて海馬の活性化と安静時脳活動を用いて、左前頭前野の機能的ネットワークを評価する。

Ｂ．研究方法

本研究では交通外傷等により高次脳機能障害を呈した患者に対し tDCS を用いた治療を行いました。1mA, 30 分間左側 DLPFC(dorsolateral prefrontal cortex)を標的に陽極電極を置き、反対側右側側 DLPFC に陰極電極を留置して直流電流刺激を施行した。海馬機能については Lure task を用いて海馬の% BOLD シグナルの変化（BOLD 機能をパターン解析および%BOLD 変化の算定、P1(initial positive peak), P2(second positive peak), N1(initial negative peak), N2(second negative peak)の amplitude, latency とグラフ理論解析を用いた機能的ネットワーク解析を行った。グラフ理論解析の方法論は、Rubinov & Sporns (2010)を改変し、行った。まず、安静時 fMRI データの体動補正、標準化、平滑化処理を行う。次に全脳 116 の関心領域(Tzourio 2002、図3)間の相関係数 (r) を算出した。相関係数 (r)を Fisher Z 変換にて標準化（z 値)し、各関心領域間の機能結合係数を算出した。算出された各関心領域間の機能結合係数から Clustering coefficient を算出し、関心領域ごとの Clustering

coefficient と機結合係数をマップ上に表示した。
Clustering coefficient は他の脳領域との集合体としての機能結合を表し、この数値が高ければ、同じ機能を持つ脳領域の機能結合が強いことを示す。また、機能的結合係数は関心領域と他の領域間との結合性の強さを示す。

C．研究結果

別紙資料の如くに30例（平成26年度11例、平成27年度は19例）に対し、ｔDCS治療を行い、安静時脳活動計測を行った。そのうち、ｆMRI lure task を施行した16例のうち、メマンチン酸塩の服用を併用した患者と服用していない患者に分けてBOLD機能をパターン解析および%BOLD変化の算定、P1(initial positive peak), P2(isecond positive peak), N1(initial negative peak), N2(second negative peak)のamplitude, latencyを算定した。健常者群36例、ｔDCSとメマンチン酸塩服用無し群、ｔDCSにメマンチン酸塩服用有り群のBOLDパターンとamplitude, latencyを図1に提示する。健常者群（n=36、男性36名、女性13名、平均年齢25.2±2.9歳）のBOLD反応では1.7±1.5秒でN1（amplitude -0.04±0.17）が観察され、次いで4.1±1.1秒に上向きのピークであるP1（amplitude 0.07±0.29）が出現する。その後、陰性のピークN2（amplitude -0.19±0.27）が8.4±1.6秒に見られる。メマンチン酸塩を服用しなかった群（男性5名、女性5名、平均年齢43.2±19.1歳）のBOLD反応ではN1のピークは見られず、緩やかな上向きのカーブを描くP1（amplitude 0.5±0.57）が4.24±2.08秒に観察され、同じく緩やかなN2（amplitude -0.06±0.44）のカーブが14.9±4.43秒に観察された。メマンチン酸塩を服用しなかった群のBOLD反応のばらつきは大きく、二峰性の峰と谷を形成している。メマンチン酸塩服用を併用した群（男性2名、女性4名、平均年齢47.8±18.1歳）のBOLD反応では、2.28±2.1秒にN1（amplitude -0.18±0.51）が観察され、次いで陽性のピークP1（amplitude 0.58±0.83）が4.76±1.24秒に現れ、最後にN2のピーク（amplitude -0.34±0.44）が9.73±5.54秒に観察された。メマンチン酸塩内服を併用した群のBOLDパターンはメマンチン酸塩を服用しなかった群に比べ、健常者に近いパターンを示したが、N1、N2のピーク潜時はやや健常者群に比べ遅延していた。また、メマンチン酸塩を服用した群、メマンチン酸塩を服用しなかった群どちらのP1のamplitudeは健常者群のピークamplitudeに比べは高い値を示した。メマンチン酸塩を服用した群のN1,N2ピークのamplitudeは健常者群に比べ低い値を示した。

図２に、交通外傷後のび慢性軸索損傷により高次脳機能障害を呈した21歳男性のtDCS治療前後のlure taskの正答率とグラフ理論解析による機能的ネットワーク解析の結果を示す。この症例の治療前のlure taskのnew, lure, sameの正答率は、それぞれ82%、13%、94%であった、tDCS治療後はnew正答率　87%, lure正答率　56%, same正答率　81%と、lure正答率は改善した。

機能的ネットワーク解析の結果、治療前のclustering coefficientは右中心傍小葉（0.83）、左補足運動野（0.83）、両側の後頭葉（1.0）が他の関心領域に比べ高い値を示し、後頭頭頂部領域を中心としたネットワーク形成が

見られる。tDCS治療後は、左中前頭回(0.83)、左上前頭回内側部（0.87）、右下前頭回弁蓋部（0.89）のclustering coefficientが高まり、両側の後頭葉のclustering coefficient（0.33）は治療前に比べ低下した。左中前頭回のClustering coefficientは治療前0.4からtDCS治療後に0.83に増加した。また、左中前頭回と他の脳領域との機能結合係数は治療前0.75であったが、tDCS治療後は0.84に増加している。tDCS治療後は左前頭葉を中心とした機能的ネットワークが形成されその機能的結合性が増強したと考えられる。

Ｄ．考察

海馬機能は機能的磁気共鳴画像（3TDiscovery,GE 社）による我々が独自に開発した Lure task を用いてメマンチン酸塩の服用の有無による BOLD パターンの解析と安静時脳活動を利用した機能的ネットワーク解析を行った。

BOLD パターンの解析では、メマンチン酸塩の内服を併用して、tDCS 治療を実施することで、海馬の血流の変化がより健常者のパターンに近づくことが分かった。これはメマンチン酸塩によって海馬神経前駆細胞の神経新生が促進され、海馬歯状回の活動性が健常者に近似したと思われる。したがって、海馬の血流変化からも、tDCS 治療に NMDA（N-メチル-D-アスパラギン酸）受容体拮抗薬メマンチン酸塩を併用することは認知機能の改善に有効であると思われる。

機能的ネットワーク解析では、tDCS 治療の前後で認知機能の中枢として作用する左中前頭回の機能的ネットワークの様相が変化することが分かった。治療前、後頭葉優位のネットワークが形成されていたが、治療後は左中前頭回を中心としたネットワークに変化した。lure 刺激に対する反応を見ても、治療前は same と反応する割合が多かったが、治療後は半数以上の刺激に対し正しく lure と反応している。ワーキングメモリなどの認知機能の中枢として駆動する左中前頭回への経頭蓋的電気刺激は脳内の機能的ネットワークを改変させ、海馬パターン分離能の改善に寄与していると考えられえる。

今後は、BOLDパターン分析に、グラフ解析による機能的ネットワークの評価を加え、経頭蓋的電気刺激法、メマンチン酸塩による高次脳機能障害患者の認知機能障害の改善について分析を進め、これらの治療法の適応や予後予測について解析を計画する。

Ｅ．結論

海馬歯状回のBOLDパターン分析によって、メマンチン酸塩の服用による高次脳機能障害患者のBOLD反応が正常化することが示された。また、機能的ネットワーク解析の結果、左中前頭回への経頭蓋的電気刺激は脳内のネットワークの調整に関与している可能性がある。

図1　メマンチン酸塩の服用による海馬歯状回BOLD反応

A.　健常者群　（n = 36）

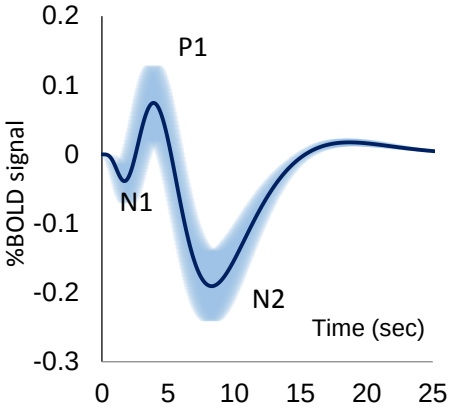

B.　tDCS治療後
メマンチン服用なし (n = 10)

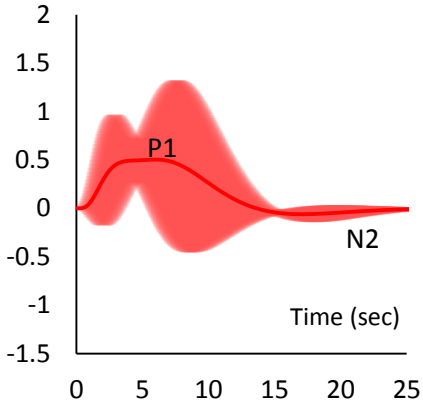

C.　tDCS治療後
メマンチン服用あり (n = 6)

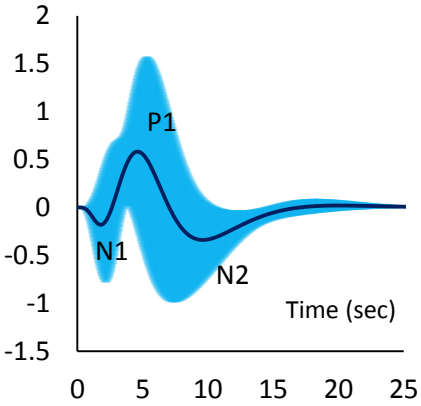

D.　健常者群　（n = 36）

	Latency (sec) Mean ± SD	%BOLD change Mean ± SD
N1	1.7±1.5	−0.04±0.17
P1	4.1±1.1	0.07±0.29
N2	8.4±1.6	−0.19±0.27

E.　メマンチン服用なし (n = 10)

	Latency (sec) Mean ± SD	%BOLD change Mean ± SD
N1	None	None
P1	4.24±2.08	0.50±0.57
N2	14.9±4.43	−0.06±0.44

F.　メマンチン服用あり (n = 6)

	Latency (sec) Mean ± SD	%BOLD change Mean ± SD
N1	2.38±2.1	−0.18±0.51
P1	4.76±1.24	0.58±0.83
N2	9.73±5.54	−0.34±0.44

A.健常被験者36名（男性36名、女性13名、平均年齢25.2±2.9歳）のlure taskにおける海馬歯状回の平均BOLD反応グラフ。B.メマンチン酸塩服用せずtDCS治療を受けた高次脳機能障害患者10名（男性5名、女性5名、平均年齢43.2±19.1歳）の平均BOLD反応。C.メマンチン酸塩を服用し、tDCS治療を受けた高次脳機能障害患者6名（男性2名、女性4名、平均年齢47.8±18.1歳）の平均BOLD反応。
グラフのx軸は時間（秒）を表し、y軸はBOLD信号の変化率を表す。
A.B.C.のグラフの青もしくは赤の実線は%BOLD signalの平均を表し、青または赤の透明色の範囲は%BOLD signalの標準偏差を表す。
D, E, Fの表は健常者群、メマンチン酸塩併用無し群、メマンチン酸塩併用群それぞれの海馬歯状回におけるBOLD反応の、N1,N2,P1のlatencyとamplitudeについて記した。

図2　グラフ理論解析によるネットワーク解析

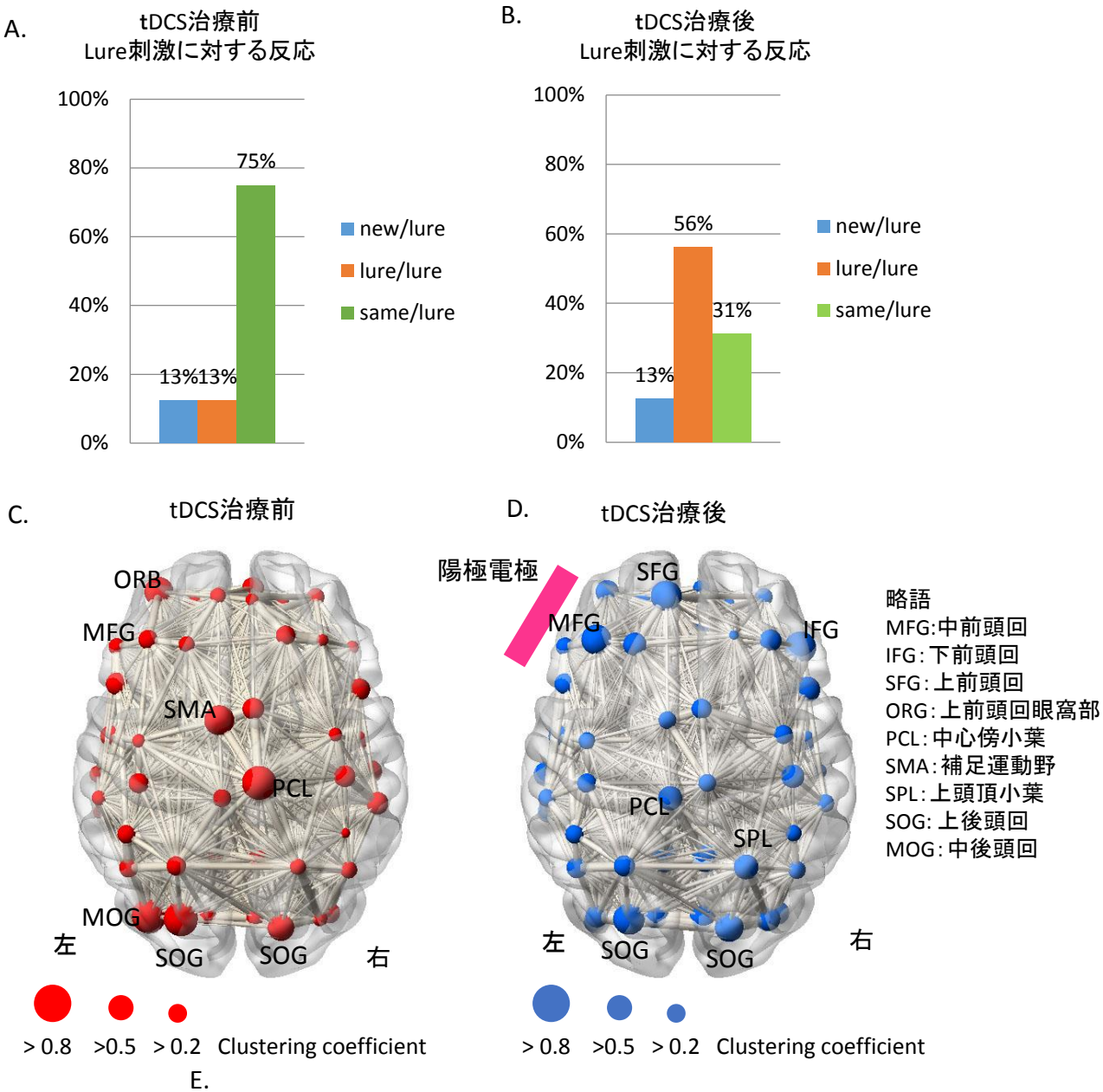

E.

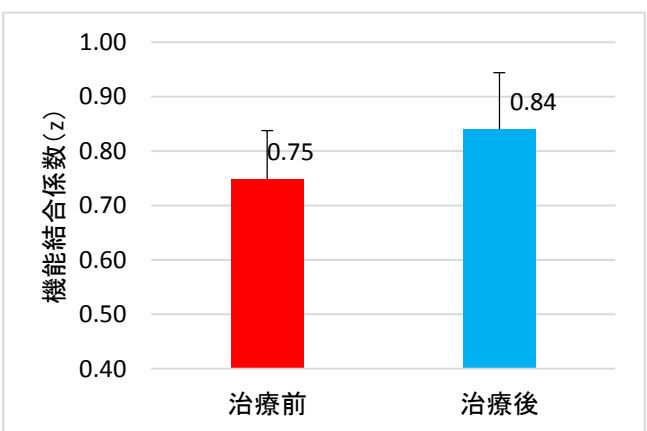

A.B.tDCS治療前とtDCS治療後の症例（21歳　男性　交通外傷後び慢性軸索損傷）のLure刺激に対する反応の割合を示したグラフ、青はnew、橙はlure、緑はsameと反応した割合を示す。刺激はlureであるので、橙色がlureの正答率を表す。C,DはtDCS治療前、治療後の機能的ネットワーク解析のそれぞれの結果を示す。丸は関心領域のclustering coefficient の値を表し、丸が大きいほど、値が大きい。灰色のラインは関心領域間の機能結合係数を表す。関心領域の略語の解説はパネルDの右に示す。E.左中前頭回と他脳領域との機能結合係数の平均値を示す。赤または青の棒グラフはそれぞれ治療前の値、治療後の値を表す。棒グラフ上の縦線は標準誤差を示す。

労災疾病臨床研究事業費補助金
（分担）研究報告書

革新的高次脳機能治療法の樹立に関する研究
―高密度（256ch）脳波計およびfMRIを用いた解析―

研究分担者　　土田幸男

研究要旨：革新的高次脳機能治療法の樹立を目的に，高次脳機能障害の治療的有効性を評価するための指標として高密度脳波計および fMRI を用いて海馬機能を反映するパターン分離遂行中の脳活動を解析した。
健常成人 11 名，高次脳機能障害患者 2 例から海馬パターン分離機能を反映する事象関連電位が得られた。今後，症例を増やし得られた事象関連電位所見の生物学的意味づけおよび高次脳機能障害のバイオマーカーとなりうるか更なるデータの蓄積を行う。また高次脳機能障害診断装置の汎用化を目的に海馬パターン分離機能を反映する事象関連電位簡易測定法の開発を行っていく予定である。

Ａ．研究目的

本研究の目的は労災による1) 交通事故，転倒・転落事故等によるびまん性軸索損傷，2) 過労により発症した心筋梗塞や脳卒中による低酸素脳症，3) 炭塵爆発事故による遷延化した一酸化中毒を対象に疾患により引き起こされた高次脳機能障害について，高密度（256ch）脳波計およびfMRIを用いた高次脳機能障害の治療的有効性を評価する脳活動の特定を目的とする。

Ｂ．研究方法

健常成人11名（女性4名，男性7名，平均年齢20±3歳）を対象とした。患者データは20症例数の中から治療前後の比較が可能で効果が検討できる2例を対象とした。

海馬機能を測定するために独自に開発したLure task遂行中の脳活動を，高密度センサー脳波とfMRIを用いて同時計測を行った。高密度センサー脳波計測は，EGI HydoroCel Geodesic Sensor Net 256-cannelを用いた。fMRIは，GE 3T Discoveryを用いた。脳波計測のサンプリング周波数は1000 Hz，Referenceは全電極平均とした。電極インピーダンスはシステム推奨の50 kΩ以下とした。計測後，EGI Net Station Toolsを用い，0.10HzのHighpassフィルタを適用，そしてMRI計測に伴うグラディエントノイズと心拍動のノイズを除去した。分析時はSSI EMSEを用いて，0.5–50 HzのBandpass，ICAによる眼球運動ノイズ除去を適用した。刺激呈示前100 msから刺激呈示後2000 msの区間を分析区間とし，刺激ごとに加算平均を行い，事象関連電位（ERP）を算出した。

（倫理面への配慮）

研究対象者に対しては検査時間の短縮

に努め又随時不安の軽減目的に声かけをしている。高密度脳波型電極の取り付けは、従来のペースト法ではなく最新型アレーを用いており軽く水にぬらすのみで装着可能で所要時間の大幅な短縮が得られ可能で入室から３０分弱で完了する。またMRI撮像に関しては検査時間の短縮に努めると同時と同時にマイクロホンによる検査施行中の意思疎通に努めている。撮像時間は海馬課題タスクが7分、その後安静時脳活動検査を行う事で5分間の休憩ができる。安静時脳活動はこの休憩時に撮像している。この間，緊急時のブザーを用意して常に緊急コールが出来る状態で検査を進めている。予め承諾を得た上でのテレビカメラによるモニターを行い患者が安全に検査を受けられる環境の形成に努める配慮を行っている。現在までのところ有害事象の発生はない。

Ｃ．研究結果

資料1に示したLure task(似ているが細かい部分が異なる対象物の識別能力検査)にて，海馬パターン分離のERPを解析した。資料2に健常者データの平均を示す。Lureに対し，前頭部電極のERPでは刺激呈示後約900 ms付近に陰性成分を惹起した。これは再認記憶研究で報告されている曖昧な記憶痕跡を評価する過程と類似している（Rugg & Curran, 2007）。側頭葉底部の活動を捉えることができると報告されている顔面部位電極(海馬体の電気活動を取得できる)のうち右側でのERPにおいて，Lureは同様の時間帯で陰性成分を惹起した。時間周波数分析では，記憶活動に関連するθ帯域（4～8 Hz）の活動が前頭部では弱く，右顔面部位では強く見られた。顔面部位電極の脳活動はLureに対する特異的な反応である可能性を示唆している。

より詳細な分析を行うため，fMRIデータを含めた個別データの検討を行った。健常者1と2は正常範囲のLure正答率を示した（資料3一段目）。顔面部位電極でのERPにおいて，Lureは刺激呈示後約1000 msに大きな陰性成分を惹起した（資料3二段目）。時間周波数分析では，同時間帯でθ帯域の活動が見られた（資料3三段目）。ERP後の時間帯の分析となるfMRIでは，右海馬の賦活を認め，initial dipが存在する正常なBOLD活動が示された。

症例1（術前）は両側前頭葉の神経膠腫患者である。低いLure正答率を示し，ERPの陰性成分は惹起したものの活動が遅いことを示した。時間周波数分析では，顕著なθ帯域活動を認めなかった。fMRIでは，右海馬の低活動を認め，initial dipが存在しない異常なBOLD活動が示された。症例1（術後）では，正常範囲のLure成績を示し，ERPにおいても， 1000 msに大きな陰性成分を惹起した。時間周波数分析ではθ帯域活動を認めた。fMRIのデータも術前より健常者に近いデータとなっている。

症例2（tDCS治療前正答時）はうつ病による認知機能低下を主訴としてtDCS治療を行った患者である（資料4）。極めて低いLure正答率であった。正答時のERP陰性成分は惹起し，θ帯域の活動も見られている。一方，大多数を占める誤答時は，θ帯域の活動は見られるものの，

ERPは全般的に陽性の極性を示した。症例2（tDCS治療後）では，Lure正答率が上昇し，ERPは顕著なピークを認めないものの，全般的に陰性の極性を示した。θ帯域の活動も認められた。これらの所見は，tDCS治療の効果を反映している可能性を示唆している。

D．考察

脳波分析の結果から，fMRIでは検討できなかった脳の直接的な神経活動を検討することができる可能性が示唆された。これらの所見を用いることで，高次脳機能障害の治療的有効性を評価できることが見込まれる。今後，健常群と治療前後の患者データを蓄積するとともに，より簡便な脳波測定による評価の確立が望まれる。臨床評価や行動指標だけでは判断しにくい海馬機能の問題を評価できる可能性があるだろう。

E．結論

健常成人 11 名，患者 2 名を対象とした事象関連電位を解析し，顔面部位電極の陰性電位が海馬機能の評価に有用である可能性が示唆された。高次脳機能障害のバイオマーカーとなりうるか更なるデータの蓄積を行う。

資料 1　海馬課題ーCerebellum 2015 より引用ー

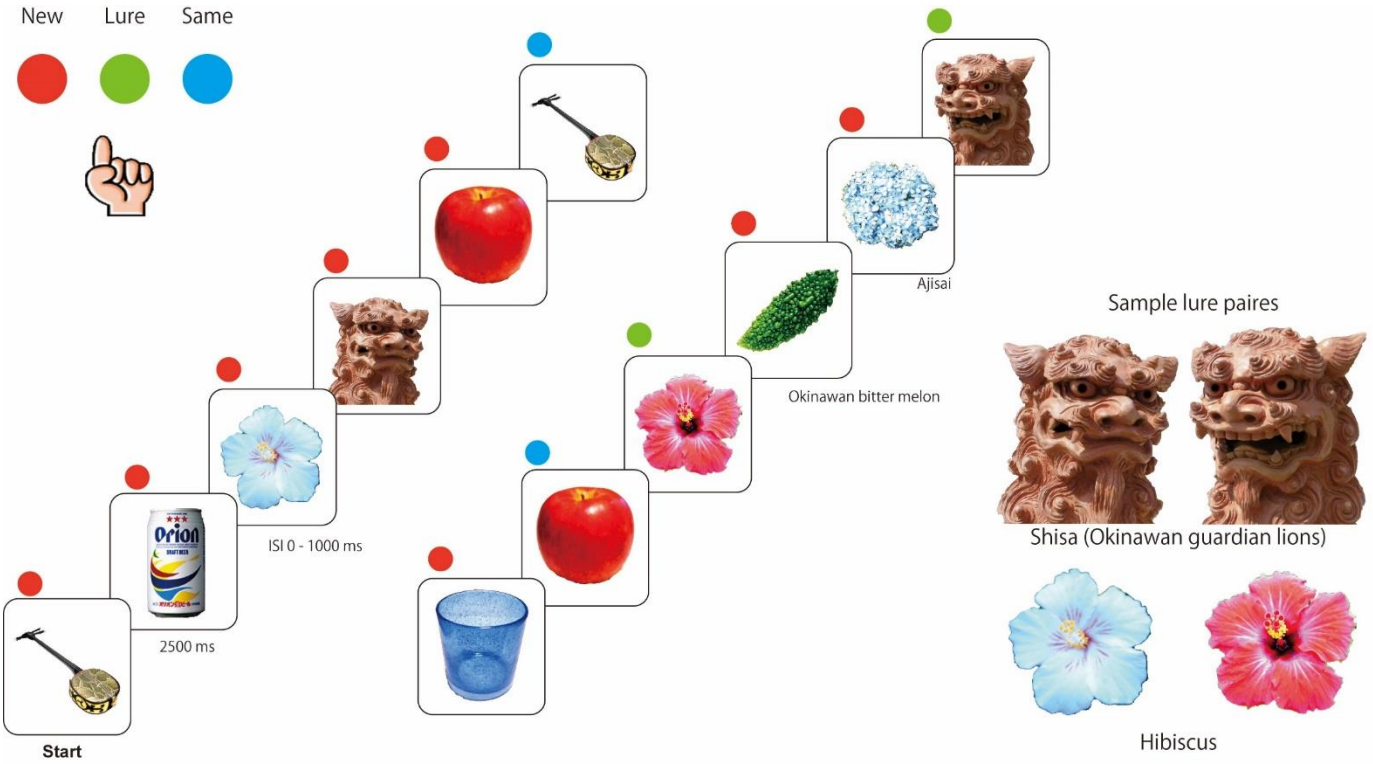

資料 2　健常成人 11 名の平均

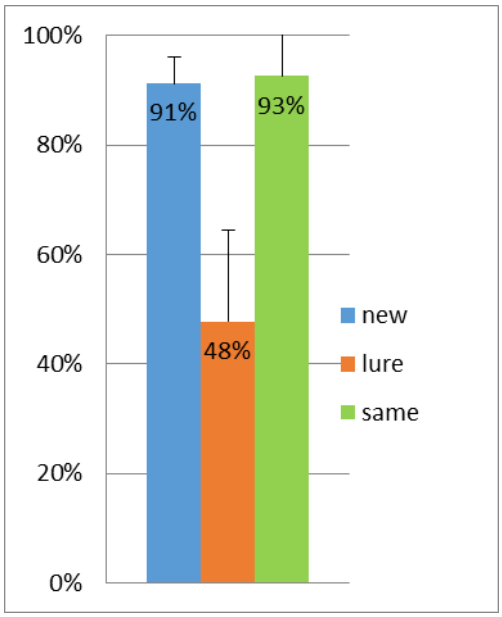

Lure task 平均正答率

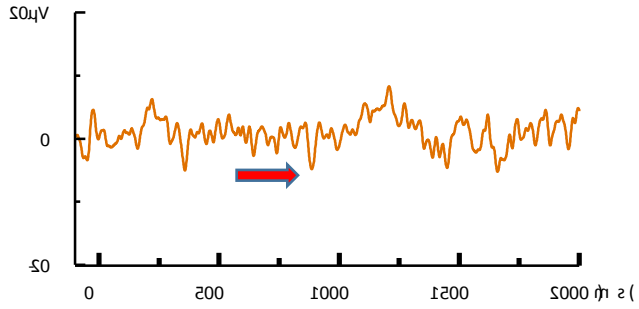

前頭部位電極における Lure task のパターン分離に対する ERP

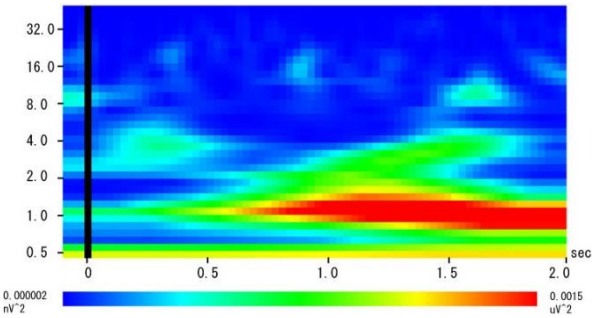

前頭部位電極における Lure task のパターン分離に対する時間周波数分析

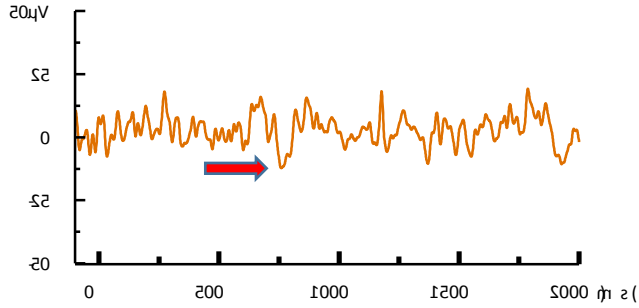

右顔面部位電極における Lure task のパターン分離に対する ERP

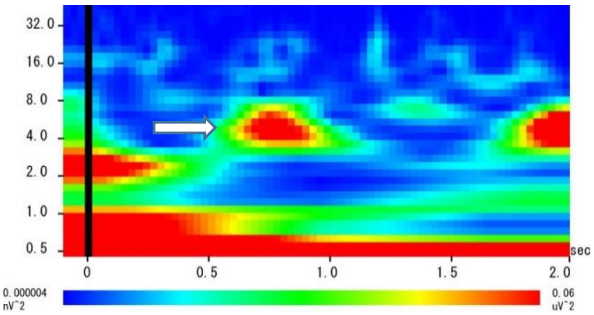

右顔面部位電極における Lure task のパターン分離に対する時間周波数分析

Lure に対し，前頭部電極で約 900 ms 付近に（赤矢印），右顔面部位電極においても同様の時間帯で陰性成分が惹起（赤矢印）（左列）。時間周波数分析では，θ 帯域（4〜8 Hz）の活動が前頭部では弱く，右顔面部位では強く見られた（白矢印）（右列）。

資料 3

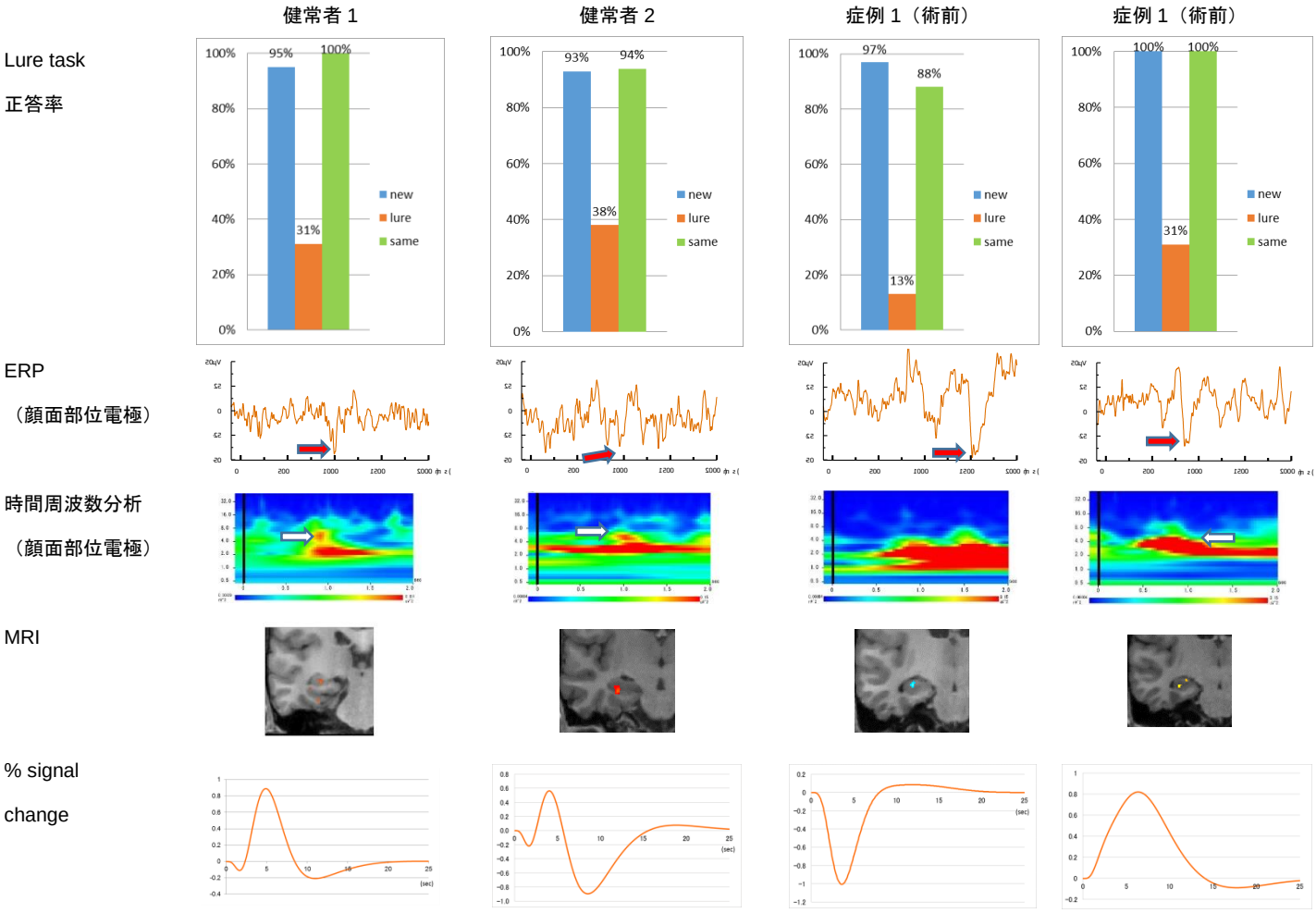

健常者 1 と 2 は正常範囲の Lure 正答率（資料 3 一段目）。顔面部位電極で約 1000 ms に大きな陰性成分が惹起（赤矢印）（資料 3 二段目）。時間周波数分析では，約 1000 ms で θ 帯域の活動が見られた（白矢印）（資料 3 三段目）。fMRI では，右海馬の賦活，initial dip を認めた（資料 3 四段目）。

症例 1（術前）は，低い Lure 正答率，ERP の陰性成分頂点は約 1500ms と遅延，θ 帯域活動を認めず，fMRI では右海馬の低活動，initial dip が存在しなかった（三列目）。症例 1（術後）では，Lure 成績は正常，1000 ms に大きな陰性成分が惹起，θ 帯域活動を認め，fMRI のデータも術前より健常者に近いデータとなった（四列目）。

資料 4

	症例 2（tDCS 前正答時）	症例 2（tDCS 前誤答時）	症例 2（tDCS 後）
Lure task 正答・誤答率	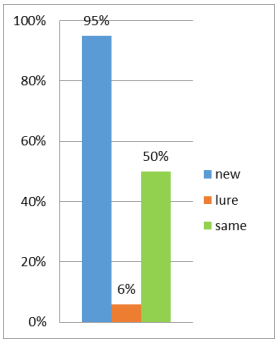	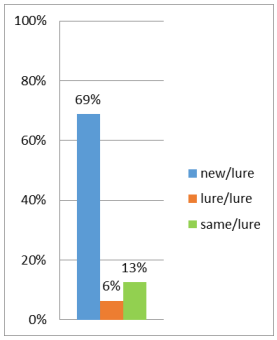	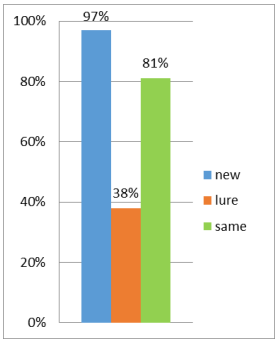
	Lure に対する 正答率	Lure に対する 反応タイプ別誤答率	Lure に対する 正答率
ERP （顔面部位電極）	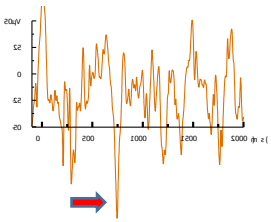	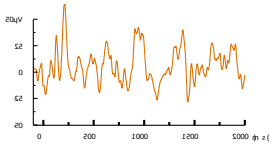	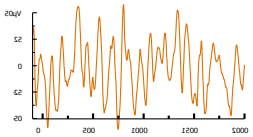
時間周波数分析 （顔面部位電極）	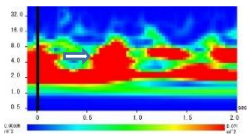	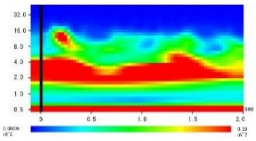	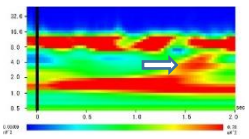

症例 2（tDCS 治療前正答時）は極めて低い Lure 正答率（6%），正答時は 750 ms に ERP 陰性成分および θ 帯域の活動を認めている（一列目）。大多数を占める誤答時は，θ 帯域の活動は見られるが，ERP は全般的に陽性の極性を示した（二列目）。症例 2（tDCS 治療後）では，Lure 正答率が上昇，ERP は顕著なピークを認めないものの，全般的に陰性の極性（赤矢印），θ 帯域の活動を認めた（白矢印）（三列目）。

Ⅲ. 研究成果の刊行に関する一覧表

書籍

著者氏名	論文タイトル名	書籍全体の編集者名	書　籍　名	出版社名	出　版地	出版年	ページ
石内勝吾	経頭蓋直流電気刺激法と脳腫瘍手術	石内勝吾	ブレインナーシング	ＭＣメディカ出版	日本	2015	83-85

雑誌

発表者名	論文タイトル名	発表雑誌	巻号	ページ	出版年
Shiroma A, Nishimura M, Nagamine H, Miyagi T, Hokama Y Watanabe T, Murayama S, Tsutsui M, Tominaga D, Ishiuchi S.	Cerebellar Contribution to Pattern Separation of Human Hippocampal Memory Circuits.	Cerebellum	-	1-18	2015
Nagaishi M, Nobusawa S, Matsumura N, Kono F, Ishiuchi S, Abe T, Michimasa Ebato, Yin Wangg, Hyodo A, Yokoo H, Nakazato Y.	SLC44A1-PRKCA fusion in papillary and rosette-forming glioneuronal tumors.	Journal of clinical neuroscience	23	73-75	2015
Kozuka C, Sunagawa S, Ueda R, Higa M, Ohshiro Y, Tanaka H, Shimizu-Okabe C, Takayama C, Matsushita M, Tsutsui M, Ishiuchi S, Nakata M, Yada T, Miyazaki J, Oyadomari S, Shimabukuro M, Masuzaki H.	A novel insulinotropic mechanism of whole grain-derived γ-oryzanol via the suppression of local dopamine D2 receptor signaling in mouse islet.	British journal of pharmacology	172	4519 -4534	2015
Noguchi K, Matsuzaki T, Sakanashi M, Hamadate N, Uchida T, Kina-Tanada M,et al. Noguchi K, Matsuzaki T, Sakanashi M, Hamadate N, Uchida T, Kina-Tanada M, Kubota H, Nakasone J, Sakanashi M, Ueda S, Masuzaki H, Ishiuchi S, Ohya Y, Tsutsui M.	Effect of caffeine contained in a cup of coffee on microvascular function in healthy subjects.	Journal of pharmacological sciences	127	217-222	2015

Kozuka C, Sunagawa S, Ueda R, Higa M, Tanaka H, Shimizu-Okabe C, Ishiuchi S, Takayama C, Matsushita M, Tsutsui M, Miyazaki J, Oyadomari S, Shimabukuro M, Masuzaki H.	Gamma-oryzanol protects pancreatic β-cells against endoplasmic reticulum stress in male mice.	Endocrinology	156 (4)	1242 -1250	2015
Ishiuchi S	Ca2+-permeable AMPA -type glutamate receptors and glioblastomas	Progress in Neuro-Oncology	22 -2	1-8	2015

Ⅳ.研究成果の刊行物・別刷

Cerebellum
DOI 10.1007/s12311-015-0726-0

ORIGINAL PAPER

Cerebellar Contribution to Pattern Separation of Human Hippocampal Memory Circuits

Ayano Shiroma[1] · Masahiko Nishimura[1] · Hideki Nagamine[1] · Tomohisa Miyagi[1] · Yohei Hokama[1] · Takashi Watanabe[1] · Sadayuki Murayama[2] · Masato Tsutsui[3] · Daisuke Tominaga[4] · Shogo Ishiuchi[1]

Abstract The cerebellum is a crucial structure for cognitive function as well as motor control. Benign brain tumors such as schwannomas, meningiomas, and epidermoids tend to occur in the cerebellopontine angle cisterns and may cause compression of the posterior lateral cerebellum near the superior posterior fissure, where the eloquent area for cognitive function was recently identified. The present study examined cognitive impairment in patients with benign cerebellar tumors before and after surgical intervention in order to clarify the functional implications of this region in humans. Patients with cerebellar tumors showed deficits in psychomotor speed and working memory compared with healthy controls. Moreover, these impairments were more pronounced in patients with right cerebellar tumors. Functional magnetic resonance imaging during performance of a lure task also demonstrated that cerebellar tumors affected pattern separation or the ability to distinguish similar experiences of episodic memory or events with discrete, non-overlapping representations, which is one of the important cognitive functions related to the hippocampus. The present findings indicate that compression of the human posterior lateral cerebellum affects hippocampal memory function.

Keywords Posterior lateral cerebellum · Cognitive function · Brain tumor · Memory · Hippocampus · fMRI

Introduction

Recent research has shown that the cerebellum plays an important role in cognitive and emotional functions as well as motor control [1–4]. Studies using functional magnetic resonance imaging (fMRI) have shown that the actual use of a tool (e.g., scissors) primarily activates the anterior cerebellum, whereas imaginary use of a tool activates the lateral posterior lobe of the cerebellum [5]. Skilled use of the tool after learning activates a specific area near the superior posterior fissure, indicating that the posterior cerebellum is essential for information processing, space representation, and some procedural memory [6, 7] and is dependent upon the sequential relationship between discrete elements, just as in the serial reaction task. However, the acquisition of other skills does not require the learning of sequences like prism adaptation, which can be acquired during short-term motor learning. Human studies have identified the important contribution of the cerebellum to intrinsic functional connectivities [8, 9] and higher cognitive functions, especially to episodic memory, working memory, and procedural memory [10–13]. Nonetheless, the relationship between the cerebellum and hippocampal circuits in memory systems has not been fully evaluated.

Benign cerebellar tumors are isolated focal lesions that are frequently localized in the cerebellopontine angle or around

Ayano Shiroma, Masahiko Nishimura and Shogo Ishiuchi contributed equally to this work.

✉ Shogo Ishiuchi
ishogo@med.u-ryukyu.ac.jp

[1] Department of Neurosurgery, Graduate School of Medicine, University of the Ryukyus, 207 Uehara, Nishihara-machi, Nakagami-gun, Okinawa 903-0215, Japan

[2] Department of Radiology, Graduate School of Medicine, University of the Ryukyus, 207 Uehara, Nishihara-machi, Nakagami-gun, Okinawa 903-0215, Japan

[3] Department of Pharmacology, Graduate School of Medicine, University of the Ryukyus, 207 Uehara, Nishihara-machi, Nakagami-gun, Okinawa 903-0215, Japan

[4] Okinawa Study Center, The Open University of Japan, 1Senbru, Nishihara, Okinawa 903-0219, Japan

Published online: 06 October 2015

the superior posterior fissure and do not invade or destroy neural networks, unlike gliomas or vascular strokes. These tumors are essentially regional, thereby allowing a more discrete estimation of the functionality of a specific region through examination of whether the function lost before operation recovers after surgical treatment. However, although preservation of VIIth and VIIIth cranial nerve function is prioritized during neurosurgical treatment, the cognitive function of these patients has not been evaluated. We therefore analyzed the cognitive impairment of patients before and after surgical intervention in order to evaluate the functional involvement of the posterior lateral cerebellum near the superior posterior fissure. We found that patients with right cerebellar tumors exhibited disturbances in psychomotor speed as examined by the digit symbol test (DST) and working memory as examined by the digit span test (DS) when compared with healthy controls. Nonetheless, the classical neuropsychological domain does not really have a distinct functional anatomy.

In the current study, we analyzed the distinct human cerebellar contribution to memory systems under whole brain network organization using the method of Global Brain Connectivity (GBC). Several past studies have indicated that cognition involves large-scale human brain systems with multiple interacting regions. We therefore tried to identify a prominent feature of this hub of human cognition using lure task-related and resting-state functional MRI (rs-fMRI) data. We focused on the pattern separation ability that discriminates between similar experiences of episodic memory, a crucial component of the hippocampal memory circuit, and used functional MRI (fMRI) to investigate subjects performing an established lure task [14]. Interestingly, patients with cerebellar tumors selectively showed a decreased ability for pattern separation in the lure task. We first identified nine regions related to pattern separation ability by imposing stringency criteria based on an activation map of lure task fMRI findings from normal volunteers. Blood oxygen level-dependent (BOLD) signals, which are one of the indices of hemodynamic responses to neural activity, were correlated to correct response rates in the lure task associated with the activity of the following four distinct regions: right and left cerebellar hemisphere (lobule VI/Crus I), left anterior mid-cingulate cortex (aMMC), and right hippocampal dentate gyrus (DG). We then tested whether these regions showed high GBC in the rest of the brain using rs-fMRI data. We found that GBC correlated to a correct response rate in the lure task was limited to three of these regions, excluding the left cerebellar lobule VI/Crus I. Finally, we ascertained that this correlation was altered in patients with right and left cerebellar tumors as compared with normal healthy volunteers. We therefore hypothesized that the cerebellar contribution to pattern separation ability is dependent upon integration of the right cerebellar hemisphere (lobule VI/Crus I) associated with the left aMMC and right hippocampal DG. The pattern changes in the functional connectivity of patients with cerebellar tumors may indicate an important contribution of the human cerebellum to higher cognitive functions associated with hippocampal memory systems.

Materials and Methods

Subjects

Neuropsychological assessments were carried out on 28 patients with benign cerebellar tumors (mean age 50.9± 12.1 years; 11 males, 17 females), 17 with right cerebellar lesions (mean age 49.4±13.6 years; 8 schwannomas, 8 meningiomas, and 1 epidermoid) and 11 with left cerebellar lesions (mean age 53.5±8.3 years; 6 schwannomas, 2 meningiomas, 2 epidermoid, and 1 lipoma) (Table 1), as well as on a control group consisting of 23 healthy controls matched for age, sex, and years of education (mean age 53.4±14.1, range 21–72 years; 9 males, 14 females). Regarding clinical histories, one patient (R19) had previously undergone gamma knife radiosurgery, and two patients (L10 and L17) had recurrent tumors. Patients were excluded for the following reasons: age under 20 or over 78 years; lesions involving non-cerebellar cortical or subcortical regions; history of alcohol or drug abuse; or pre-existing psychiatric disease. Neurological examinations of gait, kinetic function-arm, kinetic function-leg, speech, and eye movements were conducted based on the Brief Ataxia Rating Scale [15]. All patients showed normal performance except for two cases (R2 and R7) who walked almost naturally, but were unable to walk with their feet in the tandem position. The locations of the cerebellar tumors are shown in Fig. 1 and Table 2. Notably, the tumor compressed the posterior lateral cerebellum in all patients, especially lobule VI and Crus I (Fig. 1 and Table 2). Lesion size was measured in milliliters on preoperative MRI, according to the formula; $a \times b \times c/2$, where a and b indicate the longest crossed dimension of the horizontal plane, and c indicates the greatest length of the tumor in the coronal plane.

Informed Consent and Approval

All patients and control subjects provided written informed consent for this investigation. The study was approved by the ethical committee of the University of the Ryukyus.

Experimental Design

In the preoperative stage, 28 patients with cerebellar lesions underwent neuropsychological assessments and 19 patients participated in the fMRI examination. The fMRI study was conducted once before surgical treatment. In the postoperative stage, 12 patients with right cerebellar tumors (mean age 45.0 ±11.5 years, range 21–64 years; 3 males, 9 females)

Table 1 Summary of 28 patients examined by neuropsychological assessment

Patient number	Sex/age/handedness	Diagnosis	Lesion side	Size of lesion (mL)	Follow-up assessment	fMRI study (preop)
R1	F/38/right	Meningioma	Right	3.41		
R2	M/21/right	Schwannoma	Right	50.56	+	
R6	M/61/right	Schwannoma	Right	0.27	+	
R7	F/42/right	Schwannoma	Right	18.31	+	+
R10	F/51/right	Meningioma	Right	6.55	+	+
R11	M/64/right	Epidermoid	Right	2.66	+	+
R12	F/34/right	Meningioma	Right	3.46	+	+
R13	F/52/right	Meningioma	Right	5.85	+	
R14	M/63/right	Schwannoma	Right	7.95		+
R15	M/76/right	Schwannoma	Right	5.79		
R16	F/50/right	Meningioma	Right	5.79	+	+
R17	M/49/right	Schwannoma	Right	3.68	+	+
R18	F/40/right	Schwannoma	Right	11.7	+	+
R19	M/60/right	Schwannoma	Right	5.22		+
R20	F/40/right	Meningioma	Right	0.42	+	+
R21	F/36/right	Meningioma	Right	7.71	+	+
R22	F/63/right	Meningioma	Right	13.51		+
L2	M/49/right	Meningioma	Left	3.82		
L4	F/48/right	Schwannoma	Left	27.34		+
L9	F/55/right	Schwannoma	Left	3.18		
L10	F/47/right	Schwannoma	Left	4.69		+
L11	F/69/right	Meningioma	Left	5.68		+
L12	F/59/right	Epidermoid	Left	3.97		
L13	M/53/right	Lipoma	Left	0.79		+
L14	M/38/left	Schwannoma	Left	25.94		
L15	F/62/right	Schwannoma	Left	0.25		+
L16	M/55/right	Epidermoid	Left	13.55		+
L17	F/38/right	Schwannoma	Left	16.89		+

"+" indicates participation in the follow-up assessment or fMRI study

M male, *F* female

underwent follow-up neuropsychological assessments in order to examine whether surgical intervention had an effect on functional recovery. Detailed individual profiles are shown in Table 1.

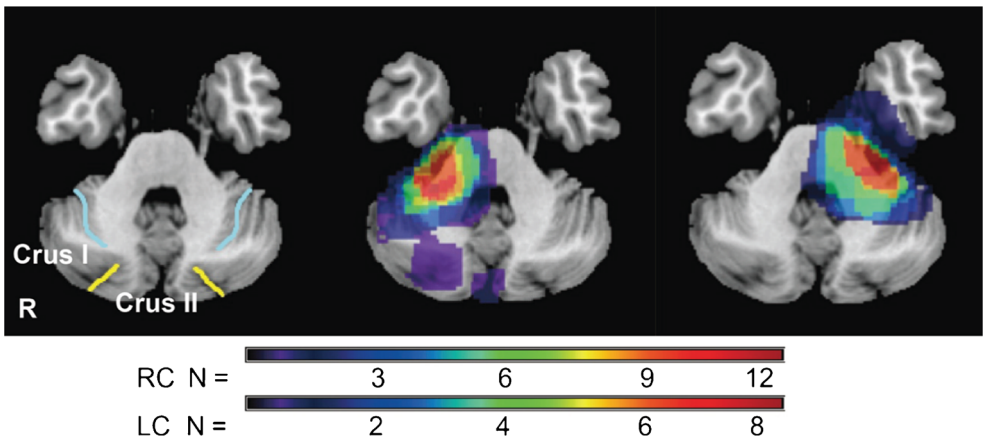

Fig. 1 Tumor topography of right (*middle image*, $n=17$) and left cerebellar tumors (*right image*, $n=11$). *Light blue line* indicates the superior posterior fissure; *yellow line* indicates the horizontal fissure in the left image

Table 2 Lesion characteristics in patients with cerebellar tumors

	Hemisphere											
Case code	I	II	III	IV	V	VI	Crus I	Crus II	VII B	VIII	IX	X
Right side												
R1							×	×				
R2			×	×	×	×	×	×	×	×	×	×
R6												×
R7			×	×	×	×	×	×		×	×	×
R10						×	×	×	×	×		
R11				×	×	×	×	×	×	×		
R12						×	×	×	×	×		×
R13							×	×	×	×		
R14			×	×	×	×				×	×	×
R15				×	×	×						×
R16			×	×	×	×	×	×	×	×		×
R17			×	×	×	×				×		×
R18						×	×			×	×	×
R19				×	×	×	×	×	×	×	×	×
R20						×	×		×			
R21				×	×	×	×	×	×			×
R22			×	×	×	×	×		×	×		×
Left side												
L2			×	×	×	×						×
L4			×	×	×	×	×	×	×	×	×	×
L9						×				×		×
L10				×	×	×	×		×	×		×
L11				×	×	×	×	×	×	×		×
L12				×	×	×	×	×	×	×		×
L13												×
L14			×	×	×	×	×	×	×	×		×
L15												×
L16			×	×	×	×						×
L17			×	×	×	×						×

"×" denotes the existence of a tumor at preoperative stage. "×" indicates the residue at postoperative stage

Neuropsychological Assessment

The battery consisted of the following tests: (I) mini-mental state examination (MMSE) [16] and modified MMSE (3MS) [17] for global cognitive screening, (II) Trail Making Test (TMT) [18] and Stroop test (ST) [18] for executive function, (III) Wechsler Adult Intelligence Scale-Revised (WAIS-R) digit span subtest (DS) [19] for working memory, (IV) WAIS-R DST [19] for psychomotor speed, (V) partial WAIS-R block design subtest (fifth and ninth items) [19] and the cube-copying test for visuospatial ability. For quantitative assessment of constructional ability in the cube-copying test, the points of connection and plane-orientation errors were evaluated. A point of connection was defined as a point at which three lines met to form a vertex, hence subjects could score up to eight points, since eight points of connection are present in a cube. Each plane with two pairs of parallel lines was evaluated in terms of the number of lines and the extent to which they were parallel. No plane-error points were scored if the cube was copied accurately [20]. We selected brief neuropsychological tests that could be performed within 1 h in order to reduce the burden on patients in the preoperative or postoperative therapeutic stage. As for the duration of patients' follow-up, we carried out of the assessment within 6 months after resection of the tumor. Patient R2 with a huge schwannoma showed transient neurological symptoms related

to the IVth nerve. The double vision by such nerve injury influenced cognitive performance, so we followed up the patient until recovery of its symptom.

Event-Related fMRI Study

Subjects

Twelve patients with right cerebellar tumors (mean age 46.9± 13.3 years, range 17–66 years; 3 males, 9 females), 7 patients with left cerebellar tumors (mean age 53.3±10.1 years, range 38–69 years; 2 males, 5 females), and 30 normal healthy volunteers (mean age 24.0±5.2 years, range 22–35 years; 21 males, 9 females) were enrolled in this study (Table 1). The normal healthy volunteers that participated in the fMRI study were different from those included in the neuropsychological analysis. Standard values in each generation of the correct response rate in fMRI behavioral task were not established. Therefore, to estimate a normal value of the correct response rate, we recruited healthy young subject. None of these patients had any signs or history of neurological or psychological diseases. This study was approved by the ethical committee of the University of the Ryukyus with written informed consent obtained from all participants. Subjects were all right-handed according to the Edinburgh Handedness Laterality Index, with a median score of 100 (range 80–100).

Experimental Paradigm

The fMRI behavioral paradigm used was a rapid event-related fMRI design [14, 21, 22] based on an explicit three-alternative forced choice task including novel (new), repeated (same), and lure (similar) stimuli consisting of color photographs of common objects. A fully randomized functional run consisted of 108 total trials, 16 lure sets, 16 repeat sets, and 44 unrelated novel items (foils) (Fig. 2). Forty-four foil trials, 16 trials first presented from repeat sets, and 16 trials first presented from lure sets were presented as the new stimuli. The same stimuli were 16 trials, which are second presented from repeat sets. The lure stimuli were 16 trials which are second presented from similar sets. Each stimulus was presented for 2,500 ms with a 0–1,000 ms interstimulus interval to prevent adaptive stimulus responses. The number of trials separating similar and identical pairs was randomly varied from 10 to 40 trials. Several photographs were displayed to participants on a goggles display during the session. If the photograph was first presented in the session, participants were required to press the *red* button indicating a new object. If the photograph had been displayed before in the session, examinees were instructed to press the *blue* button indicating a repeated object. Finally, if they thought that the photograph was similar to, but not the same as previous stimuli, they were required to press the *green* button, indicating a similar but not identical object. Responses and reaction times were recorded in a button box (Current Designs, Inc., Philadelphia, Pennsylvania). Visual stimuli were presented to the subjects using 800×600 resolution magnet-compatible goggles under computer control (Resonance Technologies, Inc., Salem, Massachusetts) using Presentation® software (Neurobehavioral Systems, Inc., Austin, Texas).

MRI Data Acquisitions

Anatomical and functional images were obtained using a 3-T MRI scanner (Discovery MR750; GE Medical System, Waukesha, Wisconsin, USA) with a 32-channel head coil and high-order manual shimming to the temporal lobes. The array spatial sensitivity encoding technique (a parallel imaging technique) was used to acquire imaging data by reducing geometric distortion for echo planar imaging (EPI). The anatomical three-dimensional (3D) spoiled gradient recalled echo (SPGR) sequence was obtained with a high-resolution 1-mm slice thickness (matrix size 256×256, field of view 256×256 mm, repetition time 6.9 ms, echo time 3 ms, flip angle 15°). T2*-weighted EPI sequence was used to measure BOLD contrast (repetition time 1,500 ms, echo time 25 ms, flip angle 70°, matrix size 128×128, field of view 192×192, in-plane resolution 1.5×1.5 mm^2, 23 slices, 3-mm thickness, 0-mm space). A total of 303 volumes were collected over one session during the experiment in a sequential ascending order. A high-resolution T2 fast spin echo (T2 FSE) sequence (repetition time 4,300 ms, echo time 92 ms, matrix size 512×512, field of view 192×192, in-plane resolution 0.375×0.375 mm^2, 23 slices, 3-mm thickness, 0-mm space) was obtained for the co-registration of 3D SPGR and EPI functional images. EPI functional images and T2 FSE structural images were acquired in an oblique coronal plane perpendicular to the long axis of the hippocampus. Almost the entire hippocampus (head, body, and tail) was included in the 23 slices. Functional images were localized in the sagittal plane of the SPGR image to identify the long axis of the hippocampus. Oblique coronal slices were fitted to the principal longitudinal axis of the hippocampus covering the entire bilateral medial temporal lobes. Firstly, distortions of fMRI signals were corrected by array spatial sensitivity encoding techniques, which were used to improve temporal and spatial resolution and reduce artifacts. Secondly, higher order shims were employed to directly compensate for local field distortions. These methods guaranteed homogeneity of the magnetic field.

Preprocessing and Estimations

Functional and structural MR images of the brain were preprocessed using the methods of realignment, temporal correlation, spatial normalization, and spatial smoothing. The data were analyzed using SPM8 software (Wellcome Trust

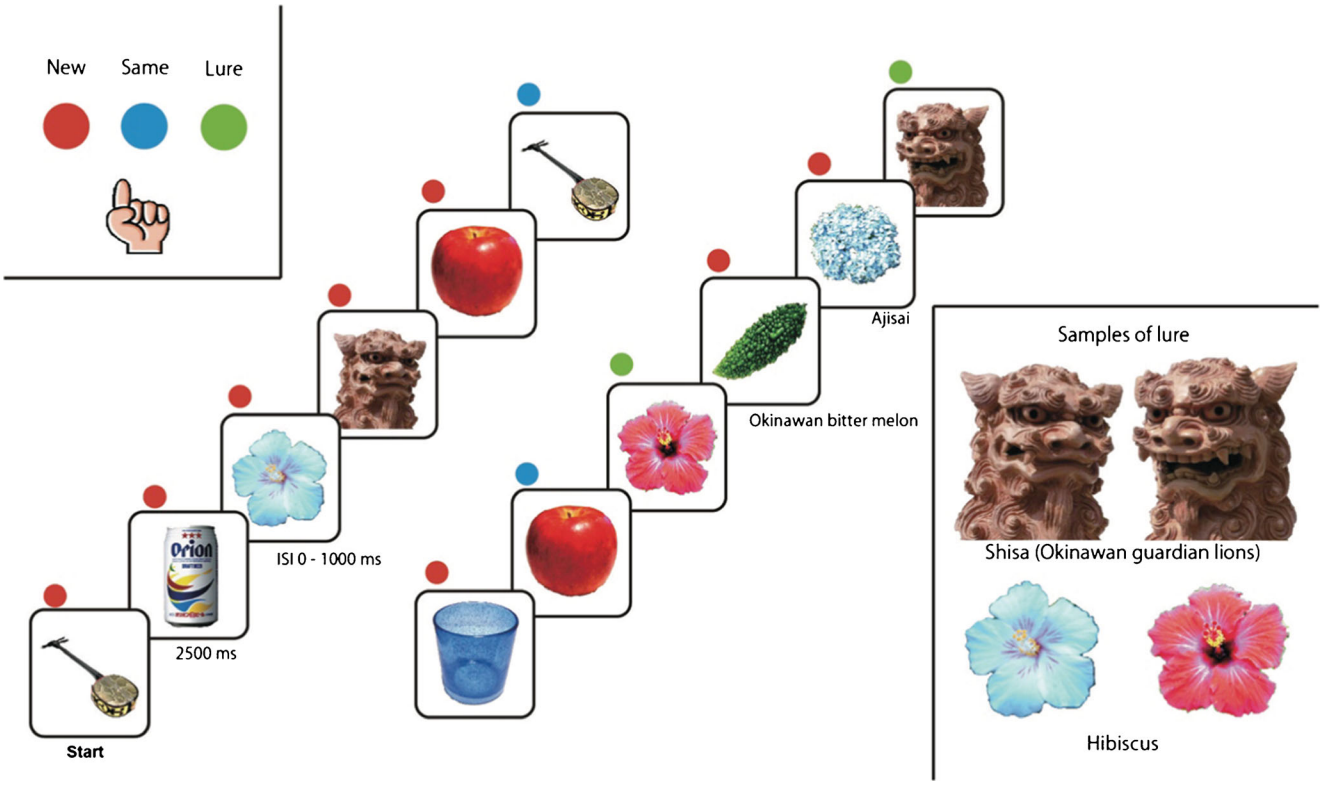

Fig. 2 fMRI behavioral task. Images of single items were presented for 2,500 ms followed by a 0–1,000 ms interstimulus interval. Novel, repeated, and similar lure items were randomly shuffled in the task. *Upper left insets* show three task buttons for new (*red*), lure (*green*), and repeated (*blue*) stimuli. *Lower right insets* show examples of lure pairs; Okinawa guardian lions and hibiscuses

Centre for Neuroimaging, University College London, London, UK). The first five volumes in each data set were removed to ensure that the signal reached a steady state. EPI functional images were corrected to account for the differences in slice acquisition times by interpolating the voxel time series using sinc interpolation and resampling the time series using the center slice as the reference point. The EPI functional images were then corrected for motion artifacts by realignment to the first volume. A mean EPI functional image was constructed during realignment. Co-registration was performed through two processes. Both the mean EPI functional image and the motion-corrected EPI functional images were co-registered to the T2 FSE structural image. The co-registered T2 FSE structural image was then co-registered to the structural SPGR image. Next, the registration points of the anterior and posterior horns of the lateral ventricle, top surface of the paracentral lobule, and bottom surface of the inferior temporal gyrus were checked in the T2 FSE structural, structural SPGR, and EPI functional images. Before spatial normalization, a parameter was produced by the segmentation process from the structural SPGR image. The structural SPGR image and EPI functional images were spatially normalized ($1 \times 1 \times 1$ mm) using the Montreal Neurological Institute space. Finally, the images were spatially smoothed using a Gaussian kernel with a full width at a half maximum of 3 mm. To detect the brain activation associated with a specific task while simultaneously reducing noise, the size of the smoothing kernel was kept at a recommended 2 to 3 times the voxel size [23]. A high-pass filter regressor (200 s) was included in the design matrix to exclude low-frequency noise and artifacts. To identify the correct activation spots of the brain, movement effects were discounted in a number of rows (298) and columns (3 translations and 3 rotations). For each subject, the three (new, lure, and repeated) regressors were estimated by a general linear model calculated by applying a canonical hemodynamic response function combined with time and dispersion derivatives. To assess the main effect of the lure images, as characterized by both the hemodynamic response function and these derivatives, an F-contrast obtained by the F test was required. Intra-individual activation maps were calculated by F tests. We calculated second-level group contrasts using a one-sample t test for each regressor (new, lure, and same) from the response of the canonical hemodynamic function. Differences in the intensities of the activation between task conditions were confirmed by a voxel-level threshold of $p<0.001$ uncorrected, and a cluster-level threshold of FWE (family-wise error)-corrected $p<0.05$. We extracted the average percent signal change values of the regions of interest (ROIs) from the anatomically defined AAL ROI atlas [24] and established 3D MRI atlases [25–27] for each subject and type of task stimuli using the MarsBar toolbox [28].

Global Brain Connectivity Analysis

Subjects

Twelve patients with right cerebellar tumors (mean age 46.9± 13.3 years, range 17–66 years; 3 males, 9 females), 7 patients with left cerebellar tumors (mean age 53.3±10.1 years, range 38–69 years; 2 males, 5 females), and 15 right-handed healthy volunteers (mean age 27.6±6.5 years, range 20–44 years; 5 males, 10 females) were enrolled in this study. The normal healthy volunteers participating in the resting-state fMRI study were different from those included in the neuropsychological analysis and the event-related fMRI experiment. No participants had any signs or history of neurological or psychological diseases. This research was approved by the ethical committee of the University of the Ryukyus, and written informed consent was obtained from all participants.

Acquisition of Resting-State fMRI Data

Functional and anatomical images were obtained using a GE Discovery MR750 3.0 Tesla MRI scanner (GE Medical System) with a 32-channel head coil. In order to minimize head movement, the heads of each of the participants were fixed using foam pads. In order to reduce geometric distortion in EPI, a parallel imaging technique known as the array spatial sensitivity encoding technique was used during imaging data acquisition. T2*-weighted EPI images were used to measure BOLD contrast (repetition time 2,000 ms, echo time 30 ms, flip angle 70°, matrix size 64×64, field of view 256×256, in-plane resolution 4× 4 mm, 42 slices, 4-mm thickness, 0-mm space). During EPI image scanning, participants were instructed to remain motionless, remain awake, relax with their eyes closed, and to try not to think about anything in particular. A total of 150 volumes were collected over one session in a sequential ascending manner (plus 5 initial discarded volumes). An anatomical three-dimensional spoiled gradient recalled echo (3D SPGR) sequence was obtained with high-resolution 1-mm slice thickness (matrix size 256× 256, field of view 256×256 mm, repetition time 6.9 ms, echo time 3 ms, flip angle 15°). A high-resolution T2 fast spin echo (T2 FSE) sequence (repetition time 4,300 ms, echo time 92 ms, matrix size 256×256, field of view 192×192, in-plane resolution 1.33×1.33 mm, 42 slices, 4-mm thickness, 0-mm space) was obtained for the co-registration of 3D SPGR images and EPI functional images. EPI functional and T2 FSE structural images were acquired in an oblique axial transverse plane (tilted 30° anterior relative to the intercommissural plane).

Preprocessing and Analysis of Resting-State fMRI Data

Following this step, fMRI preprocessing, analysis, and visualization methods were conducted as implemented in SPM (8 package, http://www.fil.ion.ucl.ac.uk/spm8/) and the "conn" toolbox (www.nitrc.org/projects/conn). Images were corrected for slice acquisition time within each volume, motion corrected with realignment to the first volume, spatially normalized to the standard MNI EPI template, and spatially smoothed using a Gaussian kernel with a full width at half maximum of 8 mm. 3D SPGR images were co-registered with each mean EPI and T2 FSE image, and averaged together to permit anatomical localization of the functional connectivity at the group level. The transformed structural images were segmented into gray matter (GM), white matter (WM), and cerebrospinal fluid (CSF) using a unified segmentation algorithm.

In addition to removing noise correlations present in WM and CSF, the addition of six motion regressors (six realignment parameters and first derivatives) controlled for correlations due to movement. Data were filtered between 0.009 and 0.08 Hz.

Correlation Analysis with Global Brain Connectivity and the Lure Task

A map of GBC was computed from resting-state fMRI data using the "conn" toolbox (www.nitrc.org/projects/conn) [29, 30]. In the "conn" toolbox, correlation maps were calculated on the basis of seed-based correlation analysis using the AAL ROI atlas [24]. When the population correlation coefficient is zero, the distribution of correlation coefficient is consistent with the normal distribution. However, normal distribution of the correlation coefficient is lost when the correlation coefficient approximates to 1 [31]. Each ROI's correlation coefficient map was transformed by Fisher's Z transformation to Z value maps in order to normalize the correlation coefficient.

These Z value maps were averaged together across each subject in order to calculate GBC values. For correlation analysis of the GBC and score of the lure task, GBC values were extracted from the ROIs that were activated by the lure stimulus in the event-related fMRI experiment. The Pearson product–moment correlation coefficient was used to calculate correlations between GBC values and the correct response rates in the lure task. When the correlation coefficient was close to +1, the r value indicated a proportional connection between GBC values and the scores in the lure task (positive correlation). Conversely, when the correlation coefficient was close to −1, the r value showed an inverse proportion (negative correlation). We estimated the strength of the correlation in five categories: negligible correlation (0.00 to 0.30 or 0.00 to −0.30), low correlation (0.30 to 0.50 or −0.30 to −0.50), moderate correlation (0.50 to 0.70 or −0.50 to −0.70), high correlation (0.70 to 0.90 or −0.70 to −0.90), and very high correlation (0.90 to 1.00 or −0.90 to −1.00) [32].

Statistical Analysis

The Kruskal-Wallis test for three independent samples or the Mann–Whitney U test for two independent samples was used

to evaluate statistical significance in the neuropsychological assessments and fMRI behavioral tasks, since a normally distributed population could not be assumed. Preoperative and postoperative neuropsychological data were compared using the Wilcoxon signed rank test. Statistical significance was accepted at $p<0.05$. The chi-square test was used to evaluate the performance in the block design subtest, since only two items of the block design subtest were evaluated as pass/fail.

Results

Preoperative Neuropsychological Profile of Patients with Benign Cerebellar Tumors

The results of the neuropsychological test of DST ($p<0.05$), forward span of DS ($p<0.05$), backward span of DS ($p<0.01$), and total score of DS ($p<0.05$) among patients with cerebellar tumors ($n=27$) indicated a significant impairment as compared with the control group, which was further confirmed using the Mann–Whitney U test. To examine whether the profile of the impairments depended on the side of the lesion, patients with right and left tumors were compared to the control group. Performance on neuropsychological tests including MMSE, DST, forward span of DS, backward span of DS, total score of DS, and cube-copying test significantly differed across groups. Patients with right cerebellar tumors performed significantly worse than the control group on DST ($p<0.001$), forward span of DS ($p<0.010$), backward of DS ($p<0.001$), and total score of DS ($p<0.05$), as indicated by a post hoc Mann–Whitney U test with Bonferroni correction (Table 3). In contrast, there were no significant impairments in left-sided tumors as compared to the control group (Table 3). A Mann–Whitney U test was used to confirm that patients with right-side tumors showed significantly lower scores on the MMSE when compared with patients with left-side tumors ($p<0.05$) (Table 3). No direct relationship was found between tumor size and scores on neuropsychological assessments, with the exception of the DST ($r=-0.48$, $p<0.05$). None of subjects failed the fifth item of block design test. Chi-square analysis of the performance of the ninth item on the block design subtest revealed no significant difference between patients with right or left cerebellar tumors and the control group.

Postoperative Neuropsychological Profile of Patients with Benign Cerebellar Tumors

Since most neuropsychological tests showed a significant decline in patients with right-sided tumors as compared with the control group at the preoperative stage, 12 patients with right cerebellar tumors were further tested 2 weeks to 18 months after resection of the tumor in order to investigate whether cognitive function became normalized after surgical decompression of the posterior lateral cerebellum. T1-weighted MRI confirmed that the decompressed cerebellum, especially lobule VI and Crus I had completely recovered after treatment (Table 2 and Fig. 3). Comparison of preoperative and postoperative neuropsychological tests revealed improvements in the raw scores of DST from 8.33±3.20 to 8.92±3.23, DS forward span from 6.08±1.16 to 6.25±1.60, DS backward span from 4.08±0.90 to 4.58±1.73, and DS total score from 9.92±3.06 to 10.83±4.59. However, no significant difference was found between neuropsychological assessments because of the small sample size (Table 4).

Hippocampal Function

Analysis of the reaction times for new, lure, and repeated task revealed no significant difference across groups (Fig. 4a–c). However, a significant decline was observed in the correct response rates during lure tasks in patients with right cerebellar tumors (13±18 %; $n=12$, age 53.4±13.4 years) ($P=0.0003$) compared with those of normal healthy volunteers (46.3±3.3 %; $n=30$, age 24.0±5.2 years). Furthermore, no difference was found between patients with right and left cerebellar tumors (30±18 %; $n=7$, age 53.3±10.1 years) ($P=0.25$) (Fig. 4d–f).

BOLD Responses

We confirmed the BOLD signal activity in the right DG but not left ones correlated to correct response rate of the lure task rather than error one, nor other new and similar ones in normal healthy volunteers. These results indicate a crucial contribution of right DG for the performance of pattern separation ability (Fig. 5a, b). We therefore analyzed BOLD response patterns in the right DG during lure tasks. In normal healthy volunteers, the initial dip in the BOLD response occurred at 1.7±1.3 s (mean±S.D.) in time course, followed by a fractional increase in blood flow within 3.9±4.2 s. The subsequent signal decrease was delayed by 8.3±5.1 s, and the % BOLD change from that of the resting state was −0.19±0.27, followed by a slope to a plateau or peak value for long pulses (>20 s) (Table 5 and Fig. 5c). Signal fluctuation or alteration of the BOLD pattern was found in patients with cerebellar tumors. A delayed latency of the initial positive peak (5.3±1.9 s) with a large amplitude of % BOLD change (0.190±0.060) subsequently followed by an initial dip (2.1±0.9 s) was found in patients with right cerebellar tumors (Table 5 and Fig. 5d). For patients with left cerebellar tumors, we found a rapid initial peak (3.3±1.4 s) without an initial dip, followed by a slope to a plateau value with a large S.D. value ranging from −0.18 to 0.28, indicating signal fluctuations among examinees of this group (Table 5 and Fig. 5e).

Table 3 Results of neuropsychological assessment of patients with damage to the right or left cerebellar hemispheres

Test	Cerebellar lesion		Controls, n=23	P
	Right, n=17	Left, n=11		
Age, years	49.41 (13.99)	52.09 (9.48)	53.39 (14.05)	n.s
Education, years	13.29 (1.90)	12.82 (2.04)	12.91 (2.39)	n.s
Cerebellar lesion size, mL	8.99 (11.66)	9.65 (9.86)	–	n.s.
3MS	96.18 (4.37)	97.59 (2.52)	97.50 (2.14)	n.s.
MMSE	28.53 (2.00) †	29.73 (0.90)	29.13 (1.26)	0.034
WAIS-R Digit symbol test #	8.65 (3.57)*	11.64 (3.38)	12.04 (2.44)	0.015
WAIS-R Digit span test				
Forward span	5.88 (1.05)*	6.45 (1.13)	6.86 (1.39)	0.025
Backward span	4.12 (0.86)*	4.64 (1.29)	5.43 (1.31)	0.006
Total score #	10.06 (2.70)*	11.55 (2.30)	12.08 (2.82)	0.048
TMT, s				
Part A	36.94 (11.94)	34.82 (11.16)	30.74 (8.59)	n.s
Part B	64.82 (22.74)	64.00 (26.20)	52.52 (19.61)	n.s
Part B-A	27.88 (13.61)	29.18 (19.41)	21.78 (14.20)	n.s
Stroop test, s				
Reading (I)	24.94 (4.70)	22.00 (4.38)	22.78 (4.19)	n.s
Naming (II)	33.24 (6.89)	30.64 (5.28)	30.35 (6.59)	n.s
Interference (III)	58.41 (22.61)	48.09 (15.27)	48.04 (13.62)	n.s.
III-II	25.18 (18.46)	17.45 (12.19)	17.70 (8.19)	n.s.
Cube-copying test				
Point of connection	7.00 (1.97)	7.45 (1.04)	8.00	0.011
Plane-drawing errors	0.41 (1.00)	0.45 (0.82)	0	n.s

Values are mean (standard deviation). # denotes scaled score (mean = 10, standard deviation = 3). P indicates a significant difference after Kruskal-Wallis test or Mann–Whitney U test; * indicates a significant decline compared to controls (post hoc Mann–Whitney U test with Bonferroni correction, p<0.05); † denotes a significant decline compared to patients with left lesions (post hoc Mann–Whitney U test with Bonferroni correction, p<0.05)

n.s. not significant, *3MS* modified mini-mental state examination, *MMSE* mini-mental state examination, *TMT* Trail Making Test

Correlation Analysis with Brain Activation and Lure Task

We began by detecting important regions for memory systems on the basis of the activation maps gathered from 30 healthy participants during the performance of a lure task involving pattern separation, which is an important human memory function of hippocampal circuits (Table 6). Next, we evaluated whether neural activity measured by local BOLD signal changes correlated to accurate response rates in the lure task across examinees, indicating a functional role of the regions instead of individual differences between examinees (Fig. 6a–i). The source ROIs were defined as the right DG, left anterior middle cingulate cortex (aMCC), and bilateral cerebellar lobule VI including Crus I, based on the correlation analysis of BOLD responses and percentage of correct responses in the lure task (Fig. 7a, c, e). Correct identification of source ROIs was confirmed by established 3D MRI atlases (Fig. 7b, d, f) [24–27]. Subdivisions of the rostral cingulate cortex, hippocampus, and cerebellum were painted on an individual structural SPGR image using FSLview in the FMRIB Software Library v5.0 (FMRIB Analysis Group, University of Oxford, Oxford, UK). The parameters of the GBC were extracted from the source ROIs above.

Correlation with GBC and Pattern Separation

For the GBC measure, we assessed standard resting-state fMRI data, and tested whether the right DG, left aMCC, and bilateral cerebellar lobule VI including Crus I had high GBC with the rest of the brain. The range of GBC values was from −2.1 to 1.9 in the normal control group, while patients with left and right cerebellar tumors showed more narrow ranges, from −0.09 to 0.07, and −0.07 to 0.11, respectively. The Pearson product–moment correlation coefficient was used to assess correlations between the GBC parameters of the four source ROIs and the percentage of correct responses in the lure task. The control subjects (n=15) showed moderate positive correlations with the GBC of the right cerebellar lobule VI, including Crus I (r=0.65, p<0.01), right hippocampal DG (r=0.62, p<0.01), and left aMCC (r=0.56, p<0.05) (Fig. 8a),

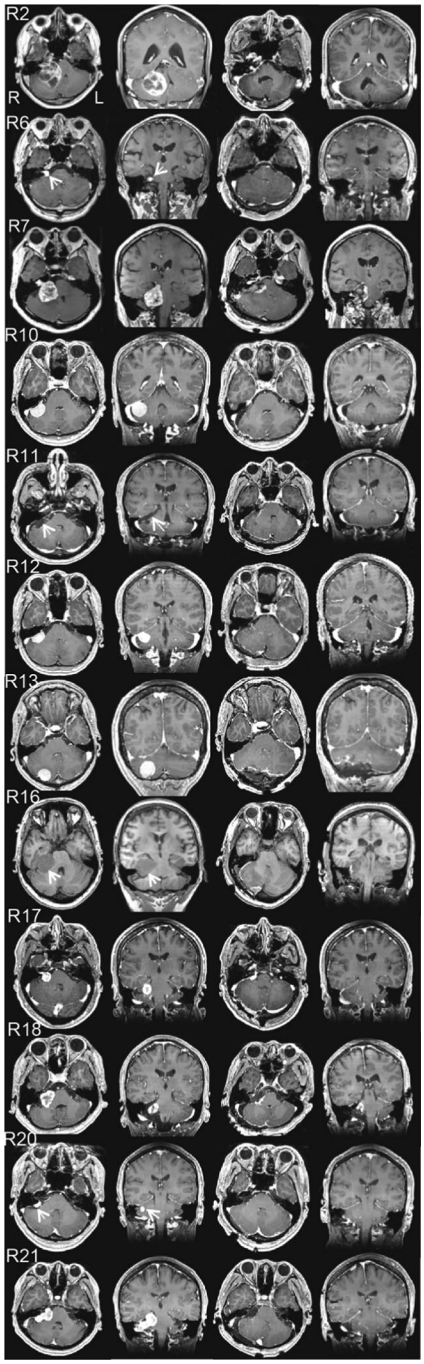

Fig. 3 Panels of pre- and postoperative gadolinium-enhanced T1-weighted MRI of cases R2, R6, R7, R10, R11, R12, R13, R16, R17, R18, R20, and R21 (from *top* to *bottom*). *Rows* show axial and coronal images before the operation, and axial and coronal images after the operation (from *left* to *right*). Since Case R16 is subject to asthma, T1-weighted MRI was performed without contrast medium

though no significant correlation was found in the left cerebellar lobule VI including Crus I (r=0.0001, p>0.05). We found that GBC connectivity correlated to correct response rates during lure tasks was limited to three regions including the right cerebellar hemisphere (lobule VI/Crus I), left aMMC, and right hippocampal DG. Herein, we raised the hypothesis that these three regions might play a crucial role in the human memory system, since rs-fMRI connectivity not only correlated to established structural connectivity, but also reflected well-known functional networks [33, 34]. Thus, GBCs in the right cerebellar hemisphere (lobule VI/Crus I), left aMMC, and right hippocampal DG were considered as the essential intrinsic connectivity of human cognition, statistically. In patients with left cerebellar tumors (n=7), high positive correlations were found in the right cerebellar lobule VI including Crus I (r=0.76, p<0.05), right DG (r=0.72, p<0.05), and left aMCC (r=0.81, p<0.01) (Fig. 8b), while the left cerebellar lobule VI including Crus I showed an extremely negative correlation (r=−0.96, p<0.001). In patients with right cerebellar tumors (n=12), significant alteration of correlations were found in the right cerebellar lobule VI including Crus I (moderate negative correlation; r=−0.64, p<0.05) and left cerebellar lobule VI including Crus I (high negative correlation; r=−0.74, p<0.01), but no correlation was found in the right DG (r=−0.04, p>0.05) or aMCC (r=−0.11, p>0.05) (Fig. 8c). These results might collectively indicate an important cerebellar contribution to pattern separation.

Discussion

We examined functional involvement of the posterior lateral cerebellum and its functional relationships with the hippocampus and the prefrontal cortex including anterior mid-cingulate cortex. Previous studies have investigated patients with cerebellar lesions such as tumors, strokes, and degenerative diseases, which frequently damage normal brain tissues. Our study evaluated patients with benign cerebellar tumors, because these lesions do not extensively destroy the surrounding normal brain tissues, so that neuropsychological assessment before and after treatment could clarify the functional involvement of the decompressed area. Human cerebellar cognitive function has been extensively studied in relation to the prefrontal cerebral cortex, but few studies have evaluated the correlation between hippocampal function and the cerebellar neocortex. Therefore, the present study also analyzed the functional activity of the posterior lateral cerebellum in relation to the hippocampus and anterior mid-cingulate cortex.

Functional Involvement of the Posterior Lateral Cerebellum

To the best of our knowledge, the present study presents the first examination of the cognitive profiles of patients with benign cerebellar tumors that compress the posterior lateral cerebellum. Neuropsychological assessments indicated that patients with right cerebellar tumors showed impairments in working memory and psychomotor speed when compared with age-matched healthy controls. Patients with right

Table 4 Neuropsychological assessment of 12 patients with right cerebellar tumors at the preoperative stage and postoperative stage

Test	Preoperative assessment	Postoperative assessment	*P*
3MS	96.28 (4.99)	97.88 (2.59)	n.s.
MMSE	29.17 (1.11)	29.25 (1.76)	n.s.
WAIS-R Digit symbol test #	8.33 (3.20)	8.92 (3.23)	n.s.
WAIS-R Digit span test			
Forward span	6.08 (1.16)	6.25 (1.60)	n.s.
Backward span	4.08 (0.90)	4.58 (1.73)	n.s.
Total score #	9.92 (3.06)	10.83 (4.59)	n.s.
TMT, s			
Part A	33.58 (10.74)	36.50 (17.20)	n.s.
Part B	59.50 (23.33)	59.92 (23.91)	n.s.
Part B-A	25.92 (13.85)	23.42 (11.75)	n.s.
Stroop test, s			
Reading (I)	24.75 (2.30)	25.17 (3.79)	n.s.
Naming (II)	32.42 (4.64)	33.83 (7.76)	n.s.
Interference (III)	52.58 (18.92)	49.25 (14.64)	n.s.
III-II	20.17 (16.08)	15.42 (9.24)	n.s.
Cube-copying test			
Point of connection	7.33 (1.79)	7.92 (0.29)	n.s.
Plane-drawing errors	0.33 (0.89)	0	n.s.

Values are mean (standard deviation). # denotes a scaled score (mean=10, standard deviation=3). n.s. denotes not significant after a Wilcoxon singed rank test

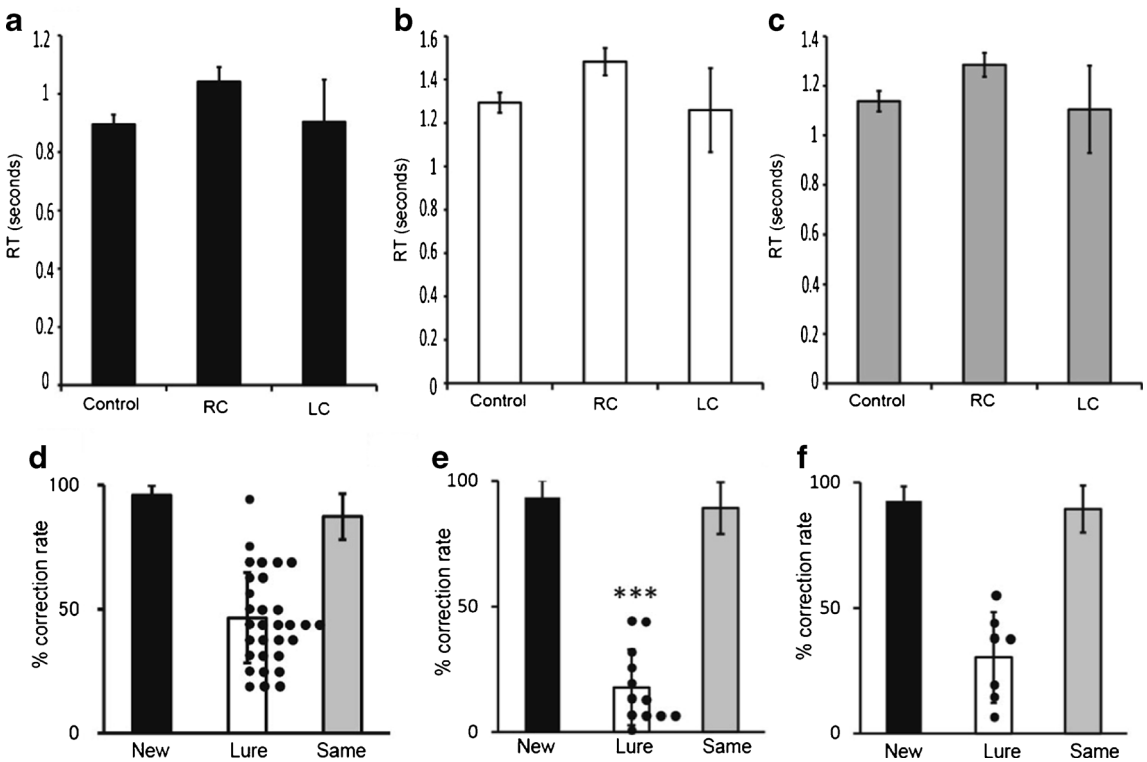

Fig. 4 Pattern separation task examined by fMRI. **a**–**c**. Reaction times (RT) for new (**a**), lure (**b**), and repeated (**c**) tasks. Control indicates normal healthy volunteers (n=30); RC, patients with right cerebellar tumors (n=12); LC, patients with left cerebellar tumors (n=7). *Bars* indicate mean; *Dots*, scores of individual cases. **d**–**f**. Percentage of correct response to new, lure, and repeated tasks in normal healthy volunteers (**d**), patients with right cerebellar tumors (**e**), and patients with left cerebellar tumors (**f**). *** in **e** indicates significant decrease compared to control (p<0.001, Mann–Whitney U test)

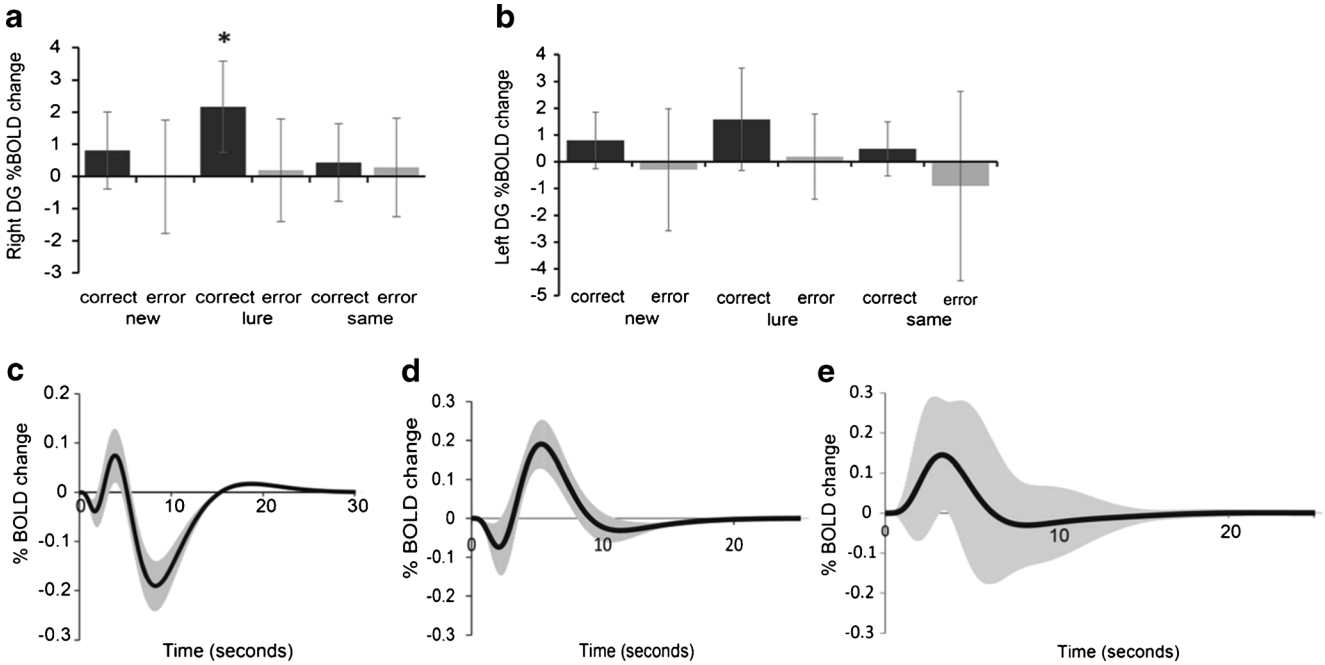

Fig. 5 BOLD response by pattern separation task. **a**–**b**. *Bar graph* showing BOLD responses in the *right* and *left* DG for correct and error responses of the new, lure, and same tasks in normal healthy volunteers. Correct responses in the lure task were increased during activation of the right DG more so than correct and error responses in other tasks (n=30) (two-way ANOVA, F=4.52, p<0.001, multiple comparisons two-sided test with Bonferroni-corrected critical p<0.05) (**a**). There was no significant difference in % BOLD change in the left DG caused by responses and/or tasks (two-way ANOVA, F=1.79, p=0.13) (**b**). *y*-axis indicates the magnitude of the % BOLD change. * denotes a significant increase compared to other conditions (p<0.05). *Graphs* showing the average BOLD curve for the lure task in normal healthy volunteers (**c**, n=30), that of patients with right cerebellar tumors (**d**, n=12), and that of patients with left cerebellar tumors (**e**, n=7). The *black line* shows the average BOLD curve and the *gray line* shows standard deviation. The *x*-axis represents time course (s) of the percentage of BOLD change. The *y*-axis represents the magnitude of % BOLD change, or the percentage BOLD signal change from the resting to stimulus condition

cerebellar tumors also showed lower scores in MMSE than patients with left-sided tumors. We tried to interpret these cognitive declines with the view that the cerebellum contributes to intrinsic functional connectivity. The laterality and disease dominancy of cerebellar tumors may therefore be important. With regard to crossed cerebello-cerebral connections, patients with right-sided cerebellar lesion showed impairments in verbal tasks, whereas patients with left-sided tumors showed deficits in spatial tasks [35, 36]. Several studies have suggested a similar laterality in cognitive symptoms [37–39], and imaging studies have elucidated cerebellar topography and lateralization effects [40, 41]. Imaging studies [40, 41] have shown that activation peaks in language tasks were lateralized to the right lobule VI and lobule VII. In contrast, spatial processing showed greater left hemisphere activation, predominantly in lobule VI [40] and lobule VII [41]. Consistent with these imaging and clinical findings, Wang et al. [42, 43] reported cerebellar symmetry in relation to cerebral intrinsic functional connectivity. They indicated a right-lateralized cerebellar network including crus I/II and a portion of lobule VI, which couples to a left-lateralized cerebral network involving the inferior frontal gyrus, superior temporal

Table 5 Latency and amplitude of BOLD in the lure task in normal healthy subjects and patients with cerebellar tumors

Peak	Mean (SD) latency (second)			Mean (SD) amplitude (% BOLD change)		
	Normal (n=30)	RC (n=12)	LC (n=7)	Normal (n=30)	RC (n=12)	LC (n=7)
N1	1.7 (1.3)	2.1 (0.9)	0.2 (1.1)	−0.039 (0.165)	−0.074 (0.070)	0.000 (0.000)
N2	8.3 (5.1)	None	None	−0.191 (0.272)	None	None
P1	3.9 (4.2)	5.3 (1.9)	3.3 (1.4)	0.074 (0.292)	0.190 (0.060)	0.140 (0.140)

RC indicates patients with right cerebellar tumors; LC, patients with left cerebellar tumors. The first negative peak is defined as N1, second negative peak as N2, and first positive peak as P1. None indicates the absence of a peak

Table 6 Significant whole-brain activations for the lure task

Region	Cluster size	Peak of *T* value	Peak coordinates		
			x	*y*	*z*
Rt. cerebellar lobule VI/Crus I	10,064	13.18	−32	−47	−33
Lt. cerebellar lobule VI/Crus I	8,572	12.96	35	−54	−22
Lt. lateral prefrontal cortex	12,393	12.25	57	10	29
Lt. caudate nucleus	4,885	11.45	13	6	11
Lt. middle cingulate gyrus	19,034	11.07	3	11	42
Rt. lateral prefrontal cortex	8,725	10.74	−49	9	25
Rt. caudate nucleus	5,150	8.73	−13	11	2
Rt. hippocampus including DG	1,859	8.51	−20	−36	−6
Rt. middle frontal gyrus	1,927	7.32	−33	2	55

Voxel-level threshold at $p<0.001$ uncorrected, corrected for multiple comparisons (family-wise error) to $p<0.05$ using a cluster threshold

Rt right, *Lt* left, *DG* dentate gyrus

gyrus, and temporal pole in the cerebral cortex. These regions include traditional language areas in the cerebral cortex, such that the cerebellar regions are commonly activated by language-related tasks. In our study, patients with right cerebellar tumors showed lower scores on the MMSE than patients with left-side tumors. Language processing is the main cognitive demand of the MMSE. Compression of the portions of the right lobule VI and Crus I connected with language areas alters the right-lateralized cerebellar network that supports language processing, which may lead to MMSE scores in patients with right cerebellar tumors. In the working memory test, lesion studies revealed that the inferior cerebellum was associated with performance on digit span test [13, 44]. There are laterality differences within the inferior lobe of cerebellum. The left inferior lobe of cerebellum is associated with the processing of aural information, whereas the right inferior lobe is involved in visual information [12]. Damage to left inferior cerebellar lobule VIII has been shown to reduce auditory digit span [44]. However, Ravizza et al. [13] revealed that performance on the auditory digit span test was unaffected by laterality of the damaged cerebellar hemisphere. Inconsistent with previous studies, the present study shows that patients with right-sided tumors exhibited impairment in the performance of the digit span test when compared with normal healthy volunteers. Chen and Desmond [11] hypothesized two cerebro-cerebellar networks for verbal working memory: the frontal/superior cerebellar network involving the right cerebellar lobule VI, Crus I, and Broca's area, which is associated with articulatory rehearsal; and the parietal/inferior cerebellar network involving the right cerebellar lobule VIIB and inferior parietal lobe, which is related to maintenance/storage of information. In the present study, impairment on working memory in patients with right-sided tumors might be related to some change in the neural bases for processing verbal working memory caused by tumor compression in the right superior and inferior cerebellum. We also found that psychomotor speed was disturbed in patients with right cerebellar tumors compared with control subjects. DST is a psychomotor performance test thought to be affected by various cognitive demands, such as motor skill, attention, and visuomotor coordination [18]. Fronto-parietal cortical networks are related to performance on the DST, and these activations reflect the processes of visual searching and updating of working memory [45]. Since patients with right cerebellar tumors also exhibited impairment of working memory, the intrinsic functional connectivity between the left fronto-parietal network coupled with the right cerebellar hemisphere might be altered by compression. We suspected that the cognitive impairments of patients with right cerebellar tumors were related to alteration of cerebellar contributions to intrinsic functional connectivity. A huge tumor may secondary compress the dentate nucleus of the human cerebellar nuclei as well as direct compression of posterior lateral cerebellum. The nucleus conjuncted with neocortex and reported an important role for human learning and cognition [46].

We found an improvement in the raw scores of some of the neuropsychological tests after surgical intervention associated with anatomical normalization of the lateral posterior cerebellum. At the postoperative stage of neuropsychological estimation, some patients with no improvements in psychomotor speed showed transient neurological symptoms related to the IVth or VIth cranial nerve function. Double vision might be a factor in preventing optimal performance. However, follow-up neuropsychological assessments in patients with cerebellar lesions have been limited [39, 47]. These previous findings [39, 47, 48] might suggest that the cerebellum can recover from pathological insult by changing the relationships of cerebral connectivity. Further studies are required to identify the detailed mechanisms behind the restoration of cognitive function following treatment of cerebellar lesions.

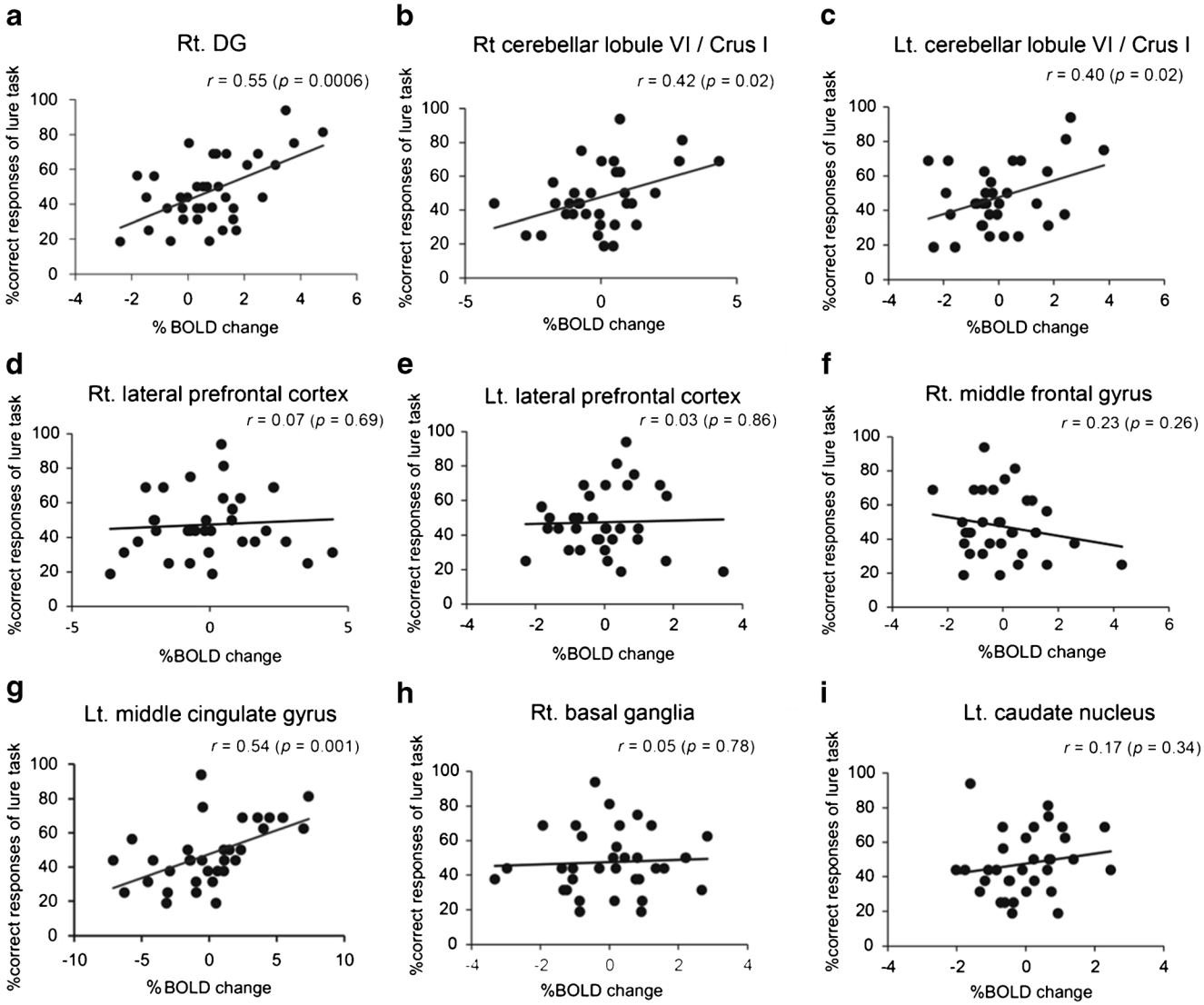

Fig. 6 Regions related to pattern separation ability. Graph (**a** to **i**) showing correlation of percentage of correct responses of the lure task and that of BOLD signals in control subjects (n=30). Hippocampus including dentate gyrus (DG) (**a**), right cerebellar lobule VI including Crus I (lobule VI/Crus I) (**b**), left lobule VI/Crus I (**c**), right lateral prefrontal cortex (**d**), left lateral prefrontal cortex (**e**), right middle frontal cortex (**f**), left middle cingulate gyrus (**g**), right basal ganglia (**h**), and left caudate nucleus (**i**). The percentage of correct responses in the lure task was significantly correlated with BOLD signals in right DG (**a**), right lobule VI/Crus I (**b**), left lobule VI/Crus I (**c**), and left middle cingulate cortex (**g**). No significant relationships were observed in the percentage of BOLD signals in the right and left lateral prefrontal cortex, right middle frontal cortex, right basal ganglia, and left caudate nucleus. The r value indicates the correlation coefficient of the Pearson product–moment (**a**–**i**). The p value indicates the significance level of the correlation coefficient. When the p value is lower than 0.05, the significance of correlation coefficient is accepted. x-axis represents the magnitude of % BOLD change that represents the rate of BOLD signal from stimulus to resting condition. y-axis represents the correct response rate in the lure task

Hippocampal Memory Function in Patients with Cerebellar Tumors

The involvement of the cerebellum in non-declarative memory has been previously investigated. Patients with focal cerebellar lesions showed impaired motor sequencing [10]. Such investigations provide evidence for a cerebellar contribution to procedural learning and support the idea that the cerebellum is an important anatomical component for competent skill acquisition. However, it is still unclear whether cerebellar lesions influence hippocampal episodic memory. On the other hand, the role of the hippocampus in episodic memory has been extensively studied, and the DG subregion of the hippocampus is well known as a substrate for cognition [49].

Pattern separation is a function of the DG that transforms similar experiences or events into discrete, non-overlapping representations. The DG and its projections into the CA3 subregion have been shown to be involved in pattern separation [14]. fMRI was used to observe the process of pattern separation by scanning normal subjects during an incidental

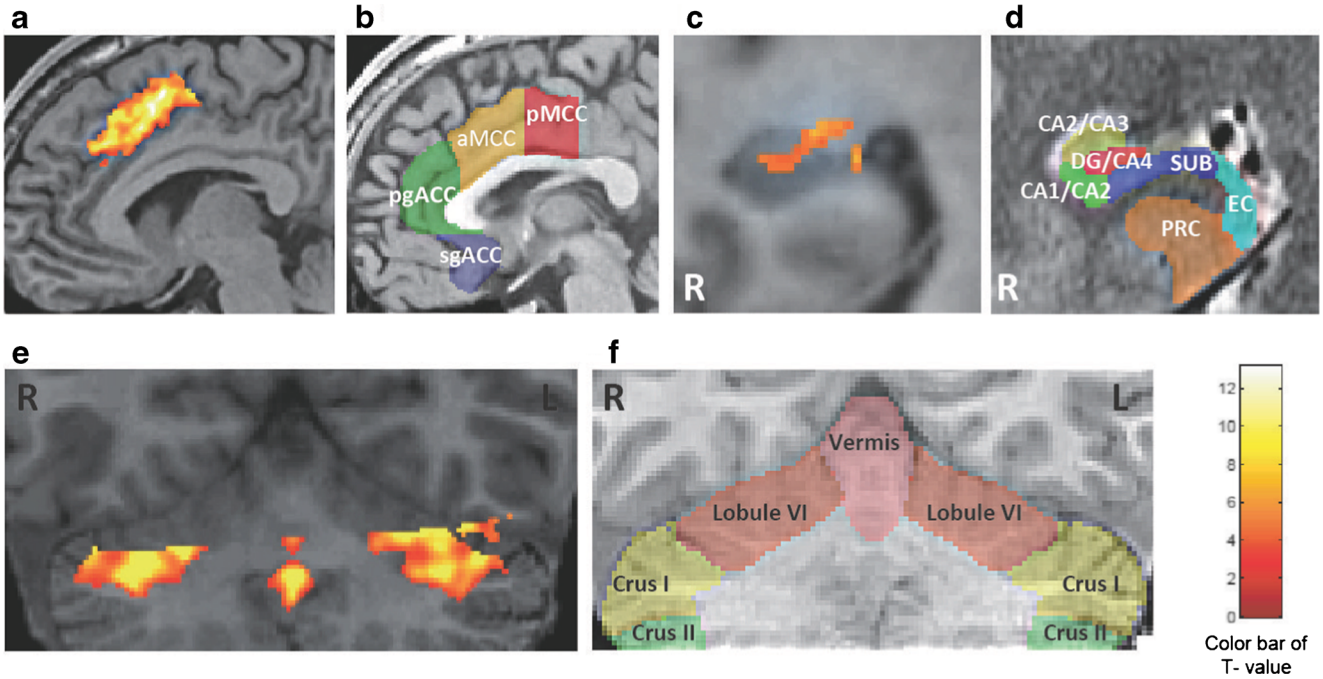

Fig. 7 Identification of source ROIs in the activation maps and topographical schemas in healthy subjects. **a**–**f**. Identification of source ROIs in the activation maps during a lure task from healthy subjects (n= 30, voxel-level threshold at $p<0.001$ uncorrected, corrected for multiple comparisons (family-wise error) to $p<0.05$ using a cluster threshold) (**a**, **c**, and **e**). Each transparent color indicates the subdivisions of the rostral cingulate cortex (**b**), right hippocampus (**d**), and cerebellum (**f**). The color maps were painted according to references [24–27], and are explained in details in the text. **b**, *transparent red*, *yellow*, *green*, and *blue*, indicate the pMCC, posterior mid-cingulate cortex; aMCC, anterior mid-cingulate cortex; pgACC, pregenual anterior cingulate cortex; sgACC, subgenual anterior cingulate cortex, respectively. **d**, *transparent red*, *yellow*, *green*, *blue*, *light blue*, and *orange* indicate the hippocampal dentate gyrus and Cornu Ammonis 4 (DG/CA4); Cornu Ammonis 2 and 3 (CA2/CA3); Cornu Ammonis 1 and 2 (CA1/CA2); subiculum (SUB); entorhinal cortex (EC); and perirhinal cortex (PRC), respectively. **f**, *Transparent pink*, *orange*, *yellow*, and *green* indicate the cerebellar vermis, and bilateral lobule VI, Crus I, and Crus II, respectively. Anatomical identification is specified in the text. Note that the aMCC in **a**, and DG/CA4 in **c**, and lobule VI and/or Crus I in **e** were selectively activated. The *color bar* indicates t values (maximum t=13.18, *white* represents the highest value). *R*, the right hemisphere. *L*, the left hemisphere

encoding task using pictures of common objects. The present fMRI study used a similar experimental paradigm to examine hippocampal memory function involvement in pattern separation in patients with cerebellar tumors. The BOLD response showed that the latency of the positive peak was significantly increased in patients with right cerebellar tumors, and these patients showed increases in the positive peak without any second negative peak. Logothetis et al. [50] reported a linear relationship between BOLD signals and neural activity. In addition, the BOLD signal was shown to represent the proportion of the cerebral blood flow (CBF) and the cerebral metabolic rate of oxygen ($CMRO_2$) [51]. The factor of gain in the positive response was interpreted as either a reduction in CBF or an increase in $CMRO_2$ [52]. Increases in BOLD responses are influenced by hemodynamics and metabolism based on the magnitude of neural response. However, the factor that exerts influence on the increase in positive BOLD responses has not yet been elucidated. Moreover, the physiological significance of the post-stimulus undershoot was interpreted as a normal decline to the resting state of neural activity [50, 53], and reductions in the second negative peak may reflect alteration of the neural responses in patients with right cerebellar tumors. The pattern of averaged BOLD responses did not illustrate the initial dip and post-stimulus undershoot in patients with left cerebellar tumors, which may have been masked by the initial dip and post-stimulus undershoot such that it could not be recognized by means of the extended standard derivation of BOLD responses. These results indicate fluctuations in the large BOLD signals in patients with left cerebellar tumors, though there was not much of a difference between patients with left and right tumors in the size of the lesion and the compressed portion of cerebellum. Further studies are required to examine the causal mechanism of fluctuation in the BOLD signals of patients with left cerebellar tumors.

These findings suggest that the cells surrounding a metabolic disturbance area may have provided appropriate assistance to the hippocampal circuitry. The assessment of hippocampal memory function indicated that patients with cerebellar tumors showed selective inability in a lure task, which reflects pattern separation inability and disturbance of the generating activity of young granule cells in the DG of the hippocampus. This inability was found in patients with both right and left cerebellar tumors, although performances in the other two tasks (new and same) were equal to those of normal

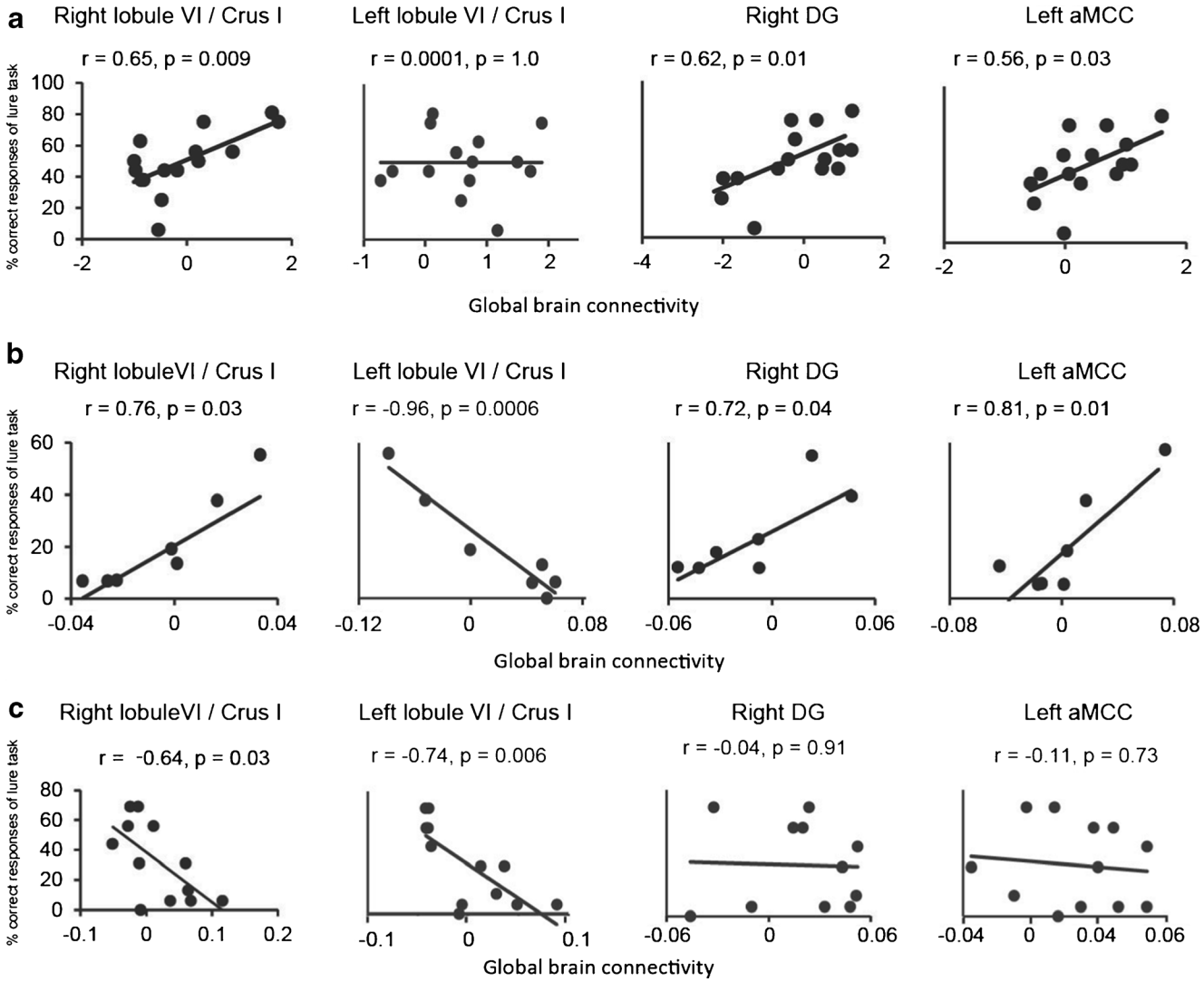

Fig. 8 Correlation of GBC value and pattern separation ability. **a**–**c**. Graphs showing correlation between the correct response rate in the lure task and the GBC value in the right cerebellar lobule VI including Crus I (*lobule VI/Crus I*), left lobule VI/Crus I, right dentate gyrus (DG), and left anterior middle cingulate cortex (*aMCC*). **a** healthy subjects (n=15). **b** patients with left cerebellar tumors (n=7). **c** patients with right cerebellar tumors (n=12). The r value, the correlation coefficient of the Pearson product–moment. The p value, the significance level of correlation coefficient. x-axis, the value of GBC. y-axis, the percentage of correct responses of lure task. Details are described in the text

healthy volunteers. Taken together, these findings indicate that the selective inability in the lure task was caused by cognitive dysfunction and not by motor impairment in patients with cerebellar tumors. Instead, cerebellar damage seems to affect hippocampal DG functions.

Influence on Pattern Separation Function by Global Brain Connectivity of Posterior Lateral Cerebellum

The fMRI examination of cognitive processing observed cerebellar activity in the convergent area of the posterior lateral lobe, which also regulates smooth motor control. Activations of posterior lateral cerebellum were previously proposed as the internal model for new tools [7]. Our present GBC study demonstrated that the value was altered in patients with cerebellar tumors compared with the normal control group. Interestingly, the left and right values of patients with cerebellar tumors converged on a narrow window. It was reported that cerebellum, cingulate cortex, and hippocampus have high GBC values that are included in the top 10 % of GBC [29]. High GBC areas have more connectivity with cortical and subcortical regions [29]. The GBC values that were restricted within the narrow window may represent a reduction in connectivity induced by lesions to the posterior lateral cerebellum.

Our present study also showed that the right cerebellar lobule VI/Curs I, right DG, and left aMCC are important regions for pattern separation. In particular, patients with right cerebellar tumors showed a disruption in the correlation of GBC to these areas associated with pattern separation function. High GBC areas are believed to integrate cortical and

subcortical activity and act as global hubs influencing cognitive control [29, 30]. According to resting-state fMRI analysis, it was reported that the posterior cerebellum has a functional connection with the prefrontal cortex, involving the anterior cingulate cortex for cognitive functions [8, 9]. Reduction in the GBC of patients with right cerebellar tumors not only elicited functional dissociation of the right and left lobule VI/Curs I from pattern separation ability but also affected the anterior mid-cingulate cortex and hippocampus. In light of these observations, global connectivity of the right posterior lateral cerebellum may play an important role in pattern separation as well as cognitive functions.

Interaction between the hippocampus and cerebellum occurs in the spatial domain [54]. Cerebellar impairment leads to dysfunction of the spatial cord as recorded by place cells in the CA1 hippocampus using L7-PKCI mice in which protein kinase C-dependent long-term depression at the parallel fiber-Purkinje cell synapses is blocked. Consequently, the cerebellum assists navigation by participating in the building of the hippocampal spatial map. Hippocampal-cerebellar interactions occur during spatio-temporal prediction [55]. Patients with right cerebellar tumors showed a high rate of error in the lure task, as was indicated by fMRI. Just as the cerebellum contributes to the fine tuning of coordination in skilled motor sequences in motor control, it also contributes to cognition by facilitating the precise discrimination of overlapping or similar experiences among episodic memories. Newly generated young neurons have been shown to facilitate pattern separation in the hippocampus [49]. Whether cognitive decline and disability in pattern separation in patients with cerebellar disease only reflect functional changes in new neurons or are instead associated with a decrease in hippocampal neurogenesis is an interesting question that requires further investigation.

Conclusions

The present findings show that compression of the posterior lateral cerebellum causes impairment of cognitive function. Surgical decompression of the cerebellum facilitated cognitive recovery. The fMRI study demonstrated global connectivity between the Crus I, aMCC, and hippocampus during analysis of hippocampal memory function. The posterior lateral cerebellum acts as a global hub, cooperating with the hippocampus and anterior mid-cingulate cortex to facilitate pattern separation ability.

Acknowledgments This work was supported by the Industrial Disease Clinical Research Grants by the Ministry of Health, Labour and Welfare (to S.I., T.W., Y.H., and M.N.), and Special Account Budget for Education and Research (to S.I., and M.T.), Grants-in-Aid for Scientific Research (B) (23390352) (to S.I.), and Challenging Exploratory Research (24650168) (to S.I.) by the Ministry of Education, Culture, Sports, Science and Technology in Japan, and the Princess Takamatsu Cancer Fund (to S.I.), and the Grants for Takeda Science Foundation (to M.T., and S.I.).

Conflict of Interest The authors declare that they have no conflict of interest.

Author Contributions A.S. and M.N. prepared the manuscript; A.S. and D.T. performed neuropsychological analysis; M.N. and S.M. analyzed fMRI data; H.N., T.M., Y.H., and T.W. handled the clinical management; and S.I. designed and administered this study and wrote the manuscript. All authors edited the manuscript.

References

1. Manto M, Bower JM, Conforto AB, Delgado-García JM, da Guarda SN, Gerwig M, et al. Consensus paper: roles of the cerebellum in motor control—the diversity of ideas on cerebellar involvement in movement. Cerebellum. 2012;11:457–87.
2. Grimaldi G, Manto M. Topography of cerebellar deficits in humans. Cerebellum. 2012;11:336–51.
3. Riva D, Annunziata S, Contarino V, Erbetta A, Aquino D, Bulgheroni S. Gray matter reduction in the vermis and CRUS-II is associated with social and interaction deficits in low-functioning children with autistic spectrum disorders: a VBM-DARTEL Study. Cerebellum. 2013;12:676–85.
4. Koziol LF, Budding D, Andreasen N, D'Arrigo S, Bulgheroni S, Imamizu H, et al. Consensus paper: the cerebellum's role in movement and cognition. Cerebellum. 2014;13:151–77.
5. Koziol LF, Budding DE, Chidekel D. From movement to thought: executive function, embodied cognition, and the cerebellum. Cerebellum. 2012;11:505–25.
6. Schmahmann JD, Sherman JC. The cerebellar cognitive affective syndrome. Brain. 1998;121(4):561–79.
7. Imamizu H, Miyauchi S, Tamada T, Sasaki Y, Takino R, Pütz B, et al. Human cerebellar activity reflecting an acquired internal model of a new tool. Nature. 2000;403:192–5.
8. Habas C, Kamdar N, Nguyen D, Prater K, Beckmann CF, Menon V, et al. Distinct cerebellar contributions to intrinsic connectivity networks. J Neurosci. 2009;29:8586–94.
9. Krienen FM, Buckner RL. Segregated fronto-cerebellar circuits revealed by intrinsic functional connectivity. Cereb Cortex. 2009;19:2485–97.
10. Molinari M, Leggio MG, Solida A, Ciorra R, Misciagna S, Silveri MC, et al. Cerebellum and procedural learning: evidence from focal cerebellar lesions. Brain. 1997;120(Pt 10):1753–62.
11. Chen SH, Desmond JE. Cerebrocerebellar networks during articulatory rehearsal and verbal working memory tasks. Neuroimage. 2005;24:332–8.
12. Marvel CL, Desmond JE. Functional topography of the cerebellum in verbal working memory. Neuropsychol Rev. 2010;20:271–9.
13. Ravizza SM, McCormick CA, Schlerf JE, Justus T, Ivry RB, Fiez JA. Cerebellar damage produces selective deficits in verbal working memory. Brain. 2006;129:306–20.

14. Bakker A, Kirwan CB, Miller M, Stark CE. Pattern separation in the human hippocampal CA3 and dentate gyrus. Science. 2008;319:1640–2.
15. Schmahmann JD, Gardner R, MacMore J, Vangel MG. Development of a brief ataxia rating scale (BARS) based on a modified form of the ICARS. Mov Disord. 2009;24:1820–8.
16. Folstein MF, Folstein SE, McHugh PR. "Mini-mental state". A practical method for grading the cognitive state of patients for the clinician. J Psychiatr Res. 1975;12:189–98.
17. Teng EL, Chui HC. The Modified Mini-Mental State (3MS) examination. J Clin Psychiatry. 1987;48:314–8.
18. Lezak MD, Howieson DB, Loring DW. Orientation and attention. In: Neuropsychological assessment 4th ed. New York: Oxford University Press; 2004 pp. 365–8, 371–4.
19. Wechsler D. Manual for the Wechsler adult intelligence scale—revised. New York: Psychological Corporation; 1981.
20. Maeshima S, Osawa A, Maeshima E, Shimamoto Y, Sekiguchi E, Kakishita K, et al. Usefulness of a cube-copying test in outpatients with dementia. Brain Inj. 2004;18:889–98.
21. Burock MA, Buckner RL, Woldorff MG, Rosen BR, Dale AM. Randomized event-related experimental designs allow for extremely rapid presentation rates using functional MRI. Neuroreport. 1998;9:3735–9.
22. Yassa MA, Stark SM, Bakker A, Albert MS, Gallagher M, Stark CE. High-resolution structural and functional MRI of hippocampal CA3 and dentate gyrus in patients with amnestic mild cognitive impairment. Neuroimage. 2010;51:1242–52.
23. Friston KJ, Holmes AP, Poline JB, Grasby PJ, Williams SC, Frackowiak RS, et al. Analysis of fMRI time-series revisited. Neuroimage. 1995;2:45–53.
24. Tzourio-Mazoyer N, Landeau B, Papathanassiou D, Crivello F, Etard O, Delcroix N, et al. Automated anatomical labeling of activations in SPM using a macroscopic anatomical parcellation of the MNI MRI single-subject brain. Neuroimage. 2002;15:273–89.
25. Schmahmann JD, Doyon J, McDonald D, Holmes C, Lavoie K, Hurwitz AS, et al. Three-dimensional MRI atlas of the human cerebellum in proportional stereotaxic space. Neuroimage. 1999;10:233–60.
26. Duvernoy HM. The human hippocampus: functional anatomy, vascularization and serial sections with MRI. Berlin: Springer Verlag; 2005.
27. Vogt BA, editor. Cingulate neurobiology and disease. NY: Oxford University Press; 2009.
28. Matthew Brett, Jean-Luc Anton, Romain Valabregue, Jean-Baptiste Poline. Region of interest analysis using an SPM toolbox [abstract] Presented at the 8th International Conference on Functional Mapping of the Human Brain, June 2–6, 2002, Sendai, Japan. Available on CD-ROM in NeuroImage, Vol 16, No 2.
29. Cole MW, Pathak S, Schneider W. Identifying the brain's most globally connected regions. Neuroimage. 2010;49:3132–48.
30. Cole MW, Yarkoni T, Repovs G, Anticevic A, Braver TS. Global connectivity of prefrontal cortex predicts cognitive control and intelligence. J Neurosci. 2012;32:8988–99.
31. Fisher RA. Frequency distribution of the values of the correlation coefficient in samples from an indefinitely large population. Biometrika. 1915;10:507–21.
32. Mukaka MM. Statistics corner: a guide to appropriate use of correlation coefficient in medical research. Malawi Med J. 2012;24:69–71.
33. Honey CJ et al. Predicting human resting-state functional connectivity from structural connectivity. Proc Natl Acad Sci U S A. 2009;106:2035–40.
34. Smith SM et al. Correspondence of the brain's functional architecture during activation and rest. Proc Natl Acad Sci U S A. 2009;106:13040–5.
35. Riva D, Giorgi C. The cerebellum contributes to higher functions during development: evidence from a series of children surgically treated for posterior fossa tumours. Brain. 2000;123:1051–61.
36. Baillieux H, De Smet HJ, Dobbeleir A, Paquier PF, De Deyn PP, Mariën P. Cognitive and affective disturbances following focal cerebellar damage in adults: a neuropsychological and SPECT study. Cortex. 2010;46:869–79.
37. Gottwald B, Mihajlovic Z, Wilde B, Mehdorn HM. Does the cerebellum contribute to specific aspects of attention? Neuropsychologia. 2003;41:1452–60.
38. Gottwald B, Wilde B, Mihajlovic Z, Mehdorn HM. Evidence for distinct cognitive deficits after focal cerebellar lesions. J Neurol Neurosurg Psychiatry. 2004;75:1524–31.
39. Hokkanen LS, Kauranen V, Roine RO, Salonen O, Kotila M. Subtle cognitive deficits after cerebellar infarcts. Eur J Neurol. 2006;13:161–70.
40. Stoodley CJ, Schmahmann JD. Functional topography in the human cerebellum: a meta-analysis of neuroimaging studies. Neuroimage. 2009;44:489–501.
41. Stoodley CJ, Valera EM, Schmahmann JD. Functional topography of the cerebellum for motor and cognitive tasks: an fMRI study. Neuroimage. 2012;59:1560–70.
42. Wang D, Buckner RL, Liu H. Cerebellar asymmetry and its relation to cerebral asymmetry estimated by intrinsic functional connectivity. J Neurophysiol. 2013;109:46–57.
43. Wang D, Buckner RL, Liu H. Functional specialization in the human brain estimated by intrinsic hemispheric interaction. J Neurosci. 2014;34:12341–52.
44. Kirschen MP et al. Verbal memory impairments in children after cerebellar tumor resection. Behav Neurol. 2008;20:39–53.
45. Usui N et al. Cortical areas related to performance of WAIS Digit Symbol Test: a functional imaging study. Neurosci Lett. 2009;463:1–5.
46. Habas C. Functional imaging of the deep cerebellar nuclei: a review. Cerebellum. 2010;9:22–8.
47. Neau JP, Arroyo-Anllo E, Bonnaud V, Ingrand P, Gil R. Neuropsychological disturbances in cerebellar infarcts. Acta Neurol Scand. 2000;102:363–70.
48. O'Halloran CJ, Kinsella GJ, Storey E. The cerebellum and neuropsychological functioning: a critical review. J Clin Exp Neuropsychol. 2012;34:35–56.
49. Nakashiba T, Cushman JD, Pelkey KA, Renaudineau S, Buhl DL, McHugh TJ, et al. Young dentate granule cells mediate pattern separation, whereas old granule cells facilitate pattern completion. Cell. 2012;149:188–201.
50. Logothetis NK, Pauls J, Augath M, Trinath T, Oeltermann A. Neurophysiological investigation of the basis of the fMRI signal. Nature. 2001;412:150–7.
51. Schridde U, Khubchandani M, Motelow JE, Sanganahalli BG, Hyder F, Blumenfeld H. Negative BOLD with large increases in neuronal activity. Cereb Cortex. 2008;18:1814–27.
52. Hu X, Yacoub E. The story of the initial dip in fMRI. Neuroimage. 2012;62:1103–8.
53. Shmuel A, Augath M, Oeltermann A, Logothetis NK. Negative functional MRI response correlates with decreases in neuronal activity in monkey visual area V1. Nat Neurosci. 2006;9:569–77.
54. Rochefort C, Arabo A, André M, Poucet B, Save E, Rondi-Reig L. Cerebellum shapes hippocampal spatial code. Science. 2011;334:385–9.
55. Onuki Y, Van Someren EJ, De Zeeuw CI, Van der Werf YD. Hippocampal-cerebellar interaction during spatio-temporal prediction. Cereb Cortex. 2015;25(2):313–21.

Journal of Clinical Neuroscience 23 (2016) 73–75

Contents lists available at ScienceDirect

Journal of Clinical Neuroscience

journal homepage: www.elsevier.com/locate/jocn

Clinical Study

SLC44A1–PRKCA fusion in papillary and rosette-forming glioneuronal tumors

Masaya Nagaishi [a,b,*], Sumihito Nobusawa [b], Nozomi Matsumura [b], Fumihiko Kono [c], Shogo Ishiuchi [d], Tatsuya Abe [e], Michimasa Ebato [f], Yin Wang [g], Akio Hyodo [a], Hideaki Yokoo [b], Yoichi Nakazato [b]

[a] *Department of Neurosurgery, Dokkyo Medical University Koshigaya Hospital, 2-1-50 Minami-Koshigaya, Koshigaya-shi, Saitama 343-8555, Japan*
[b] *Department of Human Pathology, Gunma University Graduate School of Medicine, Maebashi-shi, Gunma, Japan*
[c] *Department of Diagnostic Pathology, Kyoto University Hospital, Mibu, Nakagyo-ku, Kyoto, Japan*
[d] *Department of Neurosurgery, University of the Ryukyus Graduate School of Medicine, Nishihara-cho, Okinawa, Japan*
[e] *Department of Neurosurgery, Oita University School of Medicine, Hasama-machi, Yufu-shi, Oita, Japan*
[f] *Department of Neurosurgery, Koshigaya Municipal Hospital, Koshigaya-shi, Saitama, Japan*
[g] *Department of Neuropathology, Institute of Neurology and Huashan Hospital of Fudan University, Shanghai, China*

ARTICLE INFO

Article history:
Received 3 January 2015
Accepted 11 April 2015

Keywords:
Fluorescence *in situ* hybridization
Papillary glioneuronal tumor
Rosette-forming glioneuronal tumor
SLC44A–PRKCA fusion

ABSTRACT

We investigated the fused protein of solute carrier family 44 choline transporter member 1 (*SLC44A1*) and protein kinase C alpha (*PRKCA*) in three patients with papillary glioneuronal tumors (PGNT). PGNT and rosette-forming glioneuronal tumors (RGNT) are recently identified, unusual glioneuronal tumor variants which were categorized as novel tumor entities in the 2007 World Health Organization classification system. The molecular background of these tumors remains poorly understood due to the paucity of studies. The *SLC44A1–PRKCA* fusion was recently detected in three cases of PGNT. We invesitgated for the *SLC44A1–PRKCA* fusion protein in the three PGNT patients and a further two with RGNT using fluorescence *in situ* hybridization. Two out of the three PGNT patients had a fused signal (paired red–green signal) representing a rearrangement on chromosomes 9 and 17. A normal signal pattern was observed in the third PGNT patient. Neither of the two RGNT patients demonstrated a fused signal. This suggests that the *SLC44A1–PRKCA* fusion is a characteristic alteration in PGNT but not RGNT. Therefore, it is a potential biomarker of PGNT. The paired red–green signal that was observed in the PGNT patients implies the presence of a different breakpoint than that previously reported in the 9q31 and 17q24 genes.

1. Introduction

Glioneuronal tumors of the central nervous system are rare low grade tumors that consist of glial and neuronal cells at varying stages of differentiation. Papillary glioneuronal tumors (PGNT) and rosette-forming glioneuronal tumors (RGNT) have been recently identified as unusual glioneuronal tumor variants, and were categorized as novel tumor entities in the 2007 World Health Organization (WHO) classification system [1]. PGNT are characterized by a prominent pseudopapillary structure composed of small glial cells arranged around hyalinized blood vessels along with sheets or focal collections of synaptophysin-positive neurocytes. Oligodendroglia-like cells (OLC) expressing oligodendrocyte transcription factor (Olig2) are also sometimes present in parts of this tumor [2,3]. RGNT display uniform neurocytes that form neurocytic rosettes and/or perivascular pseudorosettes. The glial tumor component in RGNT resembles pilocytic astrocytoma. OLC have also been detected in inter-rosette spaces. Therefore, the histopathology of RGNT shares common features with PGNT.

In spite of the morphological features of the glial elements, none of the reported PGNT and RGNT patients have had a 1p19q codeletion, *KIAA–BRAF* fusion, or *BRAF* V600E mutation [4–7]. The molecular features and histogenesis of these glioneuronal tumors have not yet been elucidated in detail. Bridge et al. recently described a solute carrier family 44 choline transporter member 1 (*SLC44A1*)–protein kinase C alpha (*PRKCA*) fusion as the defining genetic alteration in PGNT. They observed it in all three of their PGNT patients, and investigated it with fluorescence *in situ* hybridization (FISH) [8]. Although they suggested that this genetic alteration was the defining molecular feature and may be responsible for the pathogenesis of PGNT, the analysis of a larger number

* Corresponding author. Tel.: +81 48 965 1111; fax: +81 48 965 8682.
E-mail address: nagaishi-nsu@umin.ac.jp (M. Nagaishi).

http://dx.doi.org/10.1016/j.jocn.2015.04.021
0967-5868/

of PGNT patients is needed. In RGNT, the phosphatidylinositol-4,5-bisphosphate 3-kinase catalytic subunit alpha and fibroblast growth factor receptor 1 mutations that are predominantly seen in glial tumors have recently been demonstrated [7,9]. However, the *SLC44A1–PRKCA* fusion has not been analyzed in this tumor type. Therefore, the aim of the present study was to confirm the FISH findings from the previously reported PGNT patients, and to investigate this fusion in another type of glioneuronal tumor, RGNT.

2. Materials and methods

2.1. Tumor samples

Formalin fixed paraffin embedded (FFPE) tissue samples from three PGNT and two RGNT patients were obtained from the following institutions: Department of Neurosurgery, Ryukyu University, Japan; Department of Pathology, Kyoto City Hospital, Japan; Department of Neurosurgery, Oita University Hospital, Japan; Department of Neurosurgery, Koshigaya Municipal Hospital; Department of Neuropathology, Huashan Hospital, China. All of the samples were from primarily developed intracranial tumors and were diagnosed on the basis of the 2007 WHO Classification [1]. All clinical samples were analyzed according to a protocol approved by the Medical Ethics Committee of Gunma University (based on the principles detailed in the Declaration of Helsinki). All patient information associated with this study was obtained in a deidentified format.

2.2. FISH

A dual color interphase FISH analysis was performed on 5 micron thick FFPE tissue sections, using previously published probes and methods [8,10]. Briefly, following deparaffinization and pretreatment, the sections were incubated in 0.35% pepsin/0.01 normal hydrochloric acid for 30 min, and then in 0.1% nonionic polyoxyethylene surfactant 40/2 × standard sodium citrate for 30 min. DNA was denatured using 70% formamide/2 × standard sodium citrate for 5 min at 75°C. An 8 μl aliquot mixture of two labeled probes was applied to the glass slide with a cover slip. The latter probe was prepared from bacterial artificial chromosomes (RP11-1036I14 for *PRKCA*, RP11-95O7 for *SLC44A1*; GenoTechs, Tsukuba, Japan) using a DNA purification kit (Qiagen Plasmid Kit Midi; Qiagen, Germantown, MD, USA) and labeled using Spectrum Green or Spectrum Orange (Vysis Nick Translation Kit; Abbott Laboratories, Abbott Park, IL, USA). The samples were intermittently irradiated at intervals of 3 s on and 2 s off (42°C; 300 W) for 2 h using a microwave processor, and then incubated for 3 nights. 4,6-diamidino-2-phenylindole (DAPI I; 1,000 ng/ml; Vysis; Abbott Laboratories) was used for nuclear counterstaining. The signals were evaluated in more than 200 non-overlapping intact nuclei of the tumor cells. A previous study detected a dual fusion signal in >68% of tumor cells in all the PGNT samples [8]. Based on this finding, we intentionally defined >60% of the neoplastic cells per tissue section as positive for a dual fusion signal.

3. Results

The microscopic examination revealed a distinctive pseudopapillary morphology with hyalinized vessels and glial cells characterized by round nuclei and scant cytoplasm in all three PGNT samples. The neuronal cells were scattered in the interpapillary area and were strongly immunostained by synaptophysin. Differently sized neuronal cells, including ganglion and ganglioid cells, were occasionally noted in each sample. Olig2-positive cells were observed around the pseudopapillary structure (Fig. 1A–D). Both RGNT samples displayed typical neurocytic rosettes with central fibrillary stroma that were immunoreactive to synaptophysin.

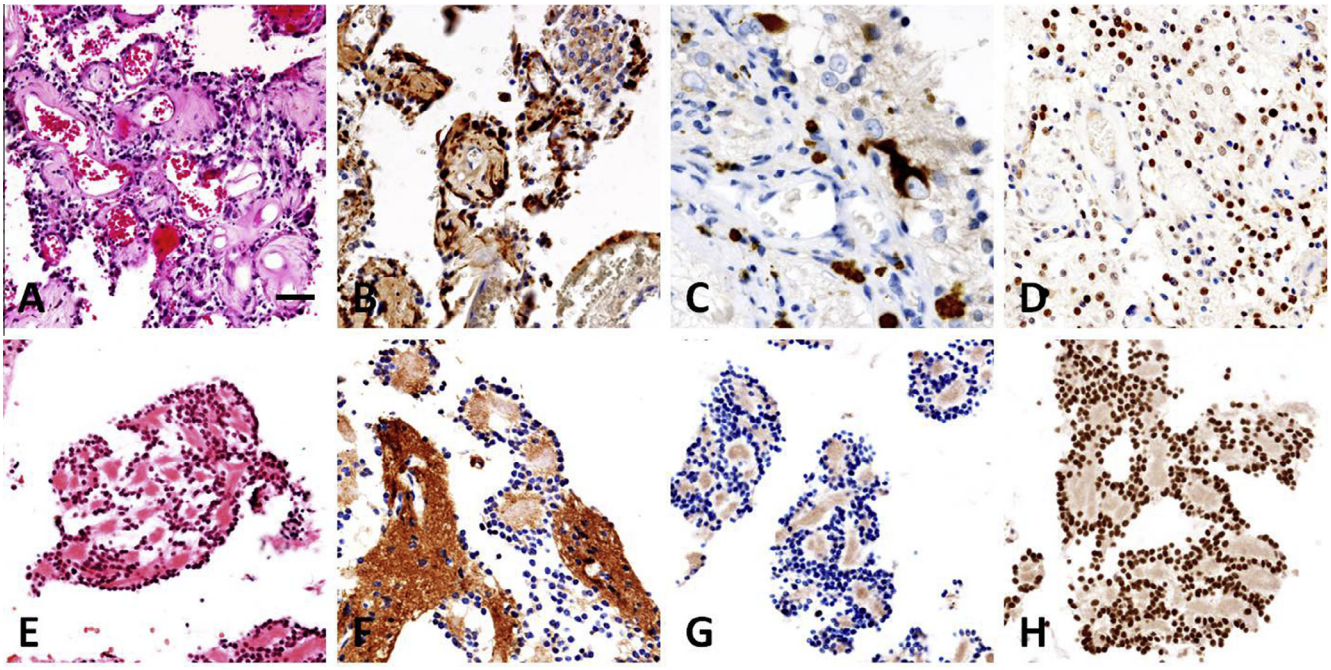

Fig. 1. Representative morphological and immunohistochemical features from tumor sections of papillary glioneuronal tumors (PGNT; A–D) and rosette-forming glioneuronal tumors (RGNT; E–H). PGNT showing a pseudopapillary structure (A; hematoxylin and eosin [H&E] staining) circumscribed by glial fibrillary acidic protein (GFAP)-positive astrocytic cells (B) and scattered neuronal cells, highlighted by synaptophysin immunostaining (C). Oligodendrocyte transcription factor (Olig2)-positive cells were present among blood vessels (D). RGNT consisted of astrocytic tumor cells (E; H&E staining) expressing GFAP (F) and neurocytes forming rosettes with a synaptophysin-positive neuropil core (G). Rosette-forming cells expressed Olig2 (H). The scale bar in part A represents the following scales for each image: 100 μm (A); 25 μm (C); 50 μm (B, D–H).

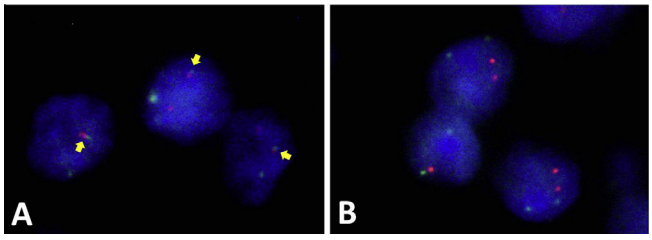

Fig. 2. Fluorescence *in situ* hybridization (FISH) images of papillary glioneuronal tumors (PGNT) and rosette-forming glioneuronal tumors (RGNT). A FISH analysis for protein kinase C alpha (*PRKCA*; green) and solute carrier family 44 choline transporter member 1 (*SLC44A1*; red) probes showed a fused signal pattern (paired red–green signal) in PGNT (A; arrow) and a normal, unfused signal pattern in RGNT (B).

The neurocytic tumor cells had small round nuclei that were stained by Olig2, and scant cytoplasm. The glial component of RGNT was dominated by spindle astroglial cells resembling pilocytic astrocytomas (Fig. 1E–H). All the PGNT and RGNT samples had Rosenthal fibers and eosinophilic granular bodies, and both lacked necrosis and mitotic activity in the tumor cells.

With the dual color probe, the normal cell nuclei showed separate red and green signals (two of each). Two out of three PGNT samples showed one fused signal (paired red–green) representing the rearrangement of chromosomes 9 and 17. However, neither displayed a completely fused yellow signal (Fig. 2A). A normal signal pattern was observed in the third PGNT sample. On the other hand, neither of the two RGNT samples demonstrated a fused signal (Fig. 2B).

4. Discussion

A novel translocation between chromosomes 9 and 17 was recently described in three PGNT patients [8]. FISH data revealed two juxtaposed red–green signals, indicating breakpoints in the 9q31 and 17q24 genes, and a sequence analysis of the reverse transcription polymerase chain reaction-generated transcript identified the fusion point in *SLC44A1* exon 15 and *PRKCA* exon 9. *PRKCA* is a member of a family of serine and threonine-specific protein kinases that contain the *BRAF* gene, which is involved in tumor-promoting signaling pathways [11]. *SLC44A1* has a role in sodium-independent choline transport and is widely expressed throughout the nervous system in both neurons and oligodendrocytes [12]. The deregulation of *PRKCA* and/or high activity of the *SLC44A1* promoter were previously proposed to be involved in the tumorigenesis of PGNT [8].

In our study, the fusion of chromosomes 9 and 17 was confirmed in two PGNT tissue samples by FISH, using one of the two probe sets described by Bridge et al. [8]. The FISH analysis with the other probe set did not result in an informative fluorescence signal. One of the PGNT samples did not show the *SLC44A1–PRKCA* fusion. In addition, in our samples, the fusion signals were a paired red–green signal but not an overlapping yellow signal, which may indicate different breakpoints than those that were previously reported within the chromosomal regions 9q31 and 17q24. A sequence analysis previously identified two different breakpoints on the *SLC44A1* gene [8]. Further analysis is needed to identify the localization of the different breakpoints and investigate the PGNT that didn't have this fusion. We were unable to perform this analysis due to the small size of the surgical specimens.

PGNT and RGNT are characterized by a biphasic pattern with neuronal and glial components. The neuronal component is mainly comprised of neurocytes, similar to the central neurocytoma. In both PGNT and RGNT, OLC are a characteristic feature and have recently been suggested to derive from common progenitor cells with the neurocytes [10]. Therefore, the cellular characteristics of the neuronal component in RGNT bear some similarities to those of the neuronal components in PGNT. The *SLC44A1–PRKCA* fusion may be histopathologically associated with papillary formation, which is a characteristic of PGNT but not RGNT.

In summary, PGNT and RGNT have recently been categorized as unusual variants of glioneuronal tumors, with molecular features that remain poorly understood. We verified the existence of the recently identified *SLC44A1–PRKCA* fusion in two out of our three PGNT patients. The fusion was not present in either of the RGNT patients, which adds support to its potential as a biomarker for PGNT.

Conflicts of Interest/Disclosures

The authors declare that they have no financial or other conflicts of interest in relation to this research and its publication.

Acknowledgment

We would like to thank Mr. Koji Isoda and Ms. Machiko Yokota for their technical support.

References

[1] Louis DN, Ohgaki H, Wiestler OD. The 2007 WHO classification of tumours of the central nervous system. Acta Neuropathol 2007;114:97–109.
[2] Vajtai I, Kappeler A, Lukes A, et al. Papillary glioneuronal tumor. Pathol Res Pract 2006;202:107–12.
[3] Izycka-Swieszewska E, Majewska H, Szurowska E, et al. Papillary glioneuronal tumour of the precentral gyrus. Folia Neuropathol 2008;46:158–63.
[4] Faria C, Miguens J, Antunes JL, et al. Genetic alterations in a papillary glioneuronal tumor. J Neurosurg Pediatr 2008;1:99–102.
[5] Gessi M, Waha A, Setty P, et al. Analysis of KIAA1549-BRAF fusion status in a case of rosette-forming glioneuronal tumor of the fourth ventricle (RGNT). Neuropathology 2011;31:654–7.
[6] Myung JK, Byeon SJ, Kim B, et al. Papillary glioneuronal tumors: a review of clinicopathologic and molecular genetic studies. Am J Surg Pathol 2011;35:1794–805.
[7] Ellezam B, Theeler BJ, Luthra R, et al. Recurrent PIK3CA mutations in rosette-forming glioneuronal tumor. Acta Neuropathol 2012;123:285–7.
[8] Bridge JA, Liu XQ, Sumegi J, et al. Identification of a novel, recurrent SLC44A1-PRKCA fusion in papillary glioneuronal tumor. Brain Pathol 2013;23:121–8.
[9] Gessi M, Moneim YA, Hammes J, et al. FGFR1 mutations in Rosette-forming glioneuronal tumors of the fourth ventricle. J Neuropathol Exp Neurol 2014;73:580–4.
[10] Tanaka Y, Yokoo H, Komori T, et al. A distinct pattern of Olig2-positive cellular distribution in papillary glioneuronal tumors: a manifestation of the oligodendroglial phenotype? Acta Neuropathol 2005;110:39–47.
[11] Michie AM, Nakagawa R. The link between PKCalpha regulation and cellular transformation. Immunol Lett 2005;96:155–62.
[12] Michel V, Bakovic M. The ubiquitous choline transporter SLC44A1. Cent Nerv Syst Agents Med Chem 2012;12:70–81.

BJP British Journal of Pharmacology

DOI:10.1111/bph.13236
www.brjpharmacol.org

RESEARCH PAPER

A novel insulinotropic mechanism of whole grain-derived γ-oryzanol via the suppression of local dopamine D_2 receptor signalling in mouse islet

Correspondence
Professor Hiroaki Masuzaki, Division of Endocrinology, Diabetes and Metabolism, Hematology, Rheumatology (Second Department of Internal Medicine), Graduate School of Medicine, University of the Ryukyus, 207 Uehara, Nishihara, Nakagami-gun, Okinawa 903-0215, Japan. E-mail: hiroaki@med.u-ryukyu.ac.jp

Received
4 March 2015
Revised
16 June 2015
Accepted
20 June 2015

Chisayo Kozuka[1], Sumito Sunagawa[1], Rei Ueda[1], Moritake Higa[1,2], Yuzuru Ohshiro[1,3], Hideaki Tanaka[1,4], Chigusa Shimizu-Okabe[5], Chitoshi Takayama[5], Masayuki Matsushita[6], Masato Tsutsui[7], Shogo Ishiuchi[8], Masanori Nakata[9], Toshihiko Yada[9], Jun-ichi Miyazaki[10], Seiichi Oyadomari[11], Michio Shimabukuro[12] and Hiroaki Masuzaki[1]

[1]*Division of Endocrinology, Diabetes and Metabolism, Hematology, Rheumatology (Second Department of Internal Medicine), Departments of* [5]*Molecular Anatomy,* [6]*Molecular and Cellular Physiology,* [7]*Pharmacology,* [8]*Neurosurgery, Graduate School of Medicine, University of the Ryukyus, Okinawa, Japan,* [2]*The Diabetes and Life-Style Related Disease Center, Tomishiro Central Hospital, Okinawa, Japan,* [3]*Okinawa Daiichi Hospital, Okinawa, Japan,* [4]*Tanaka Clinic, Okinawa, Japan,* [9]*Division of Integrative Physiology, Department of Physiology, Jichi Medical University School of Medicine, Tochigi, Japan,* [10]*Division of Stem Cell Regulation Research, Osaka University Graduate School of Medicine, Osaka, Japan,* [11]*Institute for Genome Research, University of Tokushima, Tokushima, Japan, and* [12]*Department of Cardio-Diabetes Medicine, Institute of Biomedical Sciences, Tokushima University Graduate School, Tokushima, Japan*

BACKGROUND AND PURPOSE

γ-Oryzanol, derived from unrefined rice, attenuated the preference for dietary fat in mice, by decreasing hypothalamic endoplasmic reticulum stress. However, no peripheral mechanisms, whereby γ-oryzanol could ameliorate glucose dyshomeostasis were explored. Dopamine D_2 receptor signalling locally attenuates insulin secretion in pancreatic islets, presumably via decreased levels of intracellular cAMP. We therefore hypothesized that γ-oryzanol would improve high-fat diet (HFD)-induced dysfunction of islets through the suppression of local D_2 receptor signalling.

EXPERIMENTAL APPROACH

Glucose metabolism and regulation of molecules involved in D_2 receptor signalling in pancreatic islets were investigated in male C57BL/6J mice, fed HFD and treated with γ-oryzanol . In isolated murine islets and the beta cell line, MIN6 , the effects of γ-oryzanol on glucose-stimulated insulin secretion (GSIS) was analysed using siRNA for D_2 receptors and a variety of compounds which alter D_2 receptor signalling.

KEY RESULTS

In islets, γ-oryzanol enhanced GSIS via the activation of the cAMP/PKA pathway. Expression of molecules involved in D_2 receptor signalling was increased in islets from HFD-fed mice, which were reciprocally decreased by γ-oryzanol. Experiments with siRNA for D_2 receptors and D_2 receptor ligands *in vitro* suggest that γ-oryzanol suppressed D_2 receptor signalling and augmented GSIS.

CONCLUSIONS AND IMPLICATIONS

γ-Oryzanol exhibited unique anti-diabetic properties. The unexpected effects of γ-oryzanol on D_2 receptor signalling in islets may provide a novel; natural food-based, approach to anti-diabetic therapy.

Abbreviations

$[Ca^{2+}]_i$, cytosolic Ca^{2+} concentration; CCK-8, cholecystokinin-octapeptide; DAT, dopamine transporter; GLP-1, glucagon-like peptide 1; GSIS, glucose-stimulated insulin secretion; GTT, glucose tolerance test; HFD, high-fat diet; IHC, immunohistochemical; siRNA, small interfering RNA; TH, L-tyrosine hydroxylase; VMAT2, vesicular monoamine transporter 2

Tables of Links

TARGETS
GPCRs[a]
Dopamine D_2 receptor
GPR119
GPR120
Transporters[b]
DAT, dopamine transporter
VMAT2, vesicular monoamine transporter 2
Enzymes[c]
PKA
TH, tyrosine hydroxylase

LIGANDS	
cAMP	Haloperidol
CCK-8, cholecystokinin-octapeptide	Insulin
L-DOPA	Oleoylethanolamide
GLP-1, glucagon-like peptide 1	Palmitic acid
Glucagon	Quinpirole
GW 9508	Somatostatin
H-89	

These Tables list key protein targets and ligands in this article which are hyperlinked to corresponding entries in http://www.guidetopharmacology.org, the common portal for data from the IUPHAR/BPS Guide to PHARMACOLOGY (Pawson *et al.*, 2014) and are permanently archived in the Concise Guide to PHARMACOLOGY 2013/14 ([a,b,c]Alexander *et al.*, 2013a,b,c).

Introduction

Dopamine is a major catecholamine neurotransmitter that controls a wide range of biological processes important in neurological, cardiovascular and metabolic homeostasis. Previous reports have demonstrated that in patients with Parkinson's disease, glucose metabolism was markedly impaired by treatment with L-DOPA, a dopamine precursor, in a dose-dependent manner (Sirtori *et al.*, 1972; Marsden and Parkes, 1977). Importantly, molecules involved in dopamine receptor signalling are expressed in both murine and human pancreatic islets (Rubi *et al.*, 2005; Simpson *et al.*, 2012). Notably, a recent study on isolated pancreatic islets from humans demonstrated that pancreatic islet-derived dopamine did attenuate insulin secretion in an autocrine or paracrine fashion via its receptors (Simpson *et al.*, 2012). In particular, studies in dopamine D_2 receptor knockout mice suggest a critical role of dopaminergic suppression in function and replication of pancreatic beta cells during development in mice (Garcia-Tornadu *et al.*, 2010).

It is well recognized that two distinct signalling pathways contribute to the control of insulin secretion from pancreatic beta cells, namely the ATP-sensitive K^+ channel-dependent pathway (triggering pathway) and the cAMP/PKA pathway (amplifying pathway) (Henquin, 2000; Kahn *et al.*, 2006). Two major incretin hormones, glucagon-like peptide 1 (GLP-1) and glucose-dependent insulinotropic polypeptide, are crucial regulators for glucose-stimulated insulin secretion (GSIS) through an increase in intracellular cAMP level, thereby activating the cAMP/PKA pathway. On the other hand, dopamine is known to substantially decrease intracellular cAMP level mainly via D_2 receptors in striatum and pituitary gland in the brain in rats, pigs and humans (Missale *et al.*, 1998; Vallone *et al.*, 2000).

Based on the notion that chronic feeding with a high fat diet (HFD) causes dysfunction of pancreatic islets and results in whole body glucose dysmetabolism (Giacca *et al.*, 2011), we hypothesized that dopamine receptor signalling would be activated locally in pancreatic islets from HFD-fed mice, thereby causing dyshomeostasis of islet functions, at least partly, through a decrease in intracellular cAMP level. On the other hand, it has been shown that expression of genes involved in D_2 receptor signalling in the brain reward system (e.g. striatum, ventral tegmental area) was considerably

decreased in HFD-induced obese rodents, resulting in profound addiction to fatty foods (Li *et al.*, 2009; Johnson and Kenny, 2010). This finding suggested that decreased local synthesis of dopamine in the brain could be relevant to this deviation in feeding behaviour.

γ-Oryzanol, derived from unrefined rice, is a unique bioactive substance, consisiting of a mixture of ferulic acid esters with phytosterols or triterpene alcohols (Lerma-Garcia *et al.*, 2009; Kozuka *et al.*, 2013). An earlier study in humans demonstrated that replacement of white rice by brown rice reduced the incidence of type 2 diabetes mellitus (Sun *et al.*, 2010). Based on this report and our interventional trial assessing the metabolically beneficial impact of brown rice on pre-diabetic obese humans (Sun *et al.*, 2010; Shimabukuro *et al.*, 2014), we recently reported in mouse experiments that γ-oryzanol acted directly on the hypothalamus and attenuated preference for dietary fat by decreasing hypothalamic endoplasmic reticulum (ER) stress, thereby ameliorating HFD-induced obesity (Kozuka *et al.*, 2012). We also demonstrated that long-term administration of γ-oryzanol considerably ameliorated HFD-induced glucose dyshomeostasis, independently of body weight and food intake (Kozuka *et al.*, 2012). Moreover, although γ-oryzanol (3.2 $mg \cdot g^{-1}$ body weight) given orally to mice was distributed predominantly to the brain (83.8 mg per 100 g tissue); it also accumulated particularly in the pancreas (3.5 mg per 100 g tissue) 1 h after supplementation (Kozuka *et al.*, 2015). However, the full mechanism whereby γ-oryzanol ameliorates glucose dysmetabolism throughout the body remained to be elucidated.

In rats, γ-oryzanol increased the dopamine content of the medial basal hypothalamus (Ieiri *et al.*, 1982). This effect was suppressed by an inhibitor of L-tyrosine hydroxylase (TH), the rate-limiting enzyme in dopamine synthesis (Ieiri *et al.*, 1982), suggesting a potential interaction of γ-oryzanol between dopamine metabolism and signalling via dopamine receptors. Based on all these findings, we tested if γ-oryzanol would improve dysfunction of pancreatic islets through the inhibition of D_2 receptor signalling in murine experimental models.

Methods

Animals

All animal care and experimental procedures were approved by the Animal Experiment Ethics Committee of the University of the Ryukyus (Nos. 5352, 5718 and 5943). All studies involving animals are reported in accordance with the ARRIVE guidelines for reporting experiments involving animals (Kilkenny *et al.*, 2010; McGrath *et al.*, 2010). A total of 204 animals were used in the experiments described here.

Eight-week-old male C57BL/6J mice obtained from Charles River Laboratories Japan, Inc. (Kanagawa, Japan) were housed at 24°C under a 12 h/12 h light/dark cycle. The mice were allowed free access to food and water.

Administration of γ-oryzanol

γ-Oryzanol (Wako Pure Chemical Industries, Ltd., Osaka, Japan) was dissolved in 0.5% methyl cellulose solution. γ-Oryzanol (20, 80 or 320 $\mu g \cdot g^{-1}$ body weight) was delivered into the stomach by a gavage needle every day during feeding with a HFD (Western Diet; Research Diets Inc., New Brunswick, NJ, USA) for 13 weeks. HFD and HFD containing 0.4% γ-oryzanol were manufactured as pellets by Research Diets (Research Diets Inc.). Daily intake of γ-oryzanol by mice, as estimated by mean food intake, was approximately 320 $\mu g \cdot g^{-1}$ body weight. The doses of γ-oryzanol were determined as described (Kozuka *et al.*, 2012).

Metabolic parameters

Whole blood was taken from the tail vein and blood glucose was measured using an automatic glucometer (Medisafe Mini; Terumo, Tokyo, Japan). Occasional blood samples were taken from the retro-orbital venous plexuses or tail vein. Plasma insulin, glucagon and active GLP-1 levels were measured using ELISA kits (Shibayagi Co. Ltd., Gunma, Japan; Wako Pure Chemical Industries, Ltd.; and Morinaga Institute of Biological Science, Inc., Tokyo, Japan). For glucose tolerance tests (GTTs), mice were intraperitoneally injected with 2.0 $g \cdot kg^{-1}$ glucose after an 18 h fast. Blood glucose levels were measured at the indicated times.

Sub-diaphragmatic vagotomy

Sub-diaphragmatic vagotomy, or sham surgery, was performed as described earlier (Miyamoto *et al.*, 2012) and mice were used for experiments 2 weeks after the surgery. To test the success of the vagotomy, we assessed the satiety induced by CCK-8 (Bachem, Bubendorf, Switzerland), which is mediated by the abdominal vagus nerves (Smith *et al.*, 1981; 1985). Sham-treated and vagotomized mice were injected i.p. with PBS or 8 $\mu g \cdot kg^{-1}$ CCK-8 after an 18 h fast.

Immunohistochemical (IHC) analyses

The pancreas was carefully dissected and fixed in 4% paraformaldehyde, embedded in paraffin and sectioned. The paraffin-embedded sections were stained with haematoxylin and eosin or immunostained for insulin (A0654; Dako Japan, Tokyo, Japan), glucagon (A0565; Dako Japan), somatostatin (AB5495; Merck Millipore, Billerica, MA), dopamine transporter (DAT) (AB1591P; Merck Millipore) and TH (AB152; Merck Millipore). The mean size and ratio of glucagon-positive α-cells, DAT-positive and TH-positive cell areas to the total islet area were calculated based on >100 islets per group using Photoshop (Adobe, San Jose, CA, USA).

Isolation of pancreatic islets and assessment of insulin/glucagon secretion

Pancreatic islets were isolated from mice by collagenase digestion (Liberase TL; Roche Diagnostics GmbH, Mannheim, Germany) and purified on a Histopaque gradient (Histopaque 1077; Sigma-Aldrich, St Louis, MO, USA) as described by Zmuda *et al.*, (2011). Insulin secretion from isolated islets and from a murine pancreatic beta cell line, MIN6 cells, (Miyazaki *et al.*, 1990), was measured as described earlier (Wei *et al.*, 2005). Briefly, the islets were incubated with or without γ-oryzanol (0.2, 2 or 20 $\mu g \cdot mL^{-1}$), forskolin (10 mM), Rp-8-Br-cAMPS (10 μM), H-89 (10 μM), haloperidol (1, 10 μM; Wako Pure Chemical Industries, Ltd.), a D_2 receptor antagonist, 10 μM L-DOPA, a dopamine precursor, or 5 μM quinpirole, a potent D_2 receptor agonist (Sigma-Aldrich), for 1 h, and

stimulated with glucose for an additional 1 h with or without γ-oryzanol, haloperidol, L-DOPA or quinpirole. The doses of each compound were decided as described (Simpson *et al.*, 2012). MIN6 cells and an α-cell line (α-TC cells) were seeded at a density of 2.0×10^5 cells·mL^{-1} on 24-well plates. After 48 h of culture, MIN6 cells were incubated with Krebs–Ringer bicarbonate buffer (KRB; composition; 119 mM NaCl, 4.74 mM KCl, 2.54 mM $CaCl_2$, 1.19 mM $MgCl_2$, 1.19 mM KH_2PO_4, 25 mM $NaHCO_3$, 0.5 % BSA, 25 mM HEPES, pH 7.4.) containing 2.5 mM glucose for 2 h, subsequently incubated in KRB with or without γ-oryzanol (0.2, 2 or 10 μg·mL^{-1}) for 1 h. The cells were also incubated with a series of insulin secretagogues with or without γ-oryzanol for 2 h. α-TC cells were incubated with KRB containing 16.7 mM glucose for 1 h, subsequently incubated with or without palmitic acid (0.25 or 0.5 mM; Sigma-Aldrich), γ-oryzanol (2 or 10 μg·mL^{-1}) or haloperidol (10 μM) for 2 h. Insulin or glucagon secretion was normalized by cellular protein content. Levels of cAMP and PKA activity were determined by the cyclic AMP EIA Kit (Cayman Chemical, Ann Arbor, MI, USA) and PKA kinase activity kit (Enzo Life Sciences, Farmingdale, NY, USA) respectively. To measure insulin content of islets, 10 islets were placed in 1 mL of acid-ethanol (90 mM HCl in 70% ethanol). Insulin was extracted overnight at –20°C after sonication, as previously described (Ariyama *et al.*, 2008). The acid-ethanol extract was neutralized with 1 M Tris (pH 7.5) and insulin levels were measured using an ELISA kit.

Measurement of cytosolic Ca^{2+} concentration ($[Ca^{2+}]_i$) in isolated islets

$[Ca^{2+}]_i$ in isolated islets was measured by fura-2 microfluorometry as described (Nakata *et al.*, 2010). Briefly, islets on coverslips were incubated with 1 μM fura-2/acetoxymethylester (Dojin Chemical Co., Kumamoto, Japan) for 1 h at 37°C in KRB containing 2.8 mM glucose with or without γ-oryzanol or haloperidol. Islets were subsequently mounted in a chamber and superfused at a rate of 1 mL·min^{-1} at 37°C in KRB with or without γ-oryzanol or haloperidol. Fluorescence following excitation at 340 nm (F340) and that at 380 nm (F380) was measured, and $[Ca^{2+}]_i$ was expressed by the ratio (F340/F380).

RNA interference

The small interfering RNA (siRNA) for D_2 receptors (the *Drd2* gene) and a control scrambled siRNA were designed and purchased from Sigma-Aldrich. Pancreatic islets and MIN6 cells were transfected with each siRNA using Lipofectamine RNAi/MAX (Life technologies, Tokyo, Japan) according to the manufacturer's protocol. Insulin secretion from MIN6 cells was normalized against cellular DNA content.

Agonist activity assay

Recruitment of β-arrestin to GPCRs, induced by γ-oryzanol was tested by the PathHunter β-Arrestin Assay obtained from DiscoveRx (Fremont, CA, USA). Luminescence was analysed with Envision (PerkinElmer, Waltham, MA, USA) and % activity was expressed as the relative luminescence units of 10 μM γ-oryzanol in comparison with that of each positive ligand. Antagonist activity (% inhibition) was measured against approximately EC_{80} concentrations of agonists. Duplicate data were obtained. The *Z*-factor, a parameter of quality control in high throughput screening assays (Zhang *et al.*, 1999), was determined by the following equation: $Z\text{-factor} = 1 - 3(SD_{sample} + SD_{control})/|mean_{sample} - mean_{control}|$. SD_{sample} and $SD_{control}$ refer to standard deviation of sample and positive control regions respectively.

Western blotting

Western blotting was performed as described (Tanaka *et al.*, 2007) with antibodies against D_2 receptors (AB5084P; Merck Millipore), DAT, TH and β-actin (ab6276; Abcam, Cambridge, MA, USA).

Quantitative real-time PCR

Gene expression was examined as described (Kozuka *et al.*, 2012). Total RNA was extracted using Trizol reagent (Life technologies) and cDNA was synthesized using an iScript™ cDNA Synthesis Kit (Bio-Rad, Hercules, CA, USA). Quantitative real-time PCR was performed using a StepOnePlus™ Real-Time PCR System and Fast SYBR Green Master Mix (Life Technologies). The mRNA levels were normalized against *Rn18s* (18S rRNA). The primer sets used for the quantitative real-time PCR analyses are summarized in Table 1.

Table 1

The primer sets used for quantitative real-time PCR analysis

Gene	GenBank Accession No.	Primer (5′–3′)
Drd2 (D2R)	NM_010077	*f* CCA TTG TCT GGG TCC TGT CC
		r GTG GGT ACA GTT GCC CTT GA
Drd3 (D3R)	NM_007877	*f* GCA GTG GTC ATG CCA GTT CAC TAT CAG
		r CCT GTT GTG TTG AAA CCA AAG AGG AGA GG
Slc6a3 (DAT)	NM_010020	*f* GCA CTA CTT CTT CTC CTC CT
		r CCT GAA GTC TTT ACT CCC TTC C
Th (TH)	NM_009377	*f* CCC TAC CAA GAT CAA ACC TAC C
		r GAG CGC ATG CAG TAG TAA GA
Slc18a2 (VMAT2)	NM_172523	*f* GTC TGT CTA TGG GAG TGT GTA T
		r GGG TAC GGC TGG ACA TTA TT
Rn18s (18S rRNA)	NR_003278	*f* TTC TGG CCA ACG GTC TAG ACA AC
		r CCA GTG GTC TTG GTG TGC TGA

Forward and reverse primers are designated by *f* and *r* respectively. D2R, dopamine D_2 receptor; D3R, dopamine D_3 receptor.

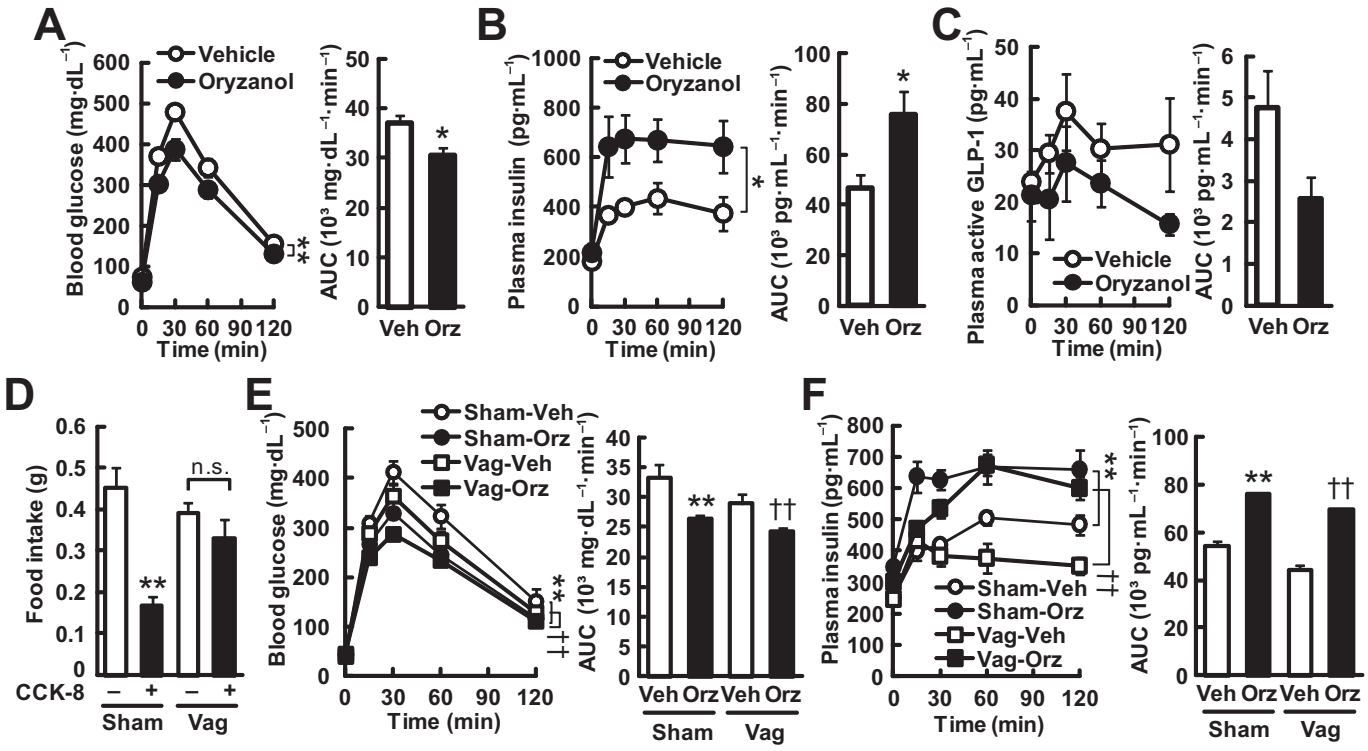

Figure 1

γ-Oryzanol enhances GSIS in mice. (A–C, E, F) Mice on a chow diet were treated with a single oral dose of γ-oryzanol (320 μg·g^{-1}). The concentrations and AUCs of blood glucose (A, E), plasma insulin (B, F) and plasma active GLP-1 (C) during ipGTTs (n = 8) are shown. Chow-fed mice (A–C) and vagotomized mice (Vag) (E, F) were analysed. (D) Satiety effects of CCK-8 were tested in sham-treated mice (Sham) and vagotomized mice (Vag). Sub-diaphragmatic vagotomy abolished the satiety effect of CCK-8. *P < 0.05, **P < 0.01 versus unoperated or sham-operated mice treated with vehicle (Vehicle or Sham-Veh). ††P < 0.01 versus vehicle-treated vagotomized mice (Vag-Veh). Data are expressed as means ± SEM.

Data analysis

Data are expressed as the mean ± SEM from n independent experiments. One-way ANOVA and repeated-measures ANOVA followed by multiple comparison tests (Bonferroni/Dunn method) were used where applicable. Student's t-test was used to analyse the differences between two groups. Differences were considered significant at P < 0.05.

Results

γ-Oryzanol acts directly on pancreatic islets and enhances GSIS in vivo

As a first step in exploring the effects of γ-oryzanol on GSIS in chow-fed mice, the effects of a single oral dose of γ-oryzanol (320 μg·g^{-1} body weight) on blood glucose and insulin levels were examined during i.p. GTTs (ipGTTs). γ-Oryzanol augmented GSIS and significantly enhanced glucose tolerance even in normal mice (Figure 1A,B). γ-Oryzanol showed a trend towards a decrease in the plasma GLP-1 level, but the change was not statistically significant (P = 0.11) (Figure 1C). To see if γ-oryzanol would enhance GSIS independently of GLP-1 receptors, we evaluated, using PathHunter β-arrestin assays, the agonist activities of γ-oryzanol on GLP-1 receptors and on two other GPCRs, GPR119 and GPR120, both of which potently stimulate GLP-1 secretion from intestine (Hirasawa *et al.*, 2005; Chu *et al.*, 2007; Lauffer *et al.*, 2009). γ-Oryzanol did not show agonist activities on these GPCRs [0% of exendin-4, a potent GLP-1 receptor agonist, Z-factor (a parameter of quality control in high throughput screening assays) (Zhang *et al.*, 1999) was 0.81; 9% of oleoylethanolamide, a potent GPR119 agonist, Z-factor was 0.41; –2% of GW 9508, a potent GPR120 agonist, Z-factor was 0.75 respectively].

To exclude the possibility that γ-oryzanol augments GSIS via a central mechanism, we carried out sub-diaphragmatic vagotomy in mice. Cholecystokinin-octapeptide (CCK-8) reduced the food intake in 1 h by 63% in sham-operated mice, while sub-diaphragmatic vagotomy abolished the satiety effect of CCK-8 (Figure 1D), indicating that the vagotomy was successful. In both sham-operated and vagotomized mice, a single oral dose of γ-oryzanol significantly lowered the blood glucose levels and the AUC of glucose during ipGTTs (Figure 1E). Noticeably, in both sham-operated and vagotomized mice, γ-oryzanol markedly increased plasma insulin levels and the AUC of insulin during ipGTTs (Figure 1F). These results suggest that γ-oryzanol acted directly on the pancreatic islets to enhance GSIS.

γ-Oryzanol enhances GSIS through activation of the cAMP/PKA pathway via the suppression of D_2 receptor signalling

In both isolated murine islets and MIN6 cells, γ-oryzanol markedly enhanced GSIS in a dose-dependent fashion (Figure 2A,E). Furthermore, in both cellular systems, γ-oryzanol significantly increased intracellular cAMP levels and PKA activity (Figure 2B,C,F,G). Similarly, augmentation of PKA activity by γ-oryzanol was abolished by H-89, a PKA inhibitor (Figure 2C,G). To explore the underlying mechanism, isolated murine islets and MIN6 cells were exposed to (i) forskolin, which increases intracellular cAMP level; (ii) Rp-8-Br-cAMPS, a cAMP antagonist; or (iii) H-89 respectively. In both cellular systems, γ-oryzanol augmented forskolin-enhanced insulin secretion (Figure 2D,H), while both Rp-8-Br-cAMPS and H-89 abolished such stimulatory effects of γ-oryzanol on GSIS (Figure 2I–K). These findings suggest that γ-oryzanol reinforces GSIS via the cAMP/PKA amplifying pathway in pancreatic islets.

On the other hand, haloperidol, a D_2 receptor antagonist, significantly enhanced GSIS (Figure 3A) through the elevation of intracellular cAMP (Figure 3B) but γ-oryzanol showed no additive effect with haloperidol (Figure 3C,D), supporting the notion that γ-oryzanol increased intracellular cAMP levels and enhanced GSIS through suppression of D_2 receptor signalling. Furthermore, both L-DOPA, a dopamine precursor, and quinpirole, a potent D_2 receptor agonist, abolished γ-oryzanol-induced enhancement of GSIS (Figure 3E–G). Of note, the inhibition by L-DOPA and quinpirole was concentration-dependent (Figure 3F,G). To further confirm the involvement of D_2 receptor signalling in enhancing GSIS by γ-oryzanol, *Drd2* was silenced *in vitro* by incubating the tissues or cells with specific siRNA for 2 days. In both pancreatic islets and MIN6 cells treated with *Drd2* siRNA, the expression of *Drd2* was attenuated by 71.4 ± 0.1% and 69.5 ± 0.1% compared with scrambled siRNA-treated cells respectively (Figure 3H,K). There were no significant changes in the expression of *Drd3* (dopamine D_3 receptor) in both systems (Figure 3H,K). Either γ-oryzanol or haloperidol enhanced GSIS accompanied by the elevation of intracellular cAMP level in cells treated with the scrambled siRNA. In contrast, in *Drd2* siRNA-treated cells, γ-oryzanol and haloperidol did not increase GSIS and intracellular cAMP level (Figure 3I,J,L). These results suggest that γ-oryzanol augments GSIS via the suppression of D_2 receptor signalling in pancreatic beta cells. Of note, data from the PathHunter β-arrestin assays suggested that there was no significant agonist or antagonist activities of γ-oryzanol for any of the dopamine receptors (Table 2).

γ-Oryzanol increases insulin biosynthesis and $[Ca^{2+}]_i$ in islets

Elevation of intracellular cAMP enhances the biosynthesis of insulin (Fehmann and Habener, 1992) and insulin secretion induced by increased $[Ca^{2+}]_i$ in the presence of insulinotropic glucose concentrations (Yada *et al.*, 1993). We therefore assessed the effect of γ-oryzanol and haloperidol on the biosynthesis of insulin and its secretion in response to increased $[Ca^{2+}]_i$ in murine-isolated islets. Both γ-oryzanol and haloperidol significantly increased intracellular insulin contents and the $[Ca^{2+}]_i$ response (Figure 4). Of note, both γ-oryzanol and haloperidol enhanced the first phase of $[Ca^{2+}]_i$ responses to high glucose (Figure 4B,C). These results also reinforce the notion that γ-oryzanol increases intracellular cAMP levels and subsequently enhances GSIS through suppression of D_2 receptor signalling.

γ-Oryzanol suppresses D_2 receptor signalling in pancreatic islets from HFD-fed mice

Following treatment of γ-oryzanol (320 $\mu g \cdot g^{-1}$ per body weight per day) for 13 weeks, glucose level in mice on a HFD was 1280 ± 50 $mg \cdot L^{-1}$, which was significantly decreased compared with those in mice on the HFD alone (1570 ± 80 $mg \cdot L^{-1}$, $P < 0.01$). Body weight in mice fed HFD with γ-oryzanol was 31.7 ± 0.8 g, which was comparable to that in mice fed HFD alone (30.4 ± 1.2 g). Areas of islet cells stained with antibody to TH, the rate-limiting enzyme of dopamine synthesis (Figure 5A), and antibody to DAT, which mediates dopamine uptake (Figure 5B), were increased in pancreatic islets from HFD-fed mice, whereas the stained areas were markedly decreased after treatment with γ-oryzanol. Consequently, the ratio of TH-positive or DAT-positive cell areas to the total islet area was significantly increased in HFD-fed mice, and was substantially decreased by the treatment with γ-oryzanol (Figure 5C,D). IHC analyses suggested that TH was localized in beta cells, while DAT was not confined to α-cells, beta cells or δ-cells (Figure 6).

We assessed protein and mRNA expression levels of genes involved in D_2 receptor signalling including D_2 receptors (*Drd2*), TH (*Th*), DAT (*Slc6a3*) and the vesicular monoamine transporter type 2 (VMAT2; *Slc18a2*), which transports dopamine into vesicles. In pancreatic islets from HFD-fed mice, the mRNA levels of *Drd2*, *Th* and *Slc6a3* were considerably elevated, while that of *Slc18a2*, also known as a functional marker of insulin production (Harris *et al.*, 2008), was markedly decreased (Figure 5E–H). Importantly, administration of γ-oryzanol depressed the mRNA levels of these genes (Figure 5E–H). In parallel with mRNA levels, protein levels of D_2 receptors, TH and DAT were concomitantly decreased by γ-oryzanol (Figure 5I–L).

γ-Oryzanol decreases glucagon secretion from murine islets

γ-Oryzanol significantly decreased glucagon levels in plasma of HFD-fed mice (Figure 7A) and in media of isolated islet cultures (Figure 7B). To test the possibility that γ-oryzanol directly acted on α-cells, a murine α-cell line, α-TC cells, was treated with γ-oryzanol. As shown in Figure 7C, glucagon secretion from α-TC cells was reduced, concentration-dependently, by glucose. It should be noted that mRNA level of *Drd2* in α-TC cells was extremely low, compared with those in isolated islets and MIN6 cells, while that of *Drd3* was about the same in the three types of cells (Figure 7D,E). In α-TC cells, γ-oryzanol and haloperidol did not affect glucagon secretion in both basal and palmitate-stimulated conditions (Figure 7F,G). IHC analyses of pancreatic islets from mice on a HFD demonstrated that γ-oryzanol augmented the intensity of insulin staining, while attenuating the average size of pancreatic islets, as well as the ratio of α-cells to the total islet area (Figure 7H–J). These results raised the possibility that γ-oryzanol reduced the increased secretion of glucagon via mechanisms independent of α-cells.

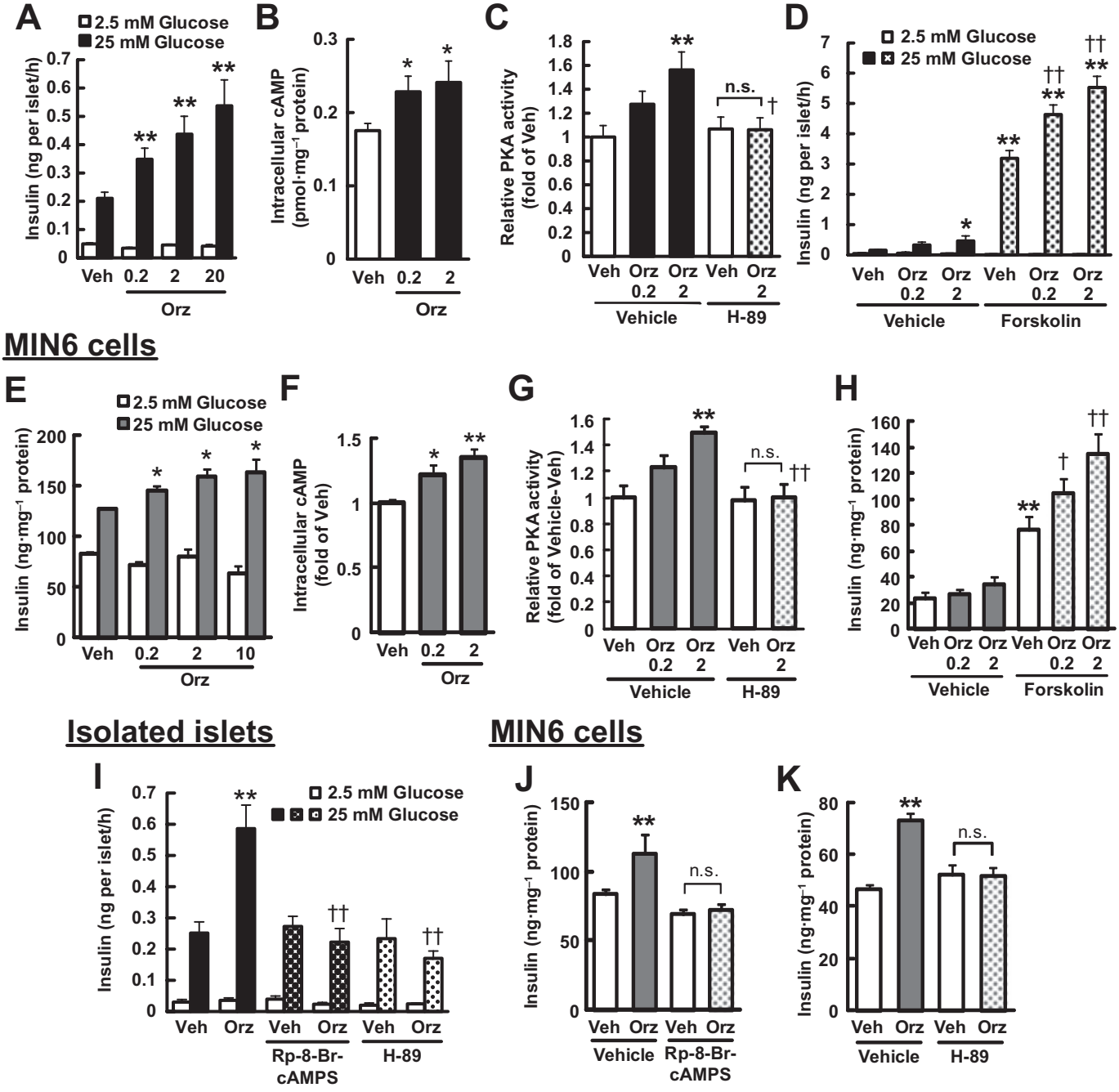

Figure 2

γ-Oryzanol enhances GSIS through activation of the cAMP/PKA pathway in murine isolated islets and MIN6 cells. Murine isolated islets (A–D, I) and MIN6 cells (E–H, J, K) were treated with the indicated concentrations of γ-oryzanol (Orz; 0.2, 2, 10 or 20 μg·mL^{-1}). (A, E) Insulin secretion was assessed following 25 mM glucose treated in murine-isolated islets (n = 10) (A) and MIN6 cells (n = 8) (E). (B, C, F, G) γ-Oryzanol (Orz; 0.2 or 2 μg·mL^{-1}) increased intracellular cAMP levels (B, F) and PKA activity (C, G) following 25 mM glucose in islets (n = 12) (B, C) and MIN6 cells (n = 8) (F, G). (D, H) Effects of γ-oryzanol (Orz; 0.2 or 2 μg·mL^{-1}) on insulin secretion enhanced by 10 μM forskolin in islets (n = 10) (D) and MIN6 cells following 2.5 mM glucose (n = 8) (H). (I–K) GSIS by 25 mM glucose was suppressed by 10 μM Rp-8-Br-cAMPS or 10 μM H-89 in islets (n = 10) (I) and MIN6 cells (n = 8) (J, K) treated with γ-oryzanol (Orz; 2 μg·mL^{-1}). Islets used in each experiment were isolated from eight mice, and they were pooled and divided into indicated number of groups. *P < 0.05, **P < 0.01 versus vehicle (Veh)-treated islets. $^{\dagger\dagger}P$ < 0.01 versus cells treated with vehicle (Veh) and γ-oryzanol (2 μg·mL^{-1}). n.s., not significant. Data are expressed as means ± SEM.

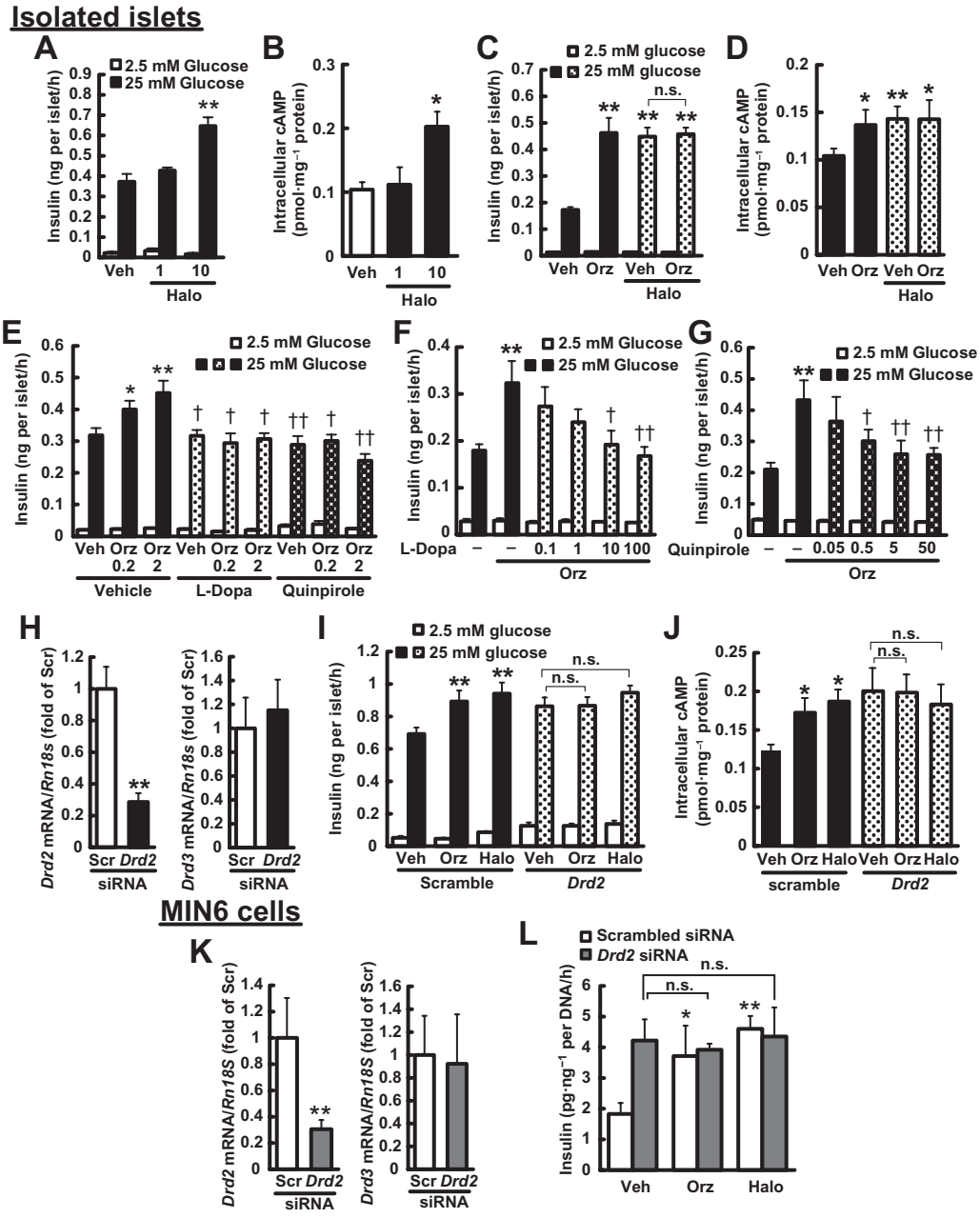

Figure 3

γ-Oryzanol enhances GSIS through the suppression of D_2 receptor signalling in murine isolated islets and MIN6 cells. (A, B) Haloperidol (1, 10 μM) increased insulin secretion (A) and intracellular cAMP levels (B) in isolated islets following 25 mM glucose (n = 12). (C, D) γ-Oryzanol (Orz; 2 μg·mL^{-1}) and haloperidol (10 μM) had no additive effect on insulin secretion (n = 12) (C) and intracellular cAMP levels (n = 24) (D) in isolated islets following 25 mM glucose. Islets used in each experiment were isolated from six mice, and they were pooled and divided into indicated number of groups. (E) Insulin secretion enhanced by the indicated concentrations of γ-oryzanol (Orz; 0.2 or 2 μg·mL^{-1}) was suppressed by 10 μM L-DOPA or 5 μM quinpirole and in isolated islets (n = 10; islets isolated from 12 mice were pooled and divided into indicated number of groups). (F, G) Insulin secretion in isolated islets treated with γ-oryzanol (Orz; 2 μg·mL^{-1}) was suppressed by the indicated concentrations of L-DOPA (0.1, 1, 10 or 100 μM) (F) or quinpirole (0.05, 0.5, 5 or 50 μM) (G) (n = 10–14; islets isolated from eight mice were pooled and divided into indicated number of groups). *P < 0.05, **P < 0.01 versus islets treated with vehicle (Veh). $^{\dagger}P$ < 0.05, $^{\dagger\dagger}P$ < 0.01 versus islets treated with vehicle (Veh) and γ-oryzanol. (H–L) Isolated pancreatic islets (H–J) and MIN6 cells (K, L) were treated with *Drd2* siRNA. (H, K) Level of mRNA expression for *Drd2* and *Drd3*. The levels were normalized against those of *Rn18s*. **P < 0.01 versus scrambled siRNA-transfected islets or cells (Scr). (I, L) Insulin secretion in siRNA-treated islets (I) and MIN6 cells (L) was not enhanced by γ-oryzanol (Orz; 2 μg·mL^{-1}) or haloperidol (10 μM) (n = 15–20). (J) γ-Oryzanol (Orz; 2 μg·mL^{-1}) and haloperidol (Halo; 10 μM) had no effect on intracellular cAMP levels in siRNA-treated islets (n = 10). Islets isolated from eight mice were pooled and divided into indicated number of groups. **P < 0.01 versus scrambled siRNA-transfected islets treated with vehicle (Veh). n.s., not significant. Amount of insulin secretion from MIN6 cells was normalized against the cellular protein content. Data are expressed as means ± SEM.

Table 2

Agonist or antagonist activities of γ-oryzanol for dopamine receptors (DRD1–DRD5)

	Agonist		Antagonist	
	% Activity	*Z*-factor	% Inhibition	*Z*-factor
DRD1	0	0.73	10	0.84
DRD2L	1	0.79	–5	0.81
DRD2S	2	0.81	5	0.91
DRD3	13	0.48	–13	0.79
DRD4	1	0.86	–2	0.77
DRD5	–2	0.75	9	0.87

Percentage of activity in γ-oryzanol for each dopamine receptor was calculated relative to the basal or maximal agonist values of dopamine. Percentage of inhibition by γ-oryzanol for each dopamine receptor was calculated relative to the basal or EC_{80} values for dopamine (antagonist activity). GPCR targets: DRD1, dopamine D_1 receptor; DRD2L, long form of the dopamine D_2 receptor; DRD2S, short form of the dopamine D_2 receptor; DRD3, dopamine D_3 receptor; DRD4, dopamine D_4 receptor; DRD5, dopamine D_5 receptor.

Discussion and conclusions

The major findings in the present study are summarized by the scheme shown in Figure 8. Here, we have demonstrated that, in mice, γ-oryzanol acted directly on pancreatic islets and enhanced GSIS *in vivo* and *in vitro* (Figures 1 and 2). Such a reinforcement of GSIS by γ-oryzanol was mediated by the local activation of the cAMP/PKA amplifying pathway (Figures 2 and 4). Along with chemical agonists for a variety of fatty acid receptors, cAMP/PKA amplifying pathways in pancreatic beta cells are promising drug targets for the treatment of type 2 diabetes (Drucker, 2006; Rayasam *et al.*, 2007; Ohishi and Yoshida, 2012). In this context, γ-oryzanol may be potentially useful as an alternative or a partner of combination therapies with incretin-related drugs.

To our knowledge, the present study is the first to demonstrate that protein and mRNA expression of molecules involved in D_2 receptor signalling was considerably elevated in pancreatic islets from mice fed on a HFD. Moreover, supplementation with γ-oryzanol corrected the dysregulation of these molecules *in vivo* (Figure 5). As increased signal transduction by D_2 receptors in pancreatic beta cells suppresses the secretion of insulin (Rubi *et al.*, 2005; Simpson *et al.*, 2012), such an effect of γ-oryzanol may be beneficial for individuals with glucose intolerance and type 2 diabetes. To date, how transcription of *Drd2* is regulated is largely undefined. It is possible that consensus element of NF-κB in the promoter region of *Drd2* (Bontempi *et al.*, 2007) is related to the HFD-induced dysregulation of D_2 receptors in isolated islets. Apart from the direct action of γ-oryzanol on pancreatic islets, it is also possible that improvement of hyperglycaemia *per se* may influence the expression of molecules involved in D_2 receptor signalling. In this context, further studies are necessary to elucidate fully the molecular mechanisms involved.

Intriguingly, in HFD-induced obese rodents, expression of genes involved in D_2 receptor signalling in the brain reward system (e.g. striatum, ventral tegmental area) was clearly decreased, resulting in a profound addiction to fatty foods (Li *et al.*, 2009; Johnson and Kenny, 2010). Furthermore, recent studies in rodents demonstrated that HFD-induced decrement in D_2 receptor expression in the brain reward system was closely associated with the hyper-methylation in the promoter region of the *Drd2* gene (Vucetic *et al.*, 2012). Studies are ongoing in our laboratory to investigate whether there is HFD-induced epigenetic dysregulation of the D_2 receptor signalling in pancreatic islets or beta cells.

In isolated islets and MIN6 cells, experiments with RNA interference for *Drd2* and with exogenous D_2 receptor ligands demonstrated that γ-oryzanol augmented GSIS via the suppression of D_2 receptor signalling (Figure 3). Enhancement of GSIS by γ-oryzanol was suppressed by L-DOPA (Figure 3E,F), while γ-oryzanol has neither agonist nor antagonist activities at D_2 receptors (Table 2). These findings suggest that γ-oryzanol has inhibitory effects on local dopamine synthesis.

In the pathophysiology of diabetes mellitus, exaggerated secretion of glucagon from pancreatic α-cells contributes to the vicious cycle of glucose dyshomeostasis (Holst, 2007). We demonstrated that γ-oryzanol substantially ameliorated the exaggerated secretion of glucagon in both HFD-fed mice and murine-isolated islets (Figure 7). As D_2 receptors are confined to beta cells in pancreatic islets in mice (Rubi *et al.*, 2005), our data raise the possibility that γ-oryzanol would not directly affect glucagon secretion from α-cells. To support this notion, we demonstrated in an α-cell line, α-TC cells, that γ-oryzanol and haloperidol did not affect glucagon secretion in either basal or palmitate-stimulated conditions (Figure 7F,G). The secretion of glucagon is known to be regulated by the central and peripheral nervous system as well as intra-islet paracrine factors including insulin, GABA and somatostatin (Ishihara *et al.*, 2003; Kawamori *et al.*, 2009; Walker *et al.*, 2011). For instance, postprandial glucagon release is strongly suppressed by GLP-1 and the effect of GLP-1 is mediated, at least partly, by somatostatin (Holst, 2007; Seino *et al.*, 2010). In this context, our results raise the possibility that γ-oryzanol may reduce increased secretion of glucagon via α-cell-independent, intra-islet paracrine factors.

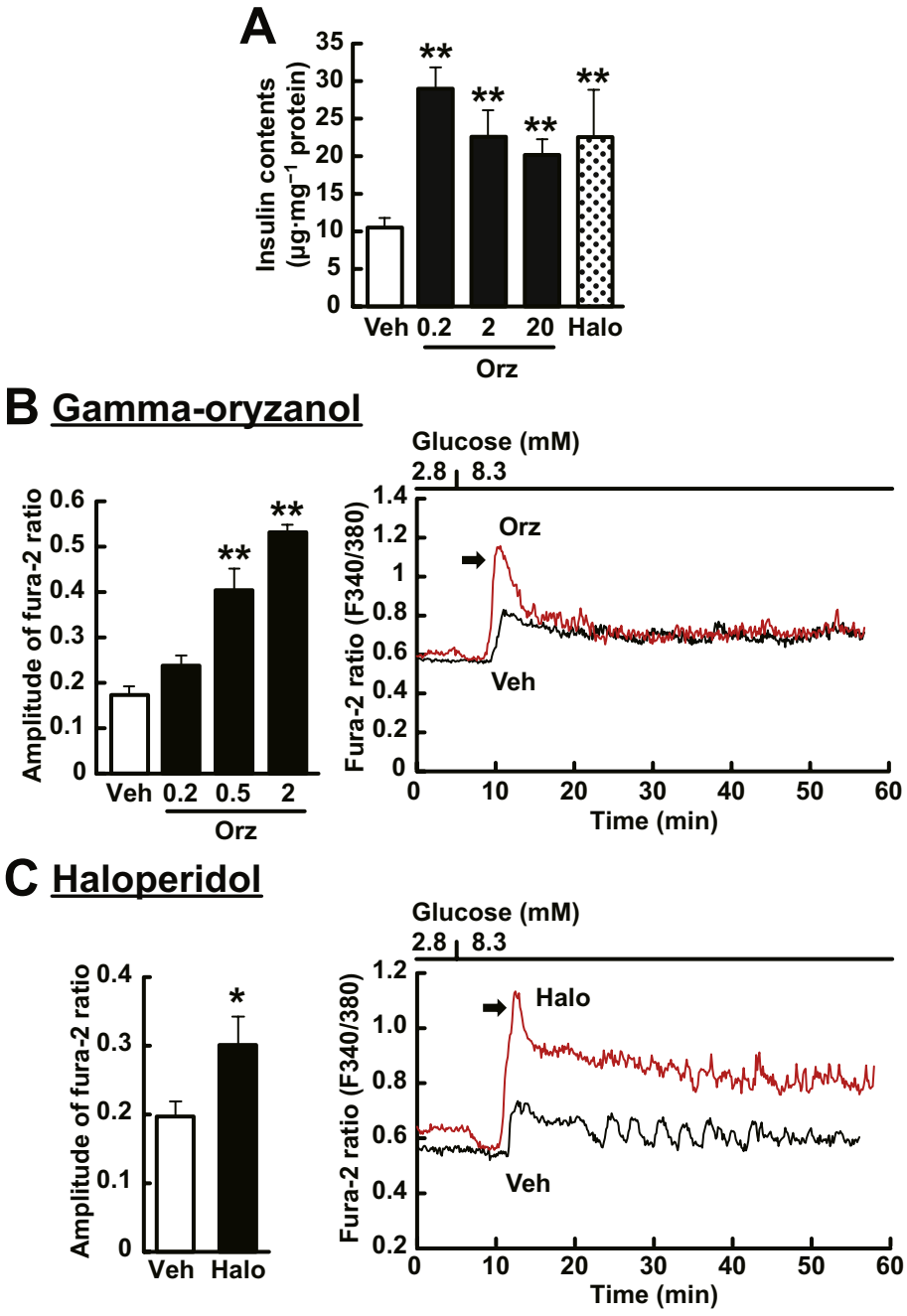

Figure 4

γ-Oryzanol increases intracellular insulin contents and $[Ca^{2+}]_i$ in murine isolated islets. (A) γ-Oryzanol (Orz; 0.2, 2 or 20 μg·mL^{-1}) and haloperidol (Halo; 10 μM) increased intracellular insulin contents ($n = 14$). (B, C) The representative $[Ca^{2+}]_i$ responses to 8.3 mM glucose in islets incubated with γ-oryzanol or haloperidol. Both 2 μg·mL^{-1} γ-oryzanol (B) and 10 μM haloperidol (C) potentiated the first-phase $[Ca^{2+}]_i$ response to 8.3 mM glucose in murine single islet. The peak amplitude of $[Ca^{2+}]_i$ responses was significantly enhanced by γ-oryzanol (Orz; 0.2, 0.5 or 2 μg·mL^{-1}) (B) (Veh, $n = 8$, Orz 0.2, $n = 12$, Orz 0.5, $n = 5$, Orz 2, $n = 3$; islets isolated from three mice were pooled and divided into indicated number of groups) and haloperidol (C) (Veh, $n = 12$, Halo, $n = 10$; islets isolated from two mice were pooled and divided into indicated number of groups). *$P < 0.05$, **$P < 0.01$ versus vehicle (Veh)-treated islets. Data are expressed as means ± SEM.

Regarding the effects of γ-oryzanol on food intake in mice, we previously reported that γ-oryzanol did not affect the total amount of food intake (chow: 16.8 ± 0.5 g per week, HFD: 16.4 ± 0.4 g per week, HFD + γ-oryzanol: 16.2 ± 0.5 g per week). However, γ-oryzanol does reduce the preference for fatty foods in mice (Kozuka *et al.*, 2012). Based on these findings, in the current experimental settings, the insulinotropic effects of γ-oryzanol on pancreatic islets should be

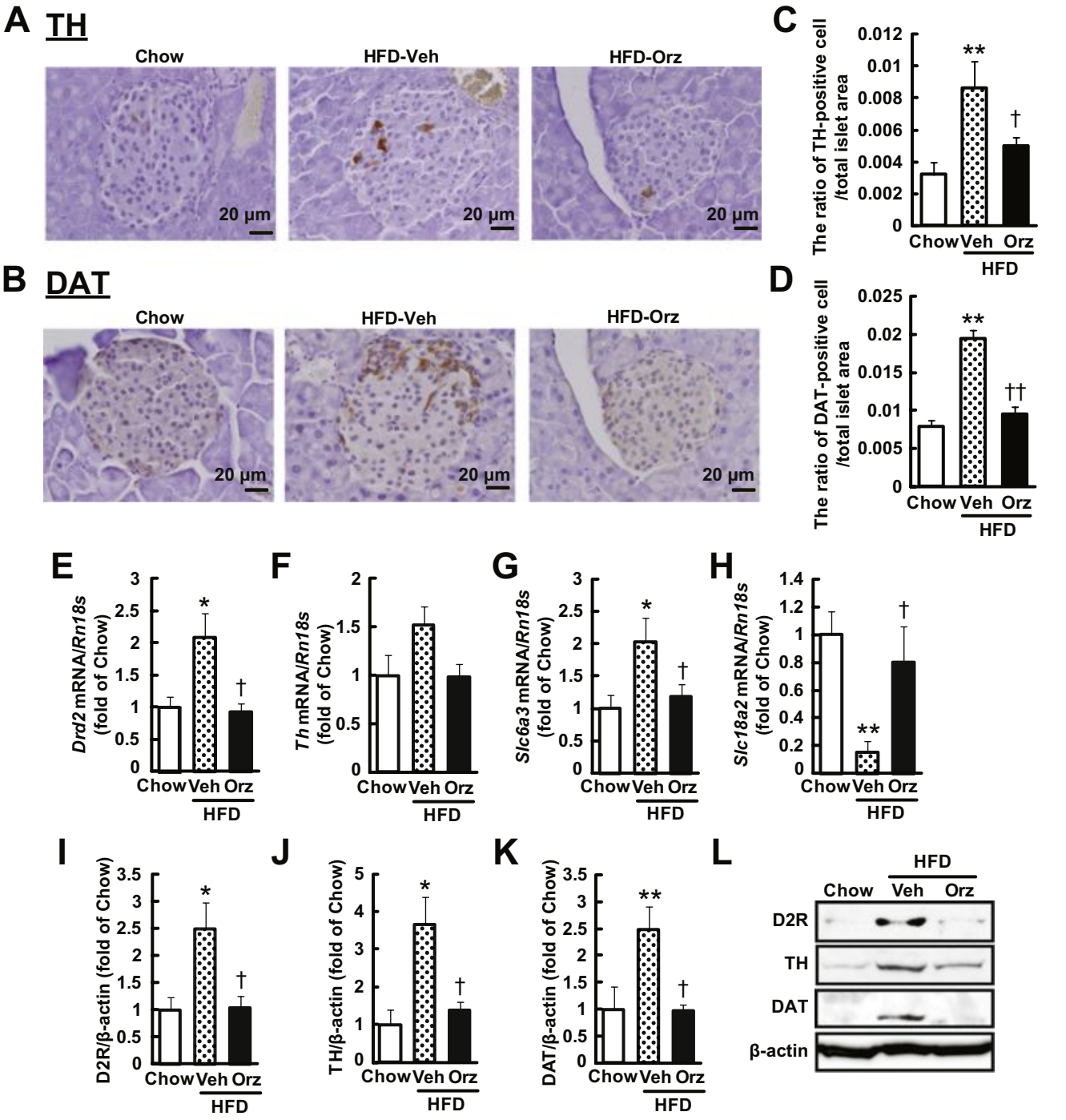

Figure 5

γ-Oryzanol suppresses the expression of molecules involved in D_2 receptor signalling in murine pancreatic islets from mice fed HFD. (A, B) IHC analyses of pancreatic islets from HFD-fed mice treated with γ-oryzanol (Orz). Paraffin-embedded sections were stained with anti-TH (A) or anti-DAT (B) antibodies. Scale bar, 20 μm; magnification, ×400. (C, D) The ratios of TH-positive (C) and DAT-positive (D) cell area to the total islet area were attenuated by the treatment with γ-oryzanol in HFD-fed mice (chow, $n = 6$, HFD-Veh, $n = 8$, HFD-Orz, $n = 8$). $^{**}P < 0.01$ versus chow-fed mice. $^{\dagger}P < 0.05$, $^{\dagger\dagger}P < 0.01$ versus vehicle (Veh)-treated HFD-fed mice. (E–H) Expression levels of *Drd2* (E), *Th* (F), *Slc6a3* (DAT) (G) and *Slc18a2* (VMAT2) (H) mRNAs in pancreatic islets from HFD-fed mice were decreased by γ-oryzanol (Orz; 320 $\mu g \cdot g^{-1}$ per body weight per day) ($n = 6$). The mRNA levels were determined by real-time PCR. The levels were normalized by those of *Rn18s* (18S rRNA). (I–L) Protein levels of D_2 receptors (I), TH (J) and DAT (K) in pancreatic islets from HFD-fed mice were decreased by γ-oryzanol ($n = 6$). Protein levels were determined by Western blotting. The values were normalized against those of β-actin protein. $^{*}P < 0.05$, $^{**}P < 0.01$ versus chow-fed mice. $^{\dagger}P < 0.05$ versus vehicle (Veh)-treated HFD-fed mice. Data are expressed as means ± SEM.

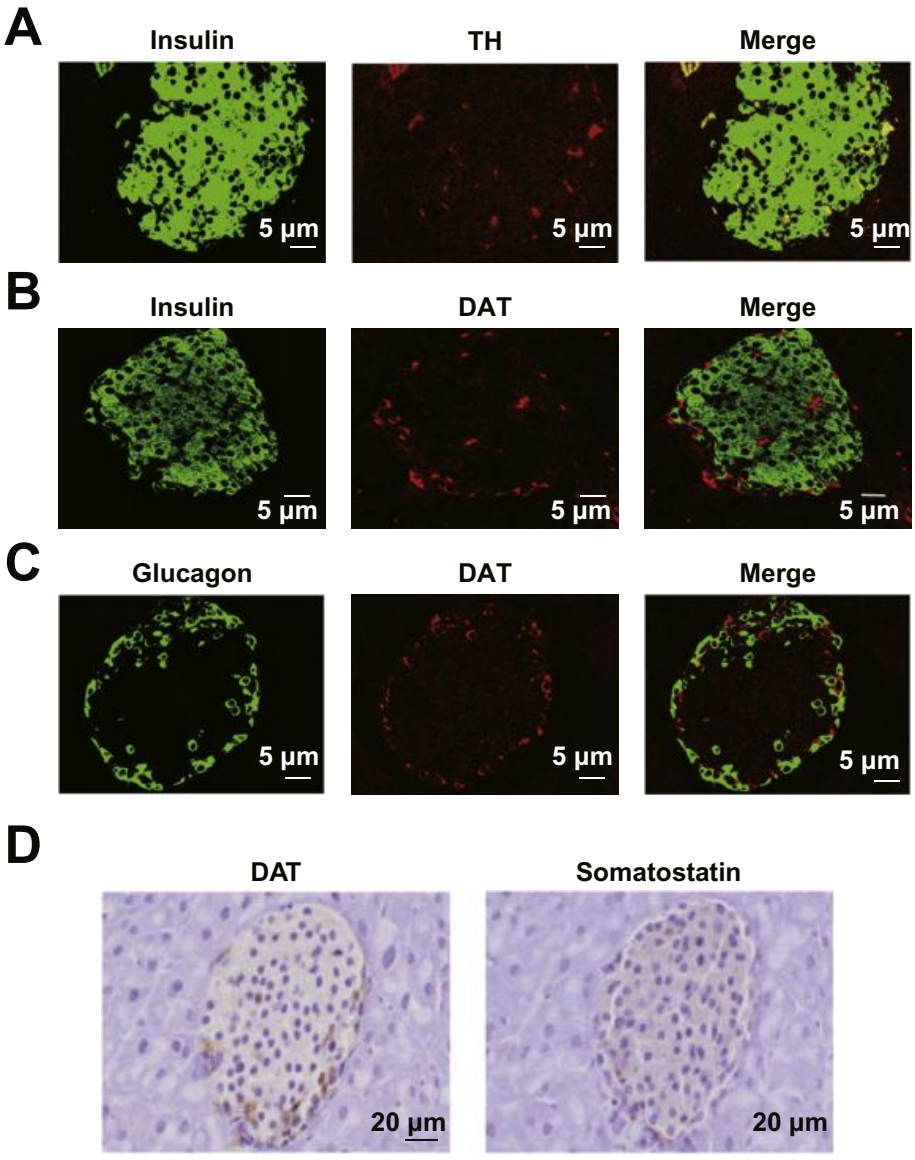

Figure 6

TH was localized in beta cells, whereas DAT was not confined to α-cells, beta cells or δ-cells. IHC analyses of pancreatic islets from HFD-fed mice. Paraffin-embedded sections were co-stained with anti-TH (red) and anti-insulin (green) (A), anti-DAT (red) and anti-insulin (green) (B), or anti-DAT (red) and anti-glucagon (green) (C) antibodies. Scale bar, 5 μm; magnification, ×600. (D) Serial paraffin-embedded sections were stained with anti-DAT and anti-somatostatin antibodies. Scale bar, 20 μm; magnification, ×400.

largely attributed to its direct mechanism. Moreover, as demonstrated in Figure 1, oral administration of γ-oryzanol to mice fed chow diet did not increase plasma GLP-1 level. The results of β-arrestin assays also support the notion that γ-oryzanol did not act as a ligand for GLP-1 receptor. Notably, secretion of GLP-1 is controlled strongly by a vagal nerve-mediated central mechanism (Drucker, 2006). However, even in vagotomized mice, γ-oryzanol markedly increased the plasma insulin levels during ipGTTs (Figure 1). These data suggest that γ-oryzanol acts directly on pancreatic islets and enhances GSIS independently of GLP-1 receptor signalling. Furthermore, we recently demonstrated that γ-oryzanol protects beta cells against ER stress-induced apoptosis in HFD-fed mice (Kozuka *et al.*, 2015). Taken together, γ-oryzanol exhibited metabolically beneficial effects on glucose homeostasis in a GLP-1 independent, unique insulinotropic manner.

The present study unveiled the mechanism, at least in part, whereby γ-oryzanol protects pancreatic islets against HFD-induced dysfunction and augments GSIS via the

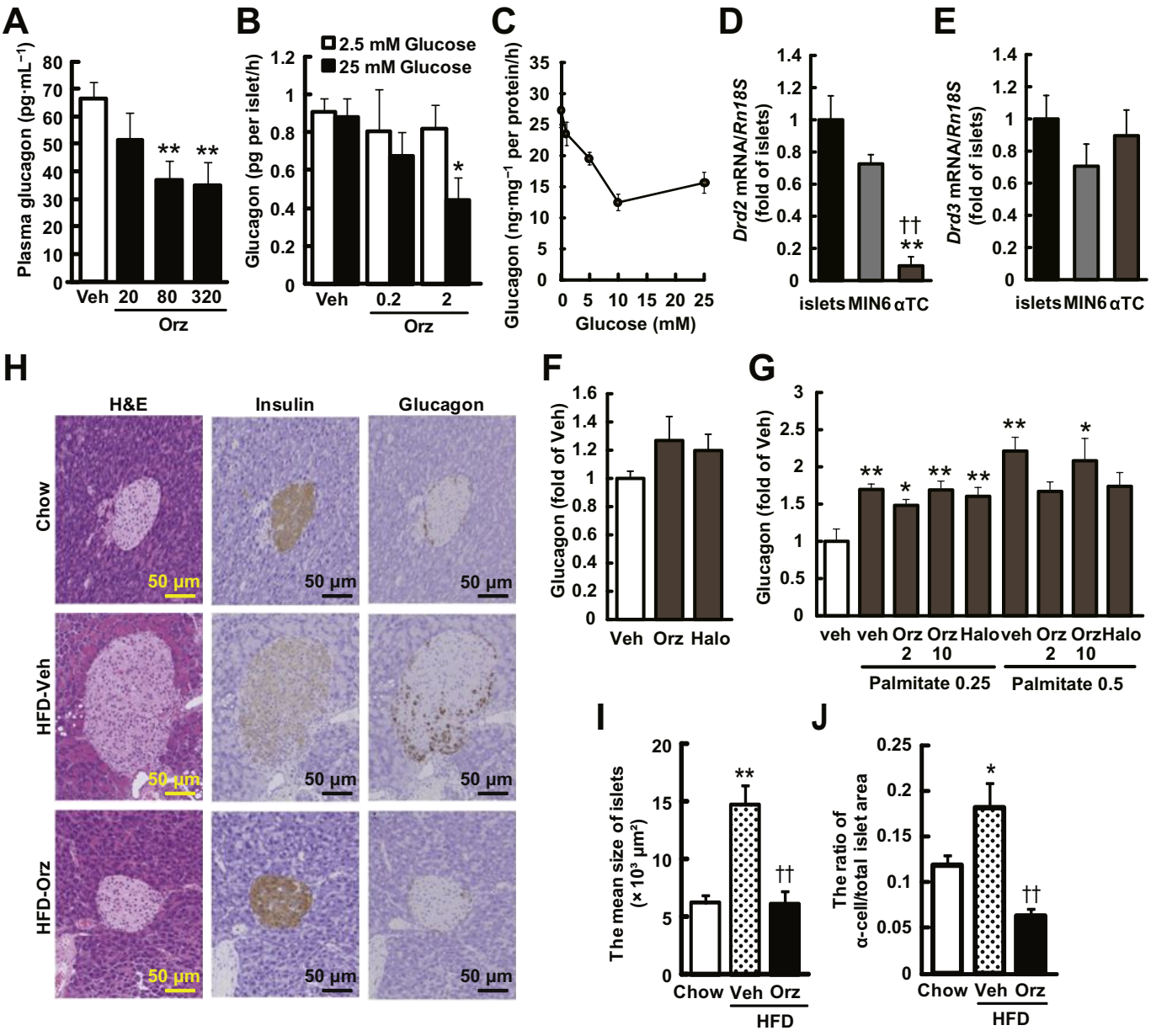

Figure 7

γ-Oryzanol ameliorates increased secretion of glucagon in HFD-fed mice and from murine isolated islets. (A) Plasma glucagon levels in HFD-fed mice treated with the indicated doses of γ-oryzanol (Orz) after a 4 h fast (20, 80 or 320 μg·g^{-1} per body weight per day; $n = 6$). (B) Glucagon secretion in isolated pancreatic islets was decreased by γ-oryzanol (Orz; 0.2 or 2 μg·mL^{-1}) following the exposure to 25 mM glucose ($n = 10$; islets isolated from three mice were pooled and divided into indicated number of groups). (C) Glucagon secretion was stimulated by indicated concentrations of glucose (0, 1, 5, 10 and 25 mM). Amount of glucagon secretion was normalized against the cellular protein content. (D, E) Expression level of *Drd2* and *Drd3* in isolated islets, MIN6 and α-TC cells. Levels of mRNA expression for *Drd2* (D) and *Drd3* (E) in three types of cells ($n = 12$). The mRNA levels were determined by real-time PCR. The levels were normalized against those of *Rn18s*. $^{**}P < 0.01$ versus islets, $^{††}P < 0.01$ versus MIN6 cells. (F, G) In α-TC cells treated with γ-oryzanol (Orz; 2 or 10 μg·mL^{-1}) or haloperidol (10 μM), glucagon secretion was assessed following 5 mM glucose (F) or palmitate (0.25 and 0.5 mM following 16.7 mM glucose (G). $^{*}P < 0.05$, $^{**}P < 0.01$ versus HFD-fed mice, islets, or α-TC cells treated with vehicle (Veh). (H) IHC analyses of isolated pancreatic islets from HFD-fed mice treated with γ-oryzanol (Orz; 320 μg·g^{-1}·day^{-1}). Serial paraffin-embedded sections were stained with haematoxylin and eosin (H&E) (upper panel) or anti-insulin (middle panel), anti-glucagon (lower panel) antibodies. Scale bar, 50 μm; magnification, ×200. (I, J) The mean sizes of islets (I) and ratios of glucagon-positive α-cell areas to the total islet area (J) were calculated ($n = 6$–8). $^{*}P < 0.05$, $^{**}P < 0.01$ versus chow-fed mice. $^{††}P < 0.01$ versus HFD-fed mice treated with vehicle (Veh). Data are expressed as means ± SEM.

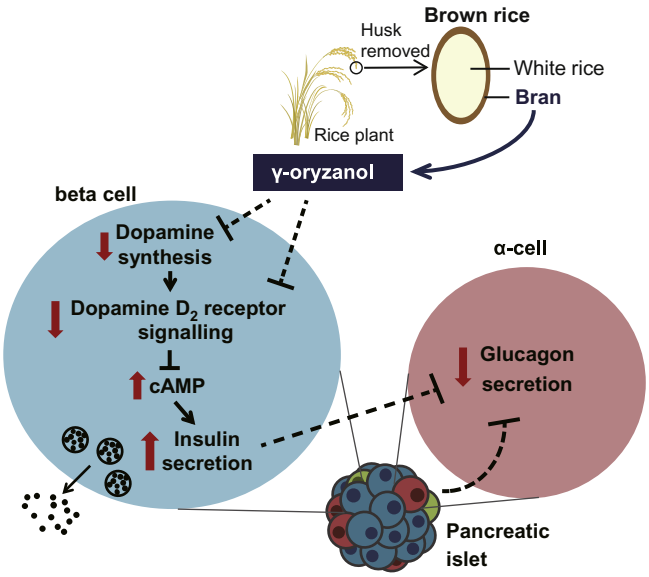

Figure 8

Scheme illustrating the effects of γ-oryzanol on pancreatic islets in mice. In pancreatic islets and beta cells, γ-oryzanol suppresses D_2 receptor signalling, at least partly via the inhibition of local dopamine synthesis, leading to an increase in the intracellular cAMP level. Consequently, GSIS is augmented via the cAMP/PKA pathway (amplifying pathway). On the other hand, γ-oryzanol ameliorates exaggerated secretion of glucagon from pancreatic α-cells, not via the direct action on α-cells, but presumably via some intra-islet paracrine factors.

attenuation of local D_2 receptor signalling in mice. This series of unexpected actions of γ-oryzanol may lead to a novel, natural food-based preventive treatment for type 2 diabetes.

Acknowledgements

We thank M. Takaki (University of the Ryukyus, Japan) and F. Y. Wei (Kumamoto University, Japan) for technical help. We are grateful to M. Hirata, I. Asato and C. Noguchi (University of the Ryukyus, Japan) for assistance. The α-TC cells were kindly provided by T. Kitamura (Gunma University, Japan). This work was supported in part by Grants-in-Aid from Japan Society for the Promotion of Science (JSPS; KAKENHI Grant Nos. 24591338 and 25·9668), Council for Science, Technology and Innovation (CSTI), Cross-ministerial Strategic Innovation Promotion Program (SIP), 'Technologies for creating next-generation agriculture, forestry and fisheries', Takeda Science Foundation (Specified Research Grant), Society for Woman's Health Science Research (13-A1-001), the Nestlé Nutrition Council Japan, Narishige Neuroscience Research Foundation, Lotte Foundation, Leave a Nest Grants, Metabolic Syndrome Foundation and Specified Project 'Establishing a research hub toward the development of an intellectual cluster in Okinawa Prefecture' (2011–2014). C. K. is a Research Fellow of JSPS.

Author contributions

C. K., C. S.-O. and M. N. performed the research. C. K. and H. M. designed the research study. S. S., R. U., M. H., Y. O., H. T., C. S.-O., C. T., M. M., M. T., S. I., M. N., T. Y., J. M., S. O. and M. S. provided invaluable advice on research design and data interpretation. J. M. and S. O. contributed essential reagents or tools. C. K. analysed the data. C. K. and H. M. wrote the paper.

Conflict of interest

We declare that we have no conflict of interest.

References

Alexander SP, Benson HE, Faccenda E, Pawson AJ, Sharman JL, Spedding M *et al.* (2013a). The concise guide to PHARMACOLOGY 2013/14: G protein-coupled receptors. Br J Pharmacol 170: 1459–1581.

Alexander SPH, Benson HE, Faccenda E, Pawson AJ, Sharman JL Spedding M *et al.* (2013b). The concise guide to PHARMACOLOGY 2013/14: Transporters. Br J Pharmacol 170: 1706–1796.

Alexander SPH, Benson HE, Faccenda E, Pawson AJ, Sharman JL Spedding M *et al.* (2013c). The concise guide to PHARMACOLOGY 2013/14: Enzymes. Br J Pharmacol 170: 1797–1867.

Ariyama Y, Tanaka Y, Shimizu H, Shimomura K, Okada S, Saito T *et al.* (2008). The role of CHOP messenger RNA expression in the link between oxidative stress and apoptosis. Metabolism 57: 1625–1635.

Bontempi S, Fiorentini C, Busi C, Guerra N, Spano P, Missale C (2007). Identification and characterization of two nuclear factor-kappaB sites in the regulatory region of the dopamine D2 receptor. Endocrinology 148: 2563–2570.

Chu ZL, Jones RM, He H, Carroll C, Gutierrez V, Lucman A *et al.* (2007). A role for beta-cell-expressed G protein-coupled receptor 119 in glycemic control by enhancing glucose-dependent insulin release. Endocrinology 148: 2601–2609.

Drucker DJ (2006). The biology of incretin hormones. Cell Metab 3: 153–165.

Fehmann HC, Habener JF (1992). Insulinotropic hormone glucagon-like peptide-I(7–37) stimulation of proinsulin gene expression and proinsulin biosynthesis in insulinoma beta TC-1 cells. Endocrinology 130: 159–166.

Garcia-Tornadu I, Ornstein AM, Chamson-Reig A, Wheeler MB, Hill DJ, Arany E *et al.* (2010). Disruption of the dopamine d2 receptor impairs insulin secretion and causes glucose intolerance. Endocrinology 151: 1441–1450.

Giacca A, Xiao C, Oprescu AI, Carpentier AC, Lewis GF (2011). Lipid-induced pancreatic beta-cell dysfunction: focus on in vivo studies. Am J Physiol Endocrinol Metab 300: E255–E262.

Harris PE, Ferrara C, Barba P, Polito T, Freeby M, Maffei A (2008). VMAT2 gene expression and function as it applies to imaging beta-cell mass. J Mol Med (Berl) 86: 5–16.

Henquin JC (2000). Triggering and amplifying pathways of regulation of insulin secretion by glucose. Diabetes 49: 1751–1760.

Hirasawa A, Tsumaya K, Awaji T, Katsuma S, Adachi T, Yamada M *et al*. (2005). Free fatty acids regulate gut incretin glucagon-like peptide-1 secretion through GPR120. Nat Med 11: 90–94.

Holst JJ (2007). The physiology of glucagon-like peptide 1. Physiol Rev 87: 1409–1439.

Ieiri T, Kase N, Hashigami Y, Kobori H, Nakamura T, Shimoda S (1982). [Effects of gamma-oryzanol on the hypothalamo-pituitary axis in the rat]. Nihon Naibunpi Gakkai Zasshi 58: 1350–1356.

Ishihara H, Maechler P, Gjinovci A, Herrera PL, Wollheim CB (2003). Islet beta-cell secretion determines glucagon release from neighbouring alpha-cells. Nat Cell Biol 5: 330–335.

Johnson PM, Kenny PJ (2010). Dopamine D2 receptors in addiction-like reward dysfunction and compulsive eating in obese rats. Nat Neurosci 13: 635–641.

Kahn SE, Hull RL, Utzschneider KM (2006). Mechanisms linking obesity to insulin resistance and type 2 diabetes. Nature 444: 840–846.

Kawamori D, Kurpad AJ, Hu J, Liew CW, Shih JL, Ford EL *et al*. (2009). Insulin signaling in alpha cells modulates glucagon secretion in vivo. Cell Metab 9: 350–361.

Kilkenny C, Browne W, Cuthill IC, Emerson M, Altman DG (2010). Animal research: Reporting in vivo experiments: the ARRIVE guidelines. Br J Pharmacol 160: 1577–1579.

Kozuka C, Yabiku K, Sunagawa S, Ueda R, Taira SI, Ohshiro H *et al*. (2012). Brown rice and its component, gamma-oryzanol, attenuate the preference for high-fat diet by decreasing hypothalamic endoplasmic reticulum stress in mice. Diabetes 61: 3084–3093.

Kozuka C, Yabiku K, Takayama C, Matsushita M, Shimabukuro M, Masuzaki H (2013). Natural food science based novel approach toward prevention and treatment of obesity and type 2 diabetes: recent studies on brown rice and γ-oryzanol. Obes Res Clin Pract 7: e165–e172.

Kozuka C, Sunagawa S, Ueda R, Higa M, Tanaka H, Shimizu-Okabe C *et al*. (2015). Gamma-oryzanol protects pancreatic beta-cells against endoplasmic reticulum stress in male mice. Endocrinology 156: 1242–1250.

Lauffer LM, Iakoubov R, Brubaker PL (2009). GPR119 is essential for oleoylethanolamide-induced glucagon-like peptide-1 secretion from the intestinal enteroendocrine L-cell. Diabetes 58: 1058–1066.

Lerma-Garcia MJ, Herrero-Martinez JM, Simo-Alfonso EF, Mendonca CRB, Ramis-Ramos G (2009). Composition, industrial processing and applications of rice bran gamma-oryzanol. Food Chem 115: 389–404.

Li Y, South T, Han M, Chen J, Wang R, Huang XF (2009). High-fat diet decreases tyrosine hydroxylase mRNA expression irrespective of obesity susceptibility in mice. Brain Res 1268: 181–189.

Marsden CD, Parkes JD (1977). Success and problems of long-term levodopa therapy in Parkinson's disease. Lancet 1: 345–349.

McGrath J, Drummond G, McLachlan E, Kilkenny C, Wainwright C (2010). Guidelines for reporting experiments involving animals: the ARRIVE guidelines. Br J Pharmacol 160: 1573–1576.

Missale C, Nash SR, Robinson SW, Jaber M, Caron MG (1998). Dopamine receptors: from structure to function. Physiol Rev 78: 189–225.

Miyamoto L, Ebihara K, Kusakabe T, Aotani D, Yamamoto-Kataoka S, Sakai T *et al*. (2012). Leptin activates hepatic 5′ AMP-Activated Protein Kinase through sympathetic nervous system and alpha1 adrenergic receptor: a potential mechanism for improvement of fatty liver in lipodystrophy by leptin. J Biol Chem 287: 40441–40447.

Miyazaki J, Araki K, Yamato E, Ikegami H, Asano T, Shibasaki Y *et al*. (1990). Establishment of a pancreatic beta cell line that retains glucose-inducible insulin secretion: special reference to expression of glucose transporter isoforms. Endocrinology 127: 126–132.

Nakata M, Shintani N, Hashimoto H, Baba A, Yada T (2010). Intra-islet PACAP protects pancreatic beta-cells against glucotoxicity and lipotoxicity. J Mol Neurosci 42: 404–410.

Ohishi T, Yoshida S (2012). The therapeutic potential of GPR119 agonists for type 2 diabetes. Expert Opin Investig Drugs 21: 321–328.

Pawson AJ, Sharman JL, Benson HE, Faccenda E, Alexander SP, Buneman OP *et al*.; NC-IUPHAR (2014). The IUPHAR/BPS Guide to PHARMACOLOGY: an expert-driven knowledge base of drug targets and their ligands. Nucl Acids Res 42 (Database Issue): D1098–D1106.

Rayasam GV, Tulasi VK, Davis JA, Bansal VS (2007). Fatty acid receptors as new therapeutic targets for diabetes. Expert Opin Ther Targets 11: 661–671.

Rubi B, Ljubicic S, Pournourmohammadi S, Carobbio S, Armanet M, Bartley C *et al*. (2005). Dopamine D2-like receptors are expressed in pancreatic beta cells and mediate inhibition of insulin secretion. J Biol Chem 280: 36824–36832.

Seino Y, Fukushima M, Yabe D (2010). GIP and GLP-1, the two incretin hormones: similarities and differences. J Diabetes Investig 1: 8–23.

Shimabukuro M, Higa M, Kinjo R, Yamakawa K, Tanaka H, Kozuka C *et al*. (2014). Effects of the brown rice diet on visceral obesity and endothelial function: the BRAVO study. Br J Nutr 111: 310–320.

Simpson N, Maffei A, Freeby M, Burroughs S, Freyberg Z, Javitch J *et al*. (2012). Dopamine-mediated autocrine inhibitory circuit regulating human insulin secretion in vitro. Mol Endocrinol 26: 1757–1772.

Sirtori CR, Bolme P, Azarnoff DL (1972). Metabolic responses to acute and chronic L-dopa administration in patients with parkinsonism. N Engl J Med 287: 729–733.

Smith GP, Jerome C, Cushin BJ, Eterno R, Simansky KJ (1981). Abdominal vagotomy blocks the satiety effect of cholecystokinin in the rat. Science 213: 1036–1037.

Smith GP, Jerome C, Norgren R (1985). Afferent axons in abdominal vagus mediate satiety effect of cholecystokinin in rats. Am J Physiol 249: R638–641.

Sun Q, Spiegelman D, van Dam RM, Holmes MD, Malik VS, Willett WC *et al*. (2010). White rice, brown rice, and risk of type 2 diabetes in US men and women. Arch Intern Med 170: 961–969.

Tanaka T, Masuzaki H, Yasue S, Ebihara K, Shiuchi T, Ishii T *et al*. (2007). Central melanocortin signaling restores skeletal muscle AMP-activated protein kinase phosphorylation in mice fed a high-fat diet. Cell Metab 5: 395–402.

Vallone D, Picetti R, Borrelli E (2000). Structure and function of dopamine receptors. Neurosci Biobehav Rev 24: 125–132.

Vucetic Z, Carlin JL, Totoki K, Reyes TM (2012). Epigenetic dysregulation of the dopamine system in diet-induced obesity. J Neurochem 120: 891–898.

Walker JN, Ramracheya R, Zhang Q, Johnson PR, Braun M, Rorsman P (2011). Regulation of glucagon secretion by glucose: paracrine, intrinsic or both? Diabetes Obes Metab 13 (Suppl. 1): 95–105.

Wei FY, Nagashima K, Ohshima T, Saheki Y, Lu YF, Matsushita M *et al*. (2005). Cdk5-dependent regulation of glucose-stimulated insulin secretion. Nat Med 11: 1104–1108.

Yada T, Itoh K, Nakata M (1993). Glucagon-like peptide-1-(7–36) amide and a rise in cyclic adenosine 3′,5′-monophosphate increase cytosolic free Ca2+ in rat pancreatic beta-cells by enhancing Ca2+ channel activity. Endocrinology 133: 1685–1692.

Zhang JH, Chung TDY, Oldenburg KR (1999). A simple statistical parameter for use in evaluation and validation of high throughput screening assays. J Biomol Screen 4: 67–73.

Zmuda EJ, Powell CA, Hai T (2011). A method for murine islet isolation and subcapsular kidney transplantation. J Vis Exp 50: e2096.

Journal of Pharmacological Sciences 127 (2015) 217–222

Contents lists available at ScienceDirect

Journal of Pharmacological Sciences

journal homepage: www.elsevier.com/locate/jphs

Full paper

Effect of caffeine contained in a cup of coffee on microvascular function in healthy subjects

Katsuhiko Noguchi [a, *], Toshihiro Matsuzaki [a], Mayuko Sakanashi [a], Naobumi Hamadate [a], Taro Uchida [a], Mika Kina-Tanada [a], Haruaki Kubota [a], Junko Nakasone [a], Matao Sakanashi [a], Shinichiro Ueda [b], Hiroaki Masuzaki [c], Shogo Ishiuchi [d], Yusuke Ohya [e], Masato Tsutsui [a, *]

[a] Department of Pharmacology, Graduate School of Medicine, University of the Ryukyus, Okinawa, Japan
[b] Department of Clinical Pharmacology and Therapeutics, Graduate School of Medicine, University of the Ryukyus, Okinawa, Japan
[c] Second Department of Internal Medicine, Graduate School of Medicine, University of the Ryukyus, Okinawa, Japan
[d] Department of Neurosurgery, Graduate School of Medicine, University of the Ryukyus, Okinawa, Japan
[e] Third Department of Internal Medicine, Graduate School of Medicine, University of the Ryukyus, Okinawa, Japan

ARTICLE INFO

Article history:
Received 16 October 2014
Received in revised form
26 December 2014
Accepted 13 January 2015
Available online 28 January 2015

Keywords:
Caffeine
Coffee
Endothelial function
Laser-Doppler flowmetry
Microcirculation

ABSTRACT

Recent epidemiological studies have demonstrated that coffee drinking is associated with reduced mortality of cardiovascular disease. However, its precise mechanisms remain to be clarified. In this study, we examined whether single ingestion of caffeine contained in a cup of coffee improves microvascular function in healthy subjects.

A double-blind, placebo-controlled, crossover study was performed in 27 healthy volunteers. A cup of either caffeinated or decaffeinated coffee was drunk by the subjects, and reactive hyperemia of finger blood flow was assessed by laser Doppler flowmetry. In an interval of more than 2 days, the same experimental protocol was repeated with another coffee in a crossover manner. Caffeinated coffee intake slightly but significantly elevated blood pressure and decreased finger blood flow as compared with decaffeinated coffee intake. There was no significant difference in heart rate between caffeinated and decaffeinated coffee intake. Importantly, caffeinated coffee intake significantly enhanced post-occlusive reactive hyperemia of finger blood flow, an index of microvascular endothelial function, compared with decaffeinated coffee intake.

These results provide the first evidence that caffeine contained in a cup of coffee enhances microvascular function in healthy individuals.

1. Introduction

Coffee is the most widely consumed beverage in the world (1). Coffee contains a variety of pharmacologically active ingredients, and it has long been argued whether coffee drinking is beneficial or harmful for cardiovascular disease (2–4). Recently, a large cohort study, in which more than 400,000 participants were prospectively followed up for 13 years, has demonstrated that coffee consumption is associated with reduced mortality of cardiovascular disease (5). Moreover, a meta-analysis of 23 prospective studies has provided quantitative evidence that coffee intake is inversely related to cardiovascular disease mortality (6). These findings suggest the beneficial cardiovascular actions of coffee. However, its precise mechanisms remain to be elucidated.

The vascular endothelium synthesizes and releases several vasodilating substances, such as prostacyclin, nitric oxide, and endothelium-derived hyperpolarizing factors (EDHF). Evaluation of endothelial function has been shown to provide important prognostic information in patients with cardiovascular disease, as evidenced by the facts that the severity of endothelial dysfunction can predict future cardiovascular events (7, 8) and that improvement of endothelial function by pharmacological interventions reduces the risk of cardiovascular disease. Acute effects of caffeine, a major

* Corresponding authors. Department of Pharmacology, Graduate School of Medicine, University of the Ryukyus, 207 Uehara, Nishihara-cho, Okinawa 903-0215, Japan. Tel.: +81 98 895 1133; fax: +81 98 895 1411.
E-mail addresses: noguchi@med.u-ryukyu.ac.jp (K. Noguchi), tsutsui@med.u-ryukyu.ac.jp (M. Tsutsui).
Peer review under responsibility of Japanese Pharmacological Society.

http://dx.doi.org/10.1016/j.jphs.2015.01.003
1347-8613/

pharmacologically active ingredient of coffee, on human endothelial function of large conduit arteries have been examined in several previous studies by using ultrasound-based measurement of brachial artery diameter during post-occlusive reactive hyperemia. However, the results of those studies are quite inconsistent (9–13). It is generally accepted that flow-dependent dilation of conduit arteries is mediated primarily by nitric oxide (14), while in the microcirculation EDHF rather than nitric oxide have been suggested to play a major role in the reactive hyperemic response (15). Microvessels, but not large arteries, regulate tissue blood blow and systemic blood pressure, and thereby play a key role in the circulatory system. However, no study has ever addressed the effect of caffeine on microvascular function.

Based on the above background, we examined in this study the effect of single ingestion of a cup of caffeinated and decaffeinated coffee on finger microvascular function in healthy subjects by laser Doppler flowmetry.

2. Methods

2.1. Subjects

We recruited twenty-seven healthy subjects (13 men and 14 women; 22–30 years old [mean age, 23.7 ± 2.2]; mean body weight, 58.4 ± 15.1 kg; mean height, 162.9 ± 9.6 cm) in our university, and the subjects who wanted to take part in the study voluntarily were investigated. Subjects taking any medication or smokers were excluded from the study, and the experiments were performed when the subjects were well conditioned. All volunteers were asked to abstain from caffeine-contained beverages at least 12 h before the study. All subjects gave written informed consent, and invasive experiments including blood sampling were approved by the Clinical Trial Ethics Committee of the University of the Ryukyus, according to the declaration of Helsinki and the ethical standard.

2.2. Study design

A double-blind, placebo-controlled, crossover study was performed. All participants were examined on two separate days in a quiet temperature-controlled room. Instant coffee of 2 g with or without caffeine (Taster's Choice™, Nestlé, Vevey, Switzerland) was prepared with 150 ml hot water. Neither sugar nor milk was added. A cup of the caffeinated or decaffeinated coffee was ingested in each subject. Hemodynamic variables and reactive hyperemic response were measured before and every 15 min after coffee intake. In a pilot study, we were not able to continue this experiment more than 75 min because some subjects complained of strong pain due to repeated cuff-compression or a fixed position of the test arm. Thus, we set the experiment time for 75 min. In an interval of more than 2 days, the same experimental protocol was repeated with another coffee in a crossover manner. Blood pressures were measured at the brachial artery using a sphygmomanometer (BP-103i, Nihon Colin, Komaki, Japan). A manchette was placed around the right upper arm, and a mean value of three measurements was used for the statistical analyses. Heart rate was obtained from the sphygmomanometer. The subjects were in a sitting position throughout the experiments.

2.3. Assessment of microvascular function

Finger blood flow was measured by a laser Doppler flowmeter (ALF21, Advance, Tokyo, Japan). A flow-probe (type C) was placed at the tip of the left index finger or thumb. Blood flow was calculated by measuring Doppler shifts derived from moving erythrocytes per photon and the mean photon frequency. As the number of Doppler shifts is proportional to the erythrocyte volume and velocity, blood flow is the product of linearized volume and velocity (16). Post-occlusive reactive hyperemia of finger blood flow was assessed as an index of microvascular endothelial function. A cuff was placed on the left upper arm, and reactive hyperemia of finger blood flow was induced by inflating a cuff for 1 min in order to interrupt arterial blood flow and then deflating it. Peak hyperemic flow was defined as the highest blood flow immediately after cuff deflation. Reactive hyperemia was calculated according to the following equation:

Reactive hyperemia (%) = [(peak hyperemic flow − resting flow)/resting flow] × 100

2.4. Measurement of caffeine and catecholamine levels

Venous blood samples were collected before and 30 min after coffee ingestion in five volunteers. The plasma caffeine levels and caffeine contents in decaffeinated and caffeinated coffee were analyzed by high performance liquid chromatography (HPLC; LC-10AD, Shimadzu, Kyoto, Japan) (17). Plasma catecholamine levels were measured by SRL Inc. (Tokyo, Japan) using the HPLC method.

2.5. Statistical analysis

Statistical analyses were performed by a two-way ANOVA followed by a Bonferoni/Dunn post hoc test. When paired or unpaired data were compared, a paired or unpaired Student's *t*-test, respectively, was applied. The computer software StatView-J 5.0 (SAS Institute Japan Ltd, Tokyo, Japan) was used for the statistical analyses. A value of $P < 0.05$ was considered to be statistically significant. Results are expressed as mean ± SD.

Reproducibility of laser Doppler flowmetry was expressed as within-subject coefficients of variability. In our laboratory, the intra-day variability for finger blood flow was 6.3% (range: 0–27.1%) and that for reactive hyperemia assessed by laser Doppler flowmetry was 21.6% (0–54.2%), and the day-to-day variability for finger blood flow was 26.2% (0–76.1%) and that for reactive hyperemia was 33.7% (0–102%). According to the previous studies, the coefficient of variance < 35% can be deemed acceptable (18).

3. Results

3.1. Caffeine content in decaffeinated and caffeinated coffee and plasma caffeine levels before and after coffee intake

Caffeine content in decaffeinated vs. caffeinated coffee was markedly different (1.37 ± 0.09 vs. 54.5 ± 3.4 mg, respectively) (Fig. 1A). Before coffee intake, plasma caffeine levels were identical between subjects with decaffeinated and caffeinated coffee intake. However, 30 min after coffee intake, plasma caffeine levels were markedly increased in the subjects with caffeinated coffee intake (from 0.75 ± 0.85 to 1.57 ± 1.30 μg/ml, $P < 0.05$), but not in those with decaffeinated coffee intake (from 0.76 ± 0.57 to 0.77 ± 0.60 μg/ml) (Fig. 1B).

3.2. Effects of caffeinated coffee intake on blood pressure and finger blood flow

Before coffee intake, there were no significant differences in baseline hemodynamic variables (i.e., systolic, diastolic, and mean blood pressures, finger blood flow, vascular resistance, or heart rate) in the subjects with decaffeinated and caffeinated coffee intake (Table 1). However, caffeinated coffee intake, but not

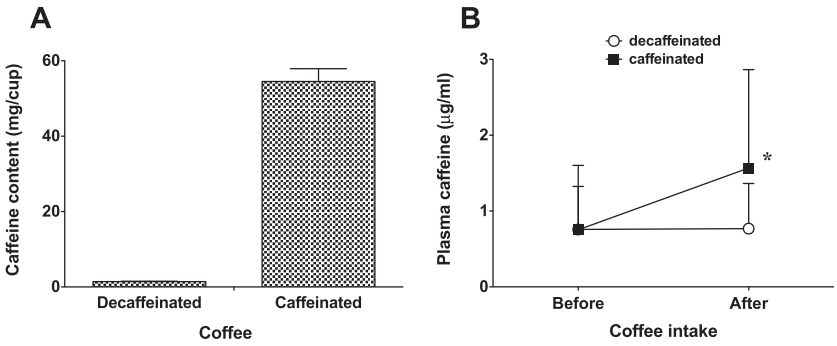

Fig. 1. Caffeine contents in a cup of decaffeinated and caffeinated coffee (A) and plasma caffeine levels before and 30 min after single intake of caffeinated and decaffeinated coffee (B). Data are expressed as mean ± SD. *$P < 0.05$ between before and after coffee intake by a paired *t*-test.

decaffeinated coffee intake, caused slight but significant elevations of systolic, diastolic and mean blood pressures by maximally 2.7, 3.2 and 2.8 mmHg, respectively (each $P < 0.01$, Fig. 2). Furthermore, caffeinated coffee intake significantly reduced finger blood flow (as assessed by laser-Doppler flowmetry, $P < 0.01$, Fig. 3A) and significantly increased vascular resistance of the finger vascular bed when compared with decaffeinated coffee intake ($P < 0.01$, Fig. 3B). On the other hand, there was no significant difference in heart rate in the subjects with decaffeinated and caffeinate coffee intake (Fig. 3C).

3.3. Effects of caffeinated coffee intake on reactive hyperemia of finger blood flow

Before coffee intake, post-occlusive reactive hyperemia of finger blood flow, an index of microvascular endothelial function, were comparable between the subjects with decaffeinated and caffeinated coffee (8.7 ± 4.3 and 10.0 ± 3.4 ml/min/100 g, respectively). However, caffeinated coffee intake significantly enhanced post-occlusive reactive hyperemia of finger blood as compared with decaffeinated coffee intake ($P < 0.01$, Fig. 4).

3.4. Plasma catecholamine levels

Plasma norepinephrine levels did not significantly differ between the subjects with decaffeinated and caffeinated coffee intake at baseline (336 ± 132 vs. 317 ± 165 pg/ml) and at 30 min after the intake (271 ± 95 vs. 272 ± 125 pg/ml). Plasma epinephrine levels also did not significantly alter between the subjects with decaffeinated and caffeinated coffee intake at baseline (35.8 ± 12.5 vs. 33.3 ± 18.5 pg/ml) and at 30 min after the intake (32.0 ± 11.2 vs. 25.8 ± 13.5 pg/ml). The respective plasma catecholamine levels did not significantly change before and after coffee intake.

Table 1
Baseline characteristics in subjects with decaffeinated and caffeinated coffee intake.

Variables	Decaffeinated	Caffeinated	*P* value
Systolic BP (mmHg)	104.9 ± 12.4	106.2 ± 11.2	0.346
Diastolic BP (mmHg)	58.0 ± 8.3	59.1 ± 6.6	0.297
Mean BP (mmHg)	73.6 ± 8.8	74.8 ± 7.6	0.264
Finger blood flow (ml/min/100 g)	23.6 ± 7.7	23.3 ± 7.9	0.916
Vascular resistance (unit)	3.43 ± 1.15	3.67 ± 1.63	0.543
Reactive hyperemia (%)	40.8 ± 25.4	50.3 ± 27.1	0.125
Heart rate (bpm)	74.6 ± 9.4	74.3 ± 8.6	0.815

BP = blood pressure, Vascular resistance = vascular resistance of the finger vascular bed (finger blood flow/mean BP), Reactive hyperemia (%) = 100 × (post-occlusive increase in finger blood flow)/(baseline finger blood flow).

4. Discussion

To the best of our knowledge, this is the first study examining the acute effect of caffeine on endothelial function in the human finger cutaneous microcirculation. The present study demonstrates that an intake of caffeine contained in a cup of coffee may cause a favorable effect on microvascular endothelial function assessed by a noninvasive laser Doppler flowmetry method in Japanese young healthy subjects.

4.1. Pressor effect of caffeine

In the present study, the plasma caffeine concentration after caffeinated coffee intake attained 1.6 μg/ml. This concentration of caffeine has been shown to act as an antagonist of adenosine A_1/A_{2A} receptors (19, 20). As adenosine causes vasodilation in most vascular beds (21), caffeine would induce an increase in vascular resistance. Thus, slight but significant rises in blood pressure observed after caffeinated coffee intake in the present study may, in part, be caused by an increase in basal vascular tone derived from the adenosine antagonism of caffeine, as found by an early study (22). In addition, a direct stimulatory effect of caffeine on myocardial contractility (23) might be involved in a significant increase in blood pressure seen after caffeinated coffee intake.

4.2. Effect of caffeine on microvascular function

The present finding that caffeine ingestion, even at a small dose (54.5 mg = less than 1 mg/kg), improves microvascular endothelial function is consistent with a previous study (24) using venous occlusion plethysmography demonstrating that the acute administration of caffeine at an extremely large dose (300 mg) augments vasodilator responses of forearm vessels to intra-arterial infusion of the endothelium-dependent agonist acetylcholine.

In contrast to our study, however, two previous reports using ultrasound-based measurement of brachial artery diameter during post-occlusive reactive hyperemia demonstrated that caffeinated coffee ingestion impaired endothelial function in healthy volunteers (9, 12). In addition, two other studies showed that acutely administered caffeine had no effect on endothelial function assessed by the brachial artery vasoreactivity measurement (10, 11). Although the reason for conflicting with our data cannot be fully explained at present, it seems plausible that the difference in the type of vessels used for assessing vascular function was mainly involved. Laser Doppler flowmetry employed in the present study measures microvascular function in cutaneous arterioles and capillaries, whereas the ultrasound-based measurement of brachial artery diameter reflects 'macrovascular' function in large conduit

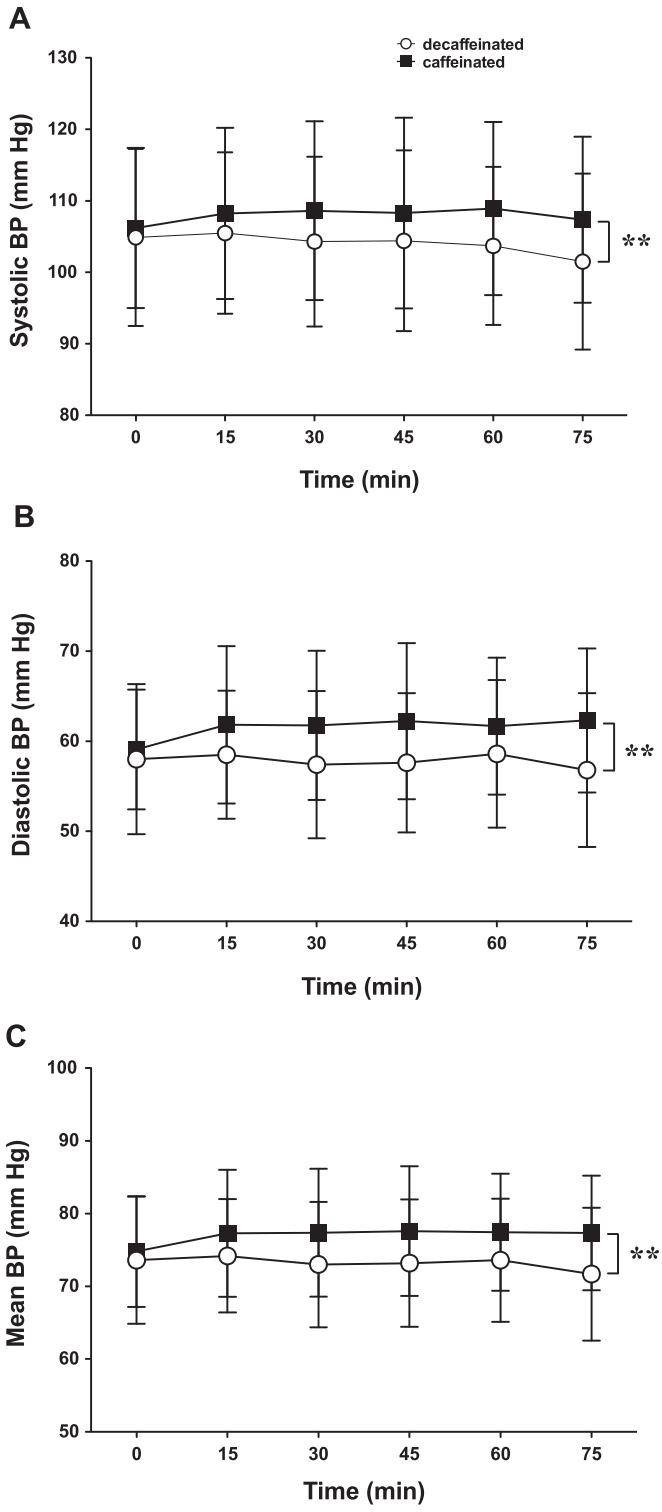

Fig. 2. Effects of caffeinated and decaffeinated coffee intake on systolic (A), diastolic (B) and mean (C) blood pressures (BP). Data are expressed as mean ± SD. $^{**}P < 0.01$ between caffeine (−) and caffeine (+) by ANOVA.

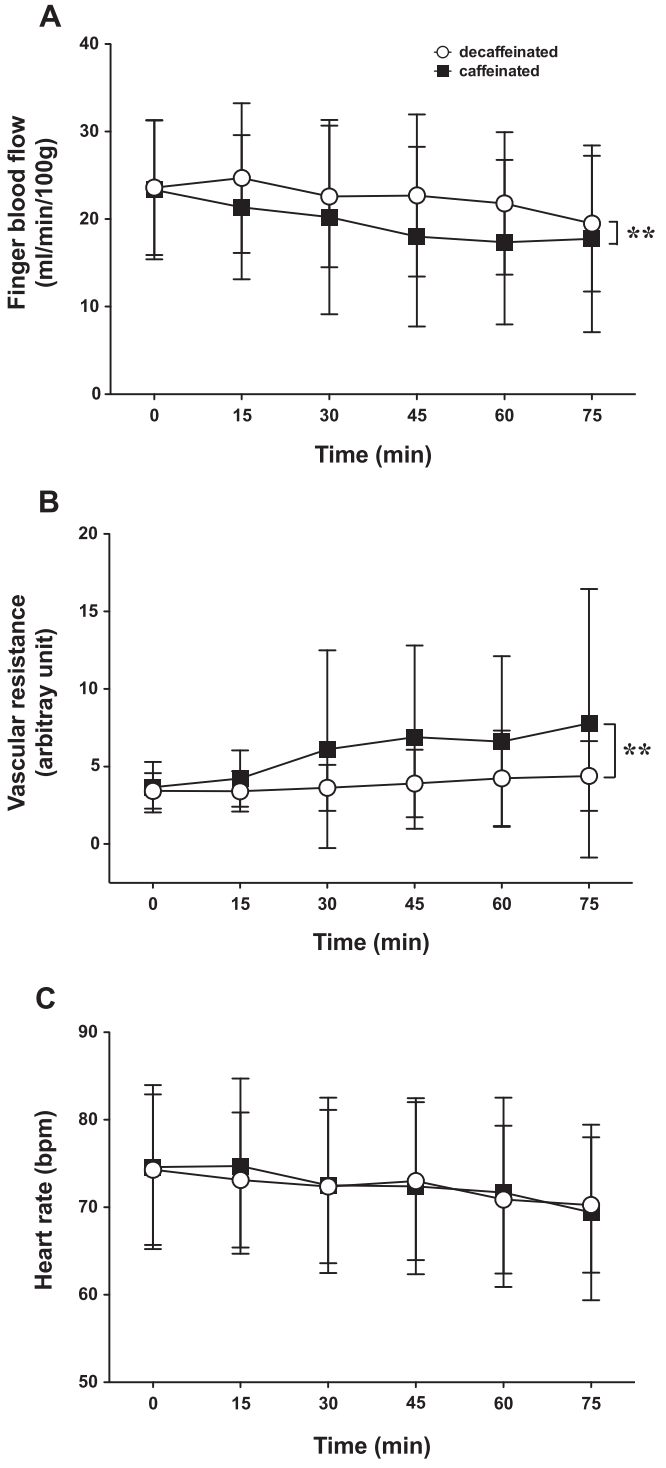

Fig. 3. Effects of caffeinated and decaffeinated coffee intake on finger blood flow (A), vascular resistance of the finger vascular bed (B), and heart rate (C). Data are expressed as mean ± SD. $^{**}P < 0.01$ between caffeine (−) and caffeine (+) by ANOVA.

arteries. Indeed, some previous studies have described that brachial artery responses to reactive hyperemia do not correlate with microvascular function as measured by agonist infusion studies or laser Doppler flowmetry (25, 26). It is generally considered that flow-dependent dilation of conduit arteries is mediated primarily by nitric oxide (14). By contrast, contribution of nitric oxide to post-occlusive reactive hyperemia in microvessels appears minimal (27, 28). Instead, EDHF may have a major role in the reactive hyperemic response in the microcirculation (15). Although the nature and mechanisms of EDHF remain uncertain, EDHF response has been proposed to be divided into two broad categories as follows: the first (classical) EDHF pathway is associated with endothelial cell hyperpolarization due to the opening of endothelial calcium-

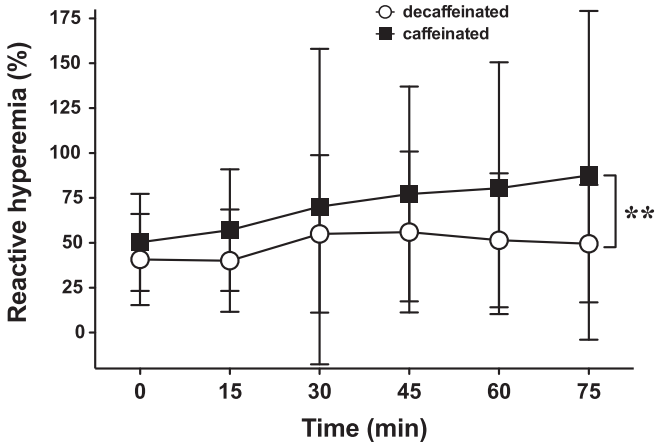

Fig. 4. Effect of caffeinated and decaffeinated coffee intake on post-occlusive reactive hyperemia of finger blood flow. Reactive hyperemia was calculated according to the following equation: reactive hyperemia (%) = [(peak hyperemic flow − resting flow)/resting flow] × 100. Data are expressed as mean ± SD. $^{**}P < 0.01$ between caffeine (−) and caffeine (+) by ANOVA.

activated K^+-channels, and the second EDHF pathway does not require endothelial hyperpolarization but involves the endothelial release of factors that hyperpolarize vascular smooth muscle cells by opening various myocyte K^+-channels such as calcium-activated K^+-channels (29). Experimental studies with animal and human vessels have demonstrated that the activation of vascular smooth muscle Ca^{2+}-activated K^+ channels probably contributes to the EDHF component of reactive hyperemia in microvessels (30, 31). Thus, microvascular endothelial function assessed by laser Doppler flowmetry may reflect the bioavailability of endothelium-dependent hyperpolarization via the activation of Ca^{2+}-activated K^+ channels in the endothelium and/or vascular smooth muscles.

4.3. Possible mechanisms involved in the beneficial effect of caffeine on microvascular function

In addition to the action on adenosine receptors, caffeine has been known to have a variety of pharmacological properties, including inhibition of phosphodiesterase (32), and calcium release from intracellular calcium stores via ryanodine-sensitive calcium channels (33). Interestingly, several electrophysiological experiments have displayed that caffeine at concentrations ranging from 10^{-6} to 10^{-3} M evokes calcium-dependent hyperpolarization in endothelial cells and vascular smooth muscle cells as a result of increased outward K^+ current (34–36). These data suggest that caffeine-induced release of calcium from intracellular calcium stores elicits the activation of calcium-activated K^+-channels in these cells. Considering that EDHF, unlike nitric oxide, has a major role in microvascular reactive hyperemia, it is possible that caffeine has the potential to augment the reactive hyperemic response of microvessels through amplifying hyperpolarization caused by EDHF. This may explain a favorable effect of caffeine on microvascular endothelial function in the present study, because the plasma concentration of caffeine was estimated to be nearly 10^{-5} M (Fig. 1B). It is intriguing that previous experiments in rats have shown that treatment with blockers of calcium-activated K^+-channels dose not affect baseline blood pressure or vascular conductance but attenuates vasodilator responses of resistance vessels produced by endothelium-dependent vasodilators such as acetylcholine (37, 38). These findings indicate that calcium-activated K^+-channels contribute little to the regulation of basal blood pressure but participate in responses to endothelial stimulation, and may be related to the present results that caffeine intake produced enhancement of microvascular endothelial function in spite of the occurrence of a slight increase in baseline blood pressure.

Several clinical studies (13, 39–41) have shown that caffeine exerts acute beneficial metabolic effects such as increased concentrations of adiponectin, a marker of anti-inflammatory and insulin-sensitizing effects (42). In addition, a cross-sectional study has reported that coffee consumption is inversely associated with a plasma marker of inflammation (C-reactive protein) and that of endothelial dysfunction (E-selectin) (43). Thus, these preferable properties of caffeine, besides the effect on endothelial function, may partly account for the beneficial cardiovascular effect of long-term coffee consumption.

4.4. Study limitations

Our study has some potential limitations to be considered. First, the number of subjects examined in this study may have been so small as to provide conclusive proof, although statistically significant effects were found. Second, the long-term effects of caffeine ingestion on endothelial function remain unknown. Third, we did not ask female subjects about the menstrual cycle, and it is thus unknown to what extent its phases affected the finger blood flow response. Finally, assessment of microvascular function was performed solely in Japanese healthy young volunteers. We have not yet elucidated whether or not caffeinated coffee intake ameliorates microvascular endothelial function not only in healthy subjects but also in patients with cardiovascular disease. These issues remain to be examined in future studies.

5. Conclusion

Our double-blind, placebo-controlled, crossover study has demonstrated, for the first time, that caffeine at the amount contained in a cup of coffee may cause improvement of microvascular endothelial function in healthy subjects.

Conflict of interest

None.

Acknowledgments

This work was supported in part by the All Japan Coffee Association and the Special Account Budget for Education and Research grated by the Japan Ministry of Education.

References

(1) Bonita JS, Mandarano M, Shuta D, Vinson J. Coffee and cardiovascular disease: in vitro, cellular, animal, and human studies. Pharmacol Res. 2007;55:187–198.
(2) Cornelis MC, El-Sohemy A. Coffee, caffeine, and coronary heart disease. Curr Opin Lipidol. 2007;18:13–19.
(3) Riksen NP, Rongen GA, Smits P. Acute and long-term cardiovascular effects of coffee: implications for coronary heart disease. Pharmacol Ther. 2009;121:185–191.
(4) Di Castelnuovo A, di Giuseppe R, Iacoviello L, de Gaetano G. Consumption of cocoa, tea and coffee and risk of cardiovascular disease. Eur J Intern Med. 2012;23:15–25.
(5) Freedman ND, Park Y, Abnet CC, Hollenbeck AR, Sinha R. Association of coffee drinking with total and cause-specific mortality. N Engl J Med. 2012;366:1891–1904.
(6) Malerba S, Turati F, Galeone C, Pelucchi C, Verga F, La Vecchia C, et al. A meta-analysis of prospective studies of coffee consumption and mortality for all causes, cancers and cardiovascular diseases. Eur J Epidemiol. 2013;28:527–539.

(7) Perticone F, Ceravolo R, Pujia A, Ventura G, Iacopino S, Scozzafava A, et al. Prognostic significance of endothelial dysfunction in hypertensive patients. Circulation. 2001;104:191–196.
(8) Widlansky ME, Gokce N, Keaney Jr JF, Vita JA. The clinical implications of endothelial dysfunction. J Am Coll Cardiol. 2003;42:1149–1160.
(9) Papamichael CM, Aznaouridis KA, Karatzis EN, Karatzi KN, Stamatelopoulos KS, Vamvakou G, et al. Effect of coffee on endothelial function in healthy subjects: the role of caffeine. Clin Sci (Lond). 2005;109:55–60.
(10) Duffy SJ, Keaney Jr JF, Holbrook M, Gokce N, Swerdloff PL, Frei B, et al. Short- and long-term black tea consumption reverses endothelial dysfunction in patients with coronary artery disease. Circulation. 2001;104:151–156.
(11) Alexopoulos N, Vlachopoulos C, Aznaouridis K, Baou K, Vasiliadou C, Pietri P, et al. The acute effect of green tea consumption on endothelial function in healthy individuals. Eur J Cardiovasc Prev Rehabil. 2008;15:300–305.
(12) Buscemi S, Verga S, Batsis JA, Donatelli M, Tranchina MR, Belmonte S, et al. Acute effects of coffee on endothelial function in healthy subjects. Eur J Clin Nutr. 2010;64:483–489.
(13) Shechter M, Shalmon G, Scheinowitz M, Koren-Morag N, Feinberg MS, Harats D, et al. Impact of acute caffeine ingestion on endothelial function in subjects with and without coronary artery disease. Am J Cardiol. 2011;107:1255–1261.
(14) Joannides R, Haefeli WE, Linder L, Richard V, Bakkali EH, Thuillez C, et al. Nitric oxide is responsible for flow-dependent dilatation of human peripheral conduit arteries in vivo. Circulation. 1995;91:1314–1319.
(15) Lorenzo S, Minson CT. Human cutaneous reactive hyperaemia: role of BK_{Ca} channels and sensory nerves. J Physiol. 2007;585:295–303.
(16) Bonner R, Nossal R. Model for laser Doppler measurements of blood flow in tissue. Appl Opt. 1981;20:2097–2107.
(17) Schreiber-Deturmeny E, Bruguerolle B. Simultaneous high-performance liquid chromatographic determination of caffeine and theophylline for routine drug monitoring in human plasma. J Chromatogr B, Biomed Appl. 1996;677:305–312.
(18) Roustit M, Blaise S, Millet C, Cracowski JL. Reproducibility and methodological issues of skin post-occlusive and thermal hyperemia assessed by single-point laser Doppler flowmetry. Microvasc Res. 2010;79:102–108.
(19) Snyder SH, Katims JJ, Annau Z, Bruns RF, Daly JW. Adenosine receptors and behavioral actions of methylxanthines. Proc Natl Acad Sci U S A. 1981;78:3260–3264.
(20) Fredholm BB, Battig K, Holmen J, Nehlig A, Zvartau EE. Actions of caffeine in the brain with special reference to factors that contribute to its widespread use. Pharmacol Rev. 1999;51:83–133.
(21) Rongen GA, Floras JS, Lenders JW, Thien T, Smits P. Cardiovascular pharmacology of purines. Clin Sci (Lond). 1997;92:13–24.
(22) Smits P, Boekema P, De Abreu R, Thien T, van 't Laar A. Evidence for an antagonism between caffeine and adenosine in the human cardiovascular system. J Cardiovasc Pharmacol. 1987;10:136–143.
(23) Riksen NP, Smits P, Rongen GA. The cardiovascular effects of methylxanthines. Handb Exp Pharmacol. 2011;200:413–437.
(24) Umemura T, Ueda K, Nishioka K, Hidaka T, Takemoto H, Nakamura S, et al. Effects of acute administration of caffeine on vascular function. Am J Cardiol. 2006;98:1538–1541.
(25) Shamim-Uzzaman QA, Pfenninger D, Kehrer C, Chakrabarti A, Kacirotti N, Rubenfire M, et al. Altered cutaneous microvascular responses to reactive hyperaemia in coronary artery disease: a comparative study with conduit vessel responses. Clin Sci (Lond). 2002;103:267–273.
(26) Eskurza I, Seals DR, DeSouza CA, Tanaka H. Pharmacologic versus flow-mediated assessments of peripheral vascular endothelial vasodilatory function in humans. Am J Cardiol. 2001;88:1067–1069.
(27) Wong BJ, Wilkins BW, Holowatz LA, Minson CT. Nitric oxide synthase inhibition does not alter the reactive hyperemic response in the cutaneous circulation. J Appl Physiol. 2003;95:504–510.
(28) Zhao JL, Pergola PE, Roman LJ, Kellogg Jr DL. Bioactive nitric oxide concentration does not increase during reactive hyperemia in human skin. J Appl Physiol. 2004;96:628–632.
(29) Edwards G, Feletou M, Weston AH. Endothelium-derived hyperpolarising factors and associated pathways: a synopsis. Pflugers Arch. 2010;459:863–879.
(30) Huang A, Sun D, Jacobson A, Carroll MA, Falck JR, Kaley G. Epoxyeicosatrienoic acids are released to mediate shear stress-dependent hyperpolarization of arteriolar smooth muscle. Circ Res. 2005;96:376–383.
(31) Liu Y, Bubolz AH, Mendoza S, Zhang DX, Gutterman DD. H_2O_2 is the transferrable factor mediating flow-induced dilation in human coronary arterioles. Circ Res. 2011;108:566–573.
(32) Butcher RW, Sutherland EW. Adenosine 3′,5′-phosphate in biological materials. I. Purification and properties of cyclic 3′,5′-nucleotide phosphodiesterase and use of this enzyme to characterize adenosine 3′,5′-phosphate in human urine. J Biol Chem. 1962;237:1244–1250.
(33) Endo M. Calcium release from the sarcoplasmic reticulum. Physiol Rev. 1977;57:71–108.
(34) Fujii K, Miyahara H, Suzuki H. Comparison of the effects of caffeine and procaine on noradrenergic transmission in the guinea-pig mesenteric artery. Br J Pharmacol. 1985;84:675–684.
(35) Chen GF, Suzuki H. Calcium dependency of the endothelium-dependent hyperpolarization in smooth muscle cells of the rabbit carotid artery. J Physiol. 1990;421:521–534.
(36) Rusko J, Van Slooten G, Adams DJ. Caffeine-evoked, calcium-sensitive membrane currents in rabbit aortic endothelial cells. Br J Pharmacol. 1995;115:133–141.
(37) Shinde UA, Desai KM, Yu C, Gopalakrishnan V. Nitric oxide synthase inhibition exaggerates the hypotensive response to ghrelin: role of calcium-activated potassium channels. J Hypertens. 2005;23:779–784.
(38) Parkington HC, Chow JA, Evans RG, Coleman HA, Tare M. Role for endothelium-derived hyperpolarizing factor in vascular tone in rat mesenteric and hindlimb circulations *in vivo*. J Physiol. 2002;542:929–937.
(39) Kempf K, Herder C, Erlund I, Kolb H, Martin S, Carstensen M, et al. Effects of coffee consumption on subclinical inflammation and other risk factors for type 2 diabetes: a clinical trial. Am J Clin Nutr. 2010;91:950–957.
(40) Wedick NM, Brennan AM, Sun Q, Hu FB, Mantzoros CS, van Dam RM. Effects of caffeinated and decaffeinated coffee on biological risk factors for type 2 diabetes: a randomized controlled trial. Nutr J. 2011;10:93–101.
(41) Yamashita K, Yatsuya H, Muramatsu T, Toyoshima H, Murohara T, Tamakoshi K. Association of coffee consumption with serum adiponectin, leptin, inflammation and metabolic markers in Japanese workers: a cross-sectional study. Nutr Diabetes. 2012;2:e33–e38.
(42) Li S, Shin HJ, Ding EL, van Dam RM. Adiponectin levels and risk of type 2 diabetes: a systematic review and meta-analysis. JAMA. 2009;302:179–188.
(43) Lopez-Garcia E, van Dam RM, Qi L, Hu FB. Coffee consumption and markers of inflammation and endothelial dysfunction in healthy and diabetic women. Am J Clin Nutr. 2006;84:888–893.

γ-Oryzanol Protects Pancreatic β-Cells Against Endoplasmic Reticulum Stress in Male Mice

Chisayo Kozuka, Sumito Sunagawa, Rei Ueda, Moritake Higa, Hideaki Tanaka, Chigusa Shimizu-Okabe, Shogo Ishiuchi, Chitoshi Takayama, Masayuki Matsushita, Masato Tsutsui, Jun-ichi Miyazaki, Seiichi Oyadomari, Michio Shimabukuro, and Hiroaki Masuzaki

Division of Endocrinology, Diabetes and Metabolism, Hematology, Rheumatology (Second Department of Internal Medicine) (C.K., S.S., R.U., M.H., H.T., M.S., H.M.), Graduate School of Medicine, University of the Ryukyus, Okinawa 903-0215, Japan; The Diabetes and Life-Style Related Disease Center (M.H.), Tomishiro Central Hospital, Okinawa 901-0243, Japan; Tanaka Clinic (H.T.), Okinawa 901-0244, Japan; Department of Molecular Anatomy (C.S.-O., C.T.), Graduate School of Medicine, University of the Ryukyus, Okinawa 903-0215, Japan; Department of Neurosurgery (S.I.), Graduate School of Medicine, University of the Ryukyus, Okinawa 903-0215, Japan; Department of Molecular and Cellular Physiology (M.M.), Graduate School of Medicine, University of the Ryukyus, Okinawa 903-0215, Japan; Department of Pharmacology (M.T.), Graduate School of Medicine, University of the Ryukyus, Okinawa 903-0215, Japan; Division of Stem Cell Regulation Research (J.-i.M.), Osaka University Graduate School of Medicine, Osaka 565-0871, Japan; Institute for Genome Research (S.O.), University of Tokushima, Tokushima 770-8506, Japan; and Department of Cardio-Diabetes Medicine (M.S.), University of Tokushima Graduate School of Health Biosciences, Tokushima 770-8503, Japan

Endoplasmic reticulum (ER) stress is profoundly involved in dysfunction of β-cells under high-fat diet and hyperglycemia. Our recent study in mice showed that γ-oryzanol, a unique component of brown rice, acts as a chemical chaperone in the hypothalamus and improves feeding behavior and diet-induced dysmetabolism. However, the entire mechanism whereby γ-oryzanol improves glucose metabolism throughout the body still remains unclear. In this context, we tested whether γ-oryzanol reduces ER stress and improves function and survival of pancreatic β-cells using murine β-cell line MIN6. In MIN6 cells with augmented ER stress by tunicamycin, γ-oryzanol decreased exaggerated expression of ER stress-related genes and phosphorylation of eukaryotic initiation factor-2α, resulting in restoration of glucose-stimulated insulin secretion and prevention of apoptosis. In islets from high-fat diet-fed diabetic mice, oral administration of γ-oryzanol improved glucose-stimulated insulin secretion on following reduction of exaggerated ER stress and apoptosis. Furthermore, we examined the impact of γ-oryzanol on low-dose streptozotocin-induced diabetic mice, where exaggerated ER stress and resultant apoptosis in β-cells were observed. Also in this model, γ-oryzanol attenuated mRNA level of genes involved in ER stress and apoptotic signaling in islets, leading to amelioration of glucose dysmetabolism. Taken together, our findings demonstrate that γ-oryzanol directly ameliorates ER stress-induced β-cell dysfunction and subsequent apoptosis, highlighting usefulness of γ-oryzanol for the treatment of diabetes mellitus. **(*Endocrinology* 156: 1242–1250, 2015)**

ISSN Print 0013-7227 ISSN Online 1945-7170
Printed in U.S.A.

Received September 9, 2014. Accepted January 9, 2015.
First Published Online January 16, 2015

Abbreviations: *Bcl2*, B cell leukemia/lymphoma 2; CAD, caspase-activated DNase; *Casp3*, caspase-3; *Cdkn1a*, cyclin-dependent kinase inhibitor 1A; Chop, CCAAT/enhancer-binding protein-homologous protein; eIF2α, eukaryotic initiation factor-2α; ER, endoplasmic reticulum; ERdj4, ER resident DNAJ 4; GLP-1, glucagon-like peptide-1; GSIS, glucose-stimulated insulin secretion; HFD, high-fat diet; IHC, immunohistochemical; 4-PBA, 4-phenylbutyrate; PCNA, proliferating cell nuclear antigen; PI, propidium iodide; PKA, protein kinase A; *Rn18s*, 18S rRNA; STZ, streptozotocin; *Xbp1s*, spliced form of X box binding protein 1.

γ-Oryzanol is a unique bioactive substance exclusively and abundantly found in brown rice (1), comprising of a mixture of ferulic acid esters with phytosterols or triterpene alcohols (2). We recently reported that γ-oryzanol decreases endoplasmic reticulum (ER) stress in hypothalamus and attenuates the preference for dietary fat, thereby ameliorating high-fat diet (HFD)-induced obesity in mice (3). In accordance with this finding, our recent clinical studies highlight metabolically beneficial impact of brown rice on prediabetic obese humans (4). However, the entire mechanism whereby brown rice prevents type 2 diabetes still remains obscure.

In subjects with type 2 diabetes, exaggerated ER stress in pancreatic islets is linked to progressive β-cell dysfunction and resultant apoptosis (5). Recent studies clarified the importance of IL-1β and nucleotide-binding oligomeraization domein like receptor family, pyrin domain-containing 3 inflammasome in ER stress-induced apoptosis in β-cell (6, 7). In response to unfolded proteins, 3 kinds of ER transmembrane proteins, including protein kinase R-like ER kinase, activating transcription factor-6, and inositol-requiring enzyme-1, are initially activated (8). Besides inositol-requiring enzyme-1α, protein kinase R-like ER kinase/eukaryotic initiation factor-2α (eIF2α) signaling strongly augments active form of IL-1β via activation of nucleotide-binding oligomeraization domein like receptor family, pyrin domain-containing 3 inflammasome, and expression level of *Il1b*, leading to apoptosis (7). Of note, an antidiabetic incretin hormone, glucagon-like peptide-1 (GLP-1) protects β-cells against ER stress-induced apoptosis via the cAMP/protein kinase A (PKA) pathway (9). These findings led us to hypothesize that γ-oryzanol would protect β-cells against ER stress-induced apoptosis. Notably, exendin-4, a long-acting GLP-1 agonist, also ameliorates glucose intolerance in diabetic rats via the proliferation of β-cells (10). In this context, using murine pancreatic β-cell line MIN6 (11) as well as HFD- or streptozotocin (STZ)-induced diabetic murine models, we tested whether γ-oryzanol would improve dysfunction of pancreatic islets through reduction of ER stress and enhancement of β-cell proliferation.

Materials and Methods

Animals

Eight-week-old male C57BL/6J mice obtained from Charles River Laboratories Japan, Inc were housed at 24°C under a 12-hour light, 12-hour dark cycle. The mice were allowed free access to food and water. Body weights were measured weekly. All animal experiments were approved by the Animal Experiment Ethics Committee of the University of the Ryukyus (No. 5352, 5718).

Administration of γ-oryzanol

γ-Oryzanol (Wako Pure Chemical Industries, Ltd) was orally administrated as described (3). Briefly, γ-oryzanol was dissolved in 0.5% methyl cellulose solution. γ-oryzanol (20, 80, or 320 μg/g body weight) was delivered into the stomach by a gavage needle every day during feeding with a HFD (Western Diet; Research Diets, Inc) for 13 weeks. For perform immunohistochemical (IHC) analyses, mice were treated for 6 months. The doses of γ-oryzanol used were as described (3).

Metabolic parameters

Blood samples were taken from the retro-orbital venous plexuses. Plasma insulin and proinsulin levels were measured using ELISA kits (Shibayagi Co, Ltd and Morinaga Institute of Biological Science, Inc). For oral glucose tolerance tests, the mice were orally administrated with 2.0 g/kg body weight glucose after an 18-hour fast. Blood glucose levels were measured at the indicated times.

Treatment of STZ

To create a model of augmented ER stress in pancreatic β-cells (12, 13), mice were single injected with low-dose STZ (100 μg/g body weight ip; Sigma-Aldrich) after 4 hours of fasting. γ-Oryzanol (320 μg/g body weight^{-1} d^{-1}) was orally administrated daily for 14 days 1 day before the treatment of STZ.

Assessment of tissue distribution of γ-oryzanol

At 1 hour after the single oral administration of γ-oryzanol (3.2 mg/g body weight), tissues were sampled, and their total lipids were extracted according to the procedure of Folch and Lebaron (14). Tissue contents of γ-oryzanol were quantified by HPLC (LC-20AT, SPD-20AV; Shimadzu) with UV detection at 315 nm using XBridge C18 column (particle size 5 μm; Waters).

Isolation of pancreatic islets and assessment of insulin secretion

Pancreatic islets were isolated from mice by collagenase digestion (Liberase TL; Roche Diagnostics GmbH) and purified on a Histopaque gradient (Histopaque 1077; Sigma-Aldrich) as described (15). Amount of insulin secretion from MIN6 cells, a representative murine pancreatic β-cell line (11), were seeded at a density of 2.0×10^5 cells/mL on 24-well plates. After 48 hours of culture, the cells were incubated with Krebs-Ringer bicarbonate buffer containing 2.5mM glucose for 2 hours, subsequently incubated in Krebs-Ringer bicarbonate buffer with or without γ-oryzanol (0.2, 2, or 10 μg/mL) for 1 hour. Insulin secretion was normalized by cellular protein content.

Assessment of cell viability and apoptosis

MIN6 cells were treated with tunicamycin and γ-oryzanol for 24 hours. Cell viability was evaluated by a colorimetric procedure with Cell Count Reagent SF (Nacalai Tesque, Inc). To assess the extent of apoptosis, cells were stained with Hoechst 33342 and propidium iodide (PI). Morphological changes of the nuclei were observed under a fluorescence microscope. Caspase-3 activity was determined by Caspase-Glo 3/7 Assay (Promega) at 24 hours after the treatment.

Luciferase reporter assay

The potential chaperone activity of ferulic acid was investigated as described (3).

Western blotting

Western blotting was performed as described (16) with antibodies against eIF2α and phospho-eIF2α (9722 and 9721; Cell Signaling Technology) (17) (see Table 1). Protein extracted from MIN6 cells treated with or without tunicamycin were used a positive or negative control, respectively.

Quantitative real-time PCR

Total RNA was extracted using TRIzol reagent (Invitrogen) and cDNA was synthesized using an iScript cDNA Synthesis kit (Bio-Rad). Quantitative real-time PCR was performed using a StepOnePlus Real-Time PCR System, Fast SYBR Green Master Mix and TaqMan Fast Advanced Master Mix (Applied Biosystems). The mRNA levels were normalized by 18S rRNA (*Rn18s*). Primers used were summarized in Supplemental Table 1.

IHC analyses

The dissected pancreas was fixed in 4% paraformaldehyde, embedded in paraffin, and sectioned. The sections were immunostained for insulin (N1542; Dako Japan), phospho-eIF2α, cleaved caspase-3 (9661; Cell Signaling Technology), and proliferating cell nuclear antigen (PCNA) (13110; Cell Signaling Technology) (18) (see Table 1). The ratios of insulin-positive and cleaved caspase-3-positive area to the total islet area were calculated based on more than 65 islets per group using Photoshop (Adobe).

Statistical analysis

Data are expressed as the mean ± SEM. One-way ANOVA, repeated-measures ANOVA, and repeated-measures ANOVA followed by multiple comparison tests (Bonferroni/Dunn method) were used where applicable. Student's *t* test was used to analyze the differences between 2 groups. Differences were considered significant at $P < .05$.

Results

Tissue distribution of γ-oryzanol after oral administration in mice

Based on a previous report showing that orally administrated γ-oryzanol was rapidly absorbed from the intestine and reached a maximum plasma concentration in less than or equal to 1 hour (2), tissue contents of γ-oryzanol were assessed at 1 hour after single oral administration of γ-oryzanol (3.2 mg/g body weight). As reported (2), γ-oryzanol was distributed dominantly in the brain, whereas γ-oryzanol was also accumulated considerably in pancreas comparable with kidney and adipose tissue (Figure 1A). On the other hand, little accumulation of γ-oryzanol was observed in liver (Figure 1A). Considering that metabolites of γ-oryzanol were distributed mainly in liver (2), it is likely that γ-oryzanol is metabolized by liver.

γ-Oryzanol ameliorates ER stress-induced β-cell dysfunction both in vitro and in vivo

To examine the possible effect of γ-oryzanol on ER stress in β-cells, we assessed the expression levels of ER stress-responsive genes, including *Ddit3* (CCAAT/enhancer-binding protein-homologous protein [Chop]), *Dnajb9* (ER resident DNAJ 4 [ERdj4]), and spliced form of X box binding protein 1 (*Xbp1s*). In islets, mRNAs of ER stress-responsive genes were substantially increased after 13 weeks of HFD feeding (Figure 1B). Noticeably, oral administration of γ-oryzanol significantly decreased the expression levels of ER stress-responsive genes in islets from HFD-fed mice (Figure 1B). Also in MIN6 cells, increment of expression of these genes induced by tunicamycin was reversed by the supplementation of γ-oryzanol (Figure 1C). Similarly, phosphorylation of eIF2α in response to ER stress was markedly reduced by γ-oryzanol in pancreatic β-cells both in vivo (Figure 1D) and in vitro (Figure 1E). γ-Oryzanol also decreased mRNA level of *Il1b* in islets from HFD-fed mice and tunicamycin-treated MIN6 cells (Figure 1, B and C). As reported (19), glucose-stimulated insulin secretion (GSIS) was significantly decreased in MIN6 cells treated with tunicamycin (Figure 1F). In contrast, both γ-oryzanol and 4-phenylbutyrate (4-PBA), a potent chemical chaperone, restored GSIS even in tunicamycin-treated cells (Figure 1F).

In addition, to explore whether ferulic acid, a partial structure of γ-oryzanol, would also decrease ER stress, we examined its possible effect on the activities of reporter

Table 1. Antibodies Used for Western Blots and IHC Analyses

Peptide/ Protein Target	Antigen Sequence (If Known)	Name of Antibody	Manufacturer, Catalog Number, and/or Name of Individual Providing the Antibody	Species Raised in; Monoclonal or Polyclonal	Dilution Used
Insulin		Guinea pig antiinsulin	Dako Japan, N1542	Guinea pig polyclonal	1:3 (IHC)
eIF2α		eIF2α Antibody	Cell Signaling Technology, 9722	Rabbit polyclonal	1:500 (WB)
Phospho-eIF2α (Ser51)		Phospho-eIF2α (Ser51) antibody	Cell Signaling Technology, 9721	Rabbit polyclonal	1:500 (WB), 1:500 (IHC)
Cleaved caspase-3		Cleaved caspase-3 (Asp175) antibody	Cell Signaling Technology, 9661	Rabbit polyclonal	1:1000 (IHC)
PCNA		PCNA (D^3H8P) XP rabbit mAb	Cell Signaling Technology, 13110	Rabbit monoclonal	1:200 (IHC)

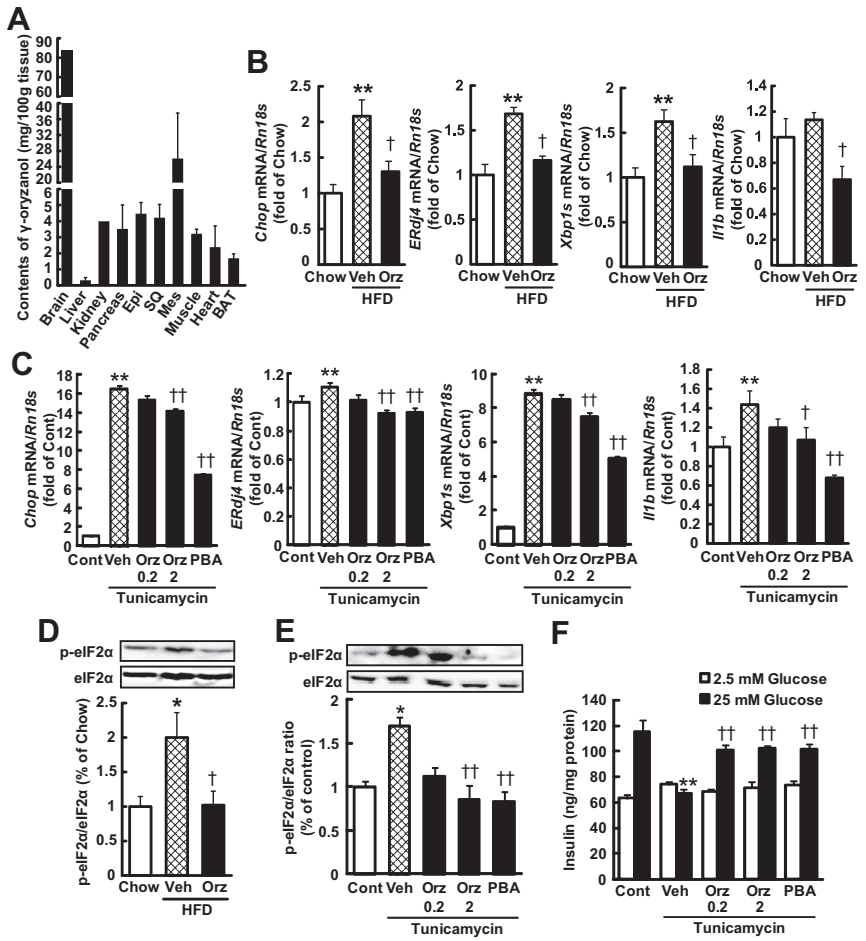

Figure 1. γ-Oryzanol (Orz) ameliorates ER stress-induced β-cell dysfunction. A, Tissue contents of Orz (mg/100 g tissue) were examined at 1 hour after single oral administration of Orz (3.2 mg/g body weight) in C57BL/6J mice (n = 10–70; 3 independent experiments). Epi, epididymal fat; SQ, sc fat; Mes, mesenteric fat; BAT, brown adipose tissue. HFD-fed mice were treated with Orz (320 μg/g body weight^{-1} d^{-1}) for 13 weeks, and pancreatic islets were isolated. MIN6 cells were treated with tunicamycin (0.5 μg/mL) and Orz (0.2 or 2 μg/mL) or 4-PBA (PBA) (5mM) for 24 hours. B and C, Expression levels of ER stress-responsive genes such as *Chop*, *ERdj4*, *Xbp1s*, and *Il1b* in pancreatic islets from HFD-fed mice (B) (n = 6) and tunicamycin-treated MIN6 cells (C) (n = 10). The levels were determined by real-time PCR and normalized by those of *Rn18s*. D and E, Phosphorylation (Ser51) of eIF2α (p-eIF2α) in pancreatic islets from HFD-fed mice (D) and tunicamycin-treated MIN6 cells (E) (n = 6). F, Effects of Orz on GSIS in tunicamycin-treated MIN6 cells. Data are expressed as mean ± SEM. *, $P < .05$; **, $P < .01$, vs chow-fed mice or control cells (Cont); †, $P < .05$; ††, $P < .01$, vs vehicle-treated HFD-fed mice or cells treated with tunicamycin and vehicle (Veh).

genes carrying ER stress-responsive *cis*-acting elements such as ER stress-responsive elements and unfolded protein response element upstream of the luciferase gene. Consequently, ferulic acid did not suppress the tunicamycin-induced activation of the *cis*-acting elements in luciferase reporter assays in human embryonic kidney 293 cells (Supplemental Figure 1), suggesting the importance of full-structure of γ-oryzanol as a chemical chaperone.

γ-Oryzanol ameliorates ER stress-induced apoptosis in β-cells

To further investigate whether γ-oryzanol prevents ER stress-induced apoptosis in β-cells, MIN6 cells were stained with Hoechst 33342 and PI. Although the number of apoptotic cells (PI-negative cells with chromatin condensation) was increased by replenishing tunicamycin, γ-oryzanol ameliorated the ER stress-induced apoptosis in tunicamycin-treated MIN6 cells (Figure 2, A and B). γ-Oryzanol also reduced the caspase-3 activity in tunicamycin-treated MIN6 cells (Figure 2C). To explore antiapoptotic potential of γ-oryzanol in vivo, expression levels of apoptosis-related genes, including caspase-3 (*Casp3*), B cell leukemia/lymphoma 2 (*Bcl2*), and *Dffb* (caspase-activated DNase [CAD]), were examined. In islets from HFD-fed mice, mRNA levels of apoptosis-related genes were substantially decreased by the treatment with γ-oryzanol (Figure 2D). Observed changes in mRNA levels were reproduced in tunicamycin-treated MIN6 cells (Supplemental Figure 2). IHC analyses also showed that positive cells for phospho-eIF2α (ER stress marker), cleaved caspase-3 (apoptosis marker), or PCNA (proliferative marker) were increased in HFD-fed mice, whereas the changes were restored by the treatment of γ-oryzanol (Figure 2, E and H). The quantification of cleaved caspase-3-positive area to total islet area as well as cleaved caspase-3-positive β-cell area to total β-cell area further reinforced the notion above (Figure 2, G and I). Moreover, γ-oryzanol augmented the intensity of insulin staining and increased the ratio of insulin-positive area to total islet area in mice on a HFD (Figure 2, E and F). In HFD-fed mice, γ-oryzanol dose dependently lowered plasma insulin level (vehicle, 511 ± 73 pg/mL; γ-oryzanol 20 μg/g body weight^{-1} d^{-1}, 358 ± 58 pg/mL; γ-oryzanol 80 μg/g body weight^{-1} d^{-1}, 351 ± 100 pg/mL; and γ-oryzanol 320 μg/g body weight^{-1} d^{-1}, 262 ± 34 pg/mL, 18-h fasting) and the proinsulin/insulin ratio, a marker of β-cell function (20) (Figure 2J), further supporting the notion that γ-oryzanol protects β-cells against ER stress in vivo.

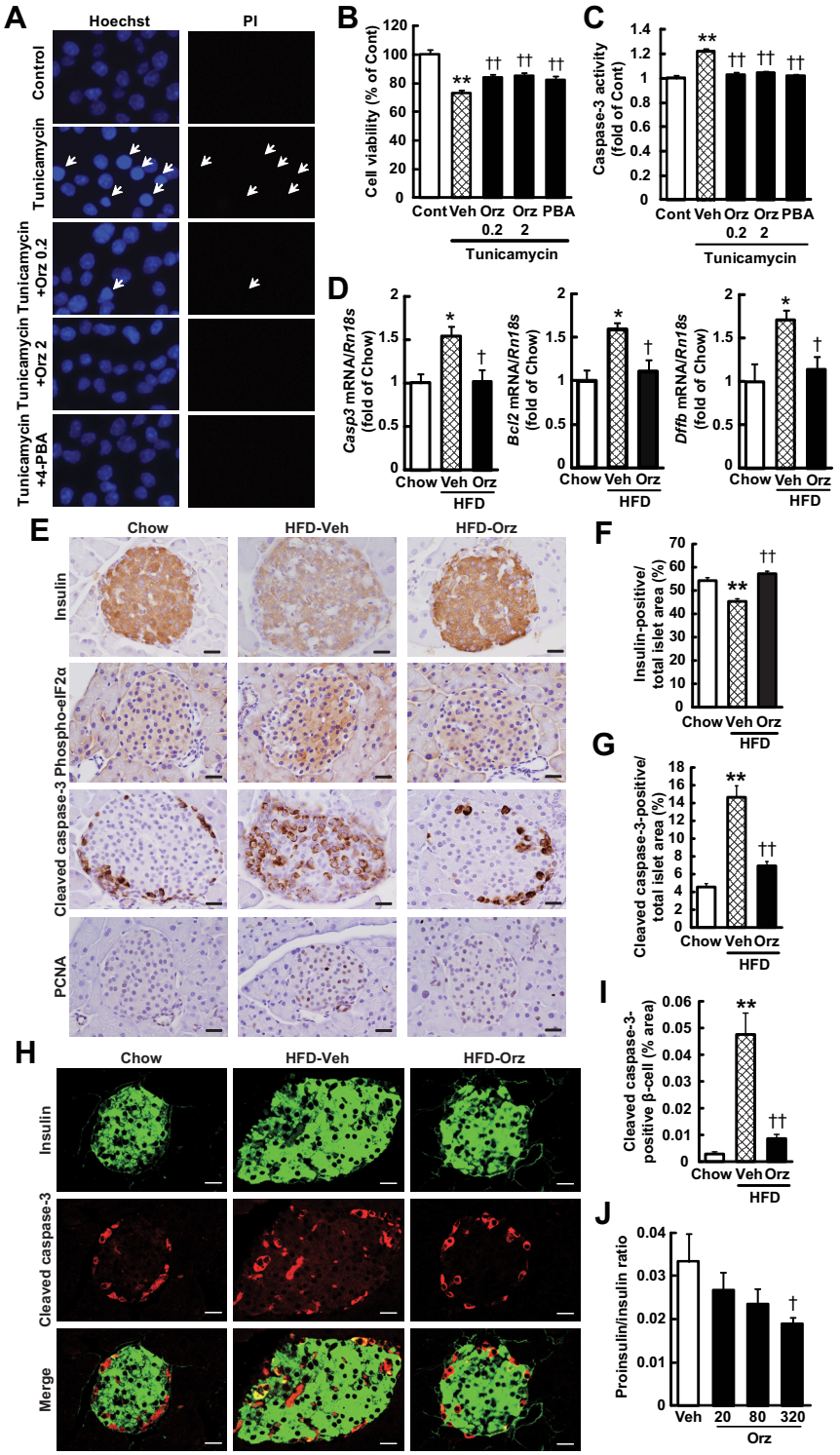

Figure 2. γ-Oryzanol (Orz) ameliorates ER stress-induced β-cell apoptosis. A–C, Effects of Orz (0.2 or 2 μg/mL) or 4-PBA (PBA) (5mM) on apoptotic nuclear morphological changes visualized by staining with Hoechst 33342 and PI (A), viability (B), and caspase-3 activity (C) in tunicamycin-treated MIN6 cells (n = 8–10). D, Expression levels of mRNA for *Casp3*, *Bcl2*, and CAD (*Dffb*) in pancreatic islets from Orz-treated HFD-fed mice (320 μg/g body weight^{-1} d^{-1}; n = 6). E, IHC analyses of isolated pancreatic islets from HFD-fed mice treated with Orz (320 μg/body weight^{-1} d^{-1}). Serial paraffin-embedded sections were stained with antiinsulin, antiphospho-eIF2α, anticleaved caspase-3, and anti-PCNA antibodies. Scale bar, 20 μm; magnification, ×400. F and G, The ratios of insulin-positive area (F) and cleaved caspase-3-positive area (G) to the total islet area were calculated (n = 3; 108–144 islets). Data are expressed as mean ± SEM. **, $P < .01$, vs chow-fed mice; ††, $P < .01$, vs HFD-fed mice treated with vehicle (Veh). H, Paraffin-embedded pancreatic sections were costained with antiinsulin (green) and anticleaved caspase-3 (red) antibodies. Scale bar, 20 μm; magnification, ×600. I, The ratio of cleaved caspase-3-positive β-cell area to total β-cell area was calculated (n = 3; 108–118 islets). J, Proinsulin/insulin ratio in Orz-treated HFD-fed mice (20, 80, or 320 μg/g body weight^{-1} d^{-1}; n = 6). Data are expressed as mean ± SEM. *, $P < .05$; **, $P < .01$, vs chow-fed mice or control cells (Cont); †, $P < .05$; ††, $P < .01$, vs vehicle-treated HFD-fed mice or cells treated with tunicamycin and vehicle (Veh).

γ-Oryzanol ameliorates β-cell dysfunction and apoptosis in STZ-treated mice

To endorse the protective effects of γ-oryzanol on β-cell in vivo, we administrated γ-oryzanol orally to low-dose STZ-induced diabetic mice. Treatment of low-dose STZ induces the partial destruction of pancreatic β-cell and insulinopenia (12), leading to exaggerated ER stress in β-cell by increased demand of insulin (21). In low-dose STZ-treated mice, fasting plasma insulin level was significantly decreased (Figure 3A), resulting in the elevation of fasting blood glucose levels (Figure 3B). In this model, γ-oryzanol significantly ameliorated glucose dysmetabolism (Figure 3, A–C) and augmented considerably plasma insulin levels (Figure 3A). IHC analyses by antibody against insulin revealed that insulin-positive β-cell area was considerably decreased in islets of STZ-treated mice, whereas the decrement was restored by γ-oryzanol (Figure 3, D and E). In islets of STZ-treated mice, intensity of phospho-eIF2α and cleaved caspase-3-positive cells were also increased, indicating that ER stress and resultant apoptosis were augmented by the treatment of STZ (Figure 3, D and G). The cleaved caspase-3-positice area to total islet area as well as cleaved caspase-3-positive β-cell area to total β-cell area further reinforced the notion above (Figure 3, F and H). Of note, phospho-eIF2α, cleaved caspase-3, and PCNA were colocalized in β-cells (Supplemental Figure 3). In this experimental setting, γ-oryzanol increased insulin-positive area and decreased the intensities of phospho-eIF2α and cleaved caspase-3-positive area in islets (Figure 3, D–H), whereas γ-oryzanol did not increase PCNA-positive proliferating cells (Figure 3D). Expression levels of genes involved in ER stress signaling and apoptosis were significantly decreased by γ-oryzanol in islets from STZ-treated mice (Figure 3I).

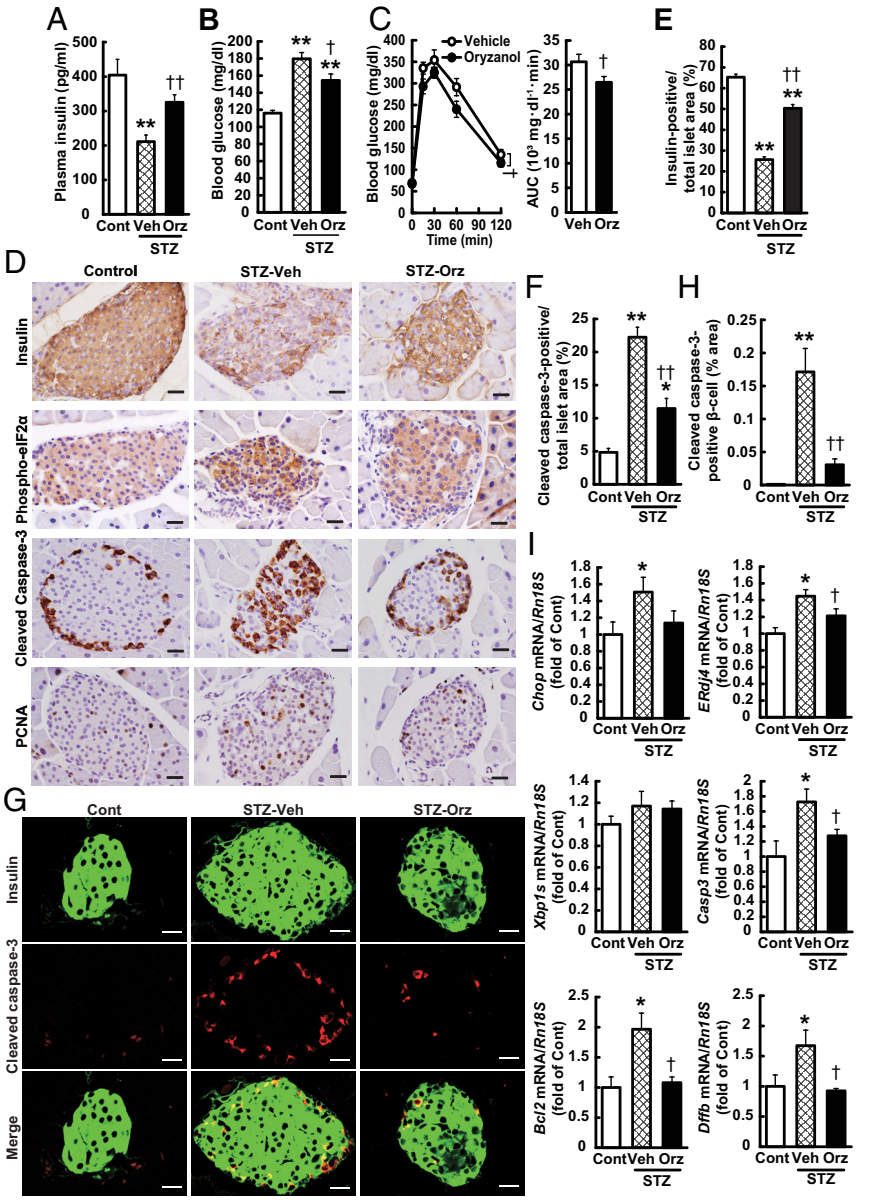

Figure 3. γ-Oryzanol ameliorates β-cell dysfunction and apoptosis in STZ-treated mice. A–C, Effects of γ-oryzanol (320 μg/g body weight^{-1} d^{-1}) on plasma insulin levels (A) (n = 7) and blood glucose levels (B) (n = 7) after a 4-h fasting were measured at 2 weeks after the STZ treatment. Blood glucose levels and the AUC of blood glucose during the oral glucose tolerance test (C) (n = 7). D, IHC analyses of pancreatic islets from STZ-treated mice treated with γ-oryzanol. Serial paraffin-embedded sections were stained with antiinsulin, antiphospho-eIF2α, cleaved caspase-3, PCNA antibodies. Scale bar, 20 μm; magnification, ×400. E and F, The ratios of insulin-positive area (E) and cleaved caspase-3-positive area (F) to the total islet area were calculated (n = 2; 84–111 islets). G, Paraffin-embedded pancreatic sections were costained with antiinsulin (green) and anticleaved caspase-3 (red) antibodies. Scale bar, 20 μm; magnification, ×600. (H) The ratio of cleaved caspase-3-positive β-cell area to total β-cell area was calculated (n = 2; 66–116 islets). (I) Expression levels of mRNA for *Chop*, *ERdj4*, *Xbp1s*, *Casp3*, *Bcl2*, and *Dffb* (CAD) in pancreatic islets from STZ-treated mice (n = 5). The mRNA levels were determined by real-time PCR and normalized by those of *Rn18s*. Data are expressed as mean ± SEM. *, $P < .05$; **, $P < .01$, vs chow-fed or control (Cont) mice; †, $P < .05$; ††, $P < .01$, vs STZ mice treated with vehicle (Veh).

γ-Oryzanol has no effect on gene expression related to β-cell survival and proliferation in HFD- or STZ-induced diabetic mice

To explore the potential of γ-oryzanol on β-cell survival and proliferation, we assessed the expression levels

of genes related to β-cell survival and proliferation, including *pancreatic and duodenal homeobox 1, v-maf musculoaponeurotic fibrosarcoma oncogene family, protein A, neurogenin 3*, *Ins1*, *Ins2*, and *cyclin-dependent kinase inhibitor 1A* (22) in islets from HFD-fed mice and STZ-treated diabetic mice. In HFD-fed mice, mRNA levels of these genes showed a trend to increase, whereas the trend was cancelled by γ-oryzanol (Figure 4A). Also in STZ-treated mice, γ-oryzanol did not increase the expression levels of these genes (Figure 4B). In tunicamycin-treated MIN6 cells, there was no change in mRNA levels of these genes (Supplemental Figure 4).

Discussion

In the present study, we demonstrated that γ-oryzanol ameliorated ER stress-induced β-cell apoptosis and glucose intolerance in both HFD-fed mice and STZ-treated mice (Figures 1–3 and Supplemental Figure 3). Also in MIN6 cells, tunicamycin-induced ER stress and after apoptosis were restored by γ-oryzanol (Figures 1 and 2 and Supplemental Figure 2). On the other hand, γ-oryzanol did not show apparent effects on β-cell survival and proliferation both in vivo and in vitro (Figure 4 and Supplemental Figure 4), suggesting that γ-oryzanol ameliorates β-cell function mainly via reduction of ER stress-induced apoptosis. ER stress plays a critical role in regulating function of β-cells and in the pathophysiology of type 2 diabetes (5, 23). Excess free fatty acid, chronic inflammation, and hyperglycaemia are known to provoke ER stress in β-cells, leading to suppression of insulin biosynthesis, impaired GSIS, and resultant apoptosis (23). Even without apparent reduction of β-cell mass, isolated pancreatic islets from HFD-fed mice showed a pronounced aggravation of GSIS (24). We recently demonstrated that γ-oryzanol acts as a chemical chaperone in primary murine neuronal cells (3). In the present study, we demonstrated that γ-oryzanol reduced ER stress also in pancreatic β-cells, thereby improving GSIS and preventing apoptosis from β-cells both in vivo and in vitro (Figures 1–3 and Supplemental Figures 2 and 3). These data suggest that γ-oryzanol has therapeutic potential for the prevention and treatment of type 2 diabetes. Importantly, ferulic acid, a partial structure of γ-oryzanol, did not exhibit the chaperone activity in luciferase reporter assays (Supplemental Figure 1). These findings reinforce the significance of full structure of γ-oryzanol in its variety of biological actions.

A series of previous studies showed that elevation of intracellular cAMP by GLP-1, forskolin, and 3-isobutyl-1-methyl xanthine prevent β-cells from apoptosis (9, 25, 26). For example, β-cell apoptosis induced by palmitate, a potent inducer of ER stress, is rescued by GLP-1 through

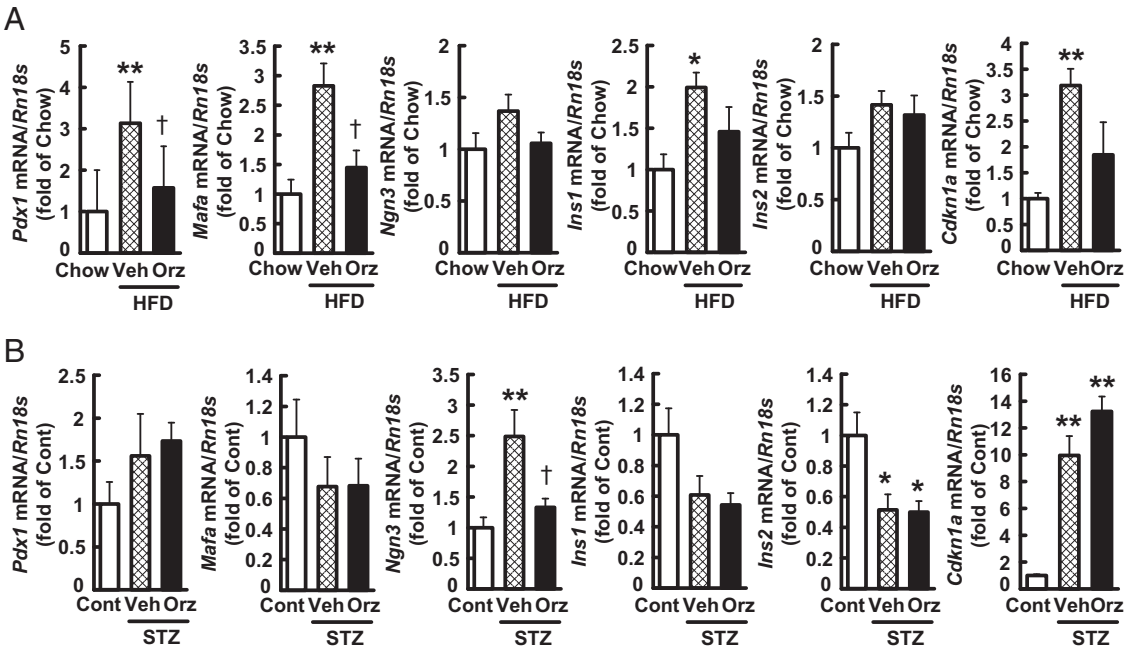

Figure 4. Effect of γ-oryzanol on expression levels of genes related to β-cell survival and proliferation factors in diabetic mice. Expression levels of mRNA for pancreatic and duodenal homeobox 1 (*Pdx1*), v-maf musculoaponeurotic fibrosarcoma oncogene family, protein A (*Mafa*), neurogenin 3 (*Ngn3*), *Ins1*, *Ins2*, and cyclin-dependent kinase inhibitor 1A (*Cdkn1a*) in pancreatic islets from γ-oryzanol-treated HFD-fed (A) (n = 6) or STZ-treated mice (B) (n = 5). The mRNA levels were determined by real-time PCR and normalized by those of *Rn18s*. Data are expressed as mean ± SEM. *, $P < .05$; **, $P < .01$, vs chow-fed or control (Cont) mice; †, $P < .05$; ††, $P < .01$, vs HFD-fed or STZ mice treated with vehicle (Veh).

activation of the cAMP/PKA pathway in rat β-cell line, RINm5F (9). On the other hand, via the decrease in intracellular cAMP level, dopamine provokes apoptosis in various types of neuronal and lactotrope cells (27, 28). We recently found that γ-oryzanol enhances GSIS through activation of the cAMP/PKA pathway by suppression of dopamine D2 receptor signaling (C. Kozuka, S. Sunagawa, R. Ueda, M. Higa, Y. Ohshiro, H. Tanaka, C. Shimizu-Okabe, C. Takayama, M. Matsushita, M. Tsutsui, S. Ishiuchi, M. Nakata, T. Yada, J. Miyazaki, S. Oyadomari, M. Shimabukuro, and H. Masuzaki, unpublished data). To our knowledge, the present study is the first demonstration that γ-oryzanol directly improves the survival and function of murine pancreatic islets in a similar manner to GLP-1. Experiments to explore the potential target molecule for γ-oryzanol are underway in our laboratory.

The present study unveiled the enigma on the molecular mechanism whereby γ-oryzanol protects pancreatic islets in a diabetic status. Because the phenotype of ER stress-based genetic models of diabetes such as *Akita* mice is extremely severe (29, 30), we used HFD- and STZ-induced diabetic mice. We think it critical to assess the impact of γ-oryzanol on glucose metabolism in models relevant to life style-related human diseases. Our novel findings that γ-oryzanol acts as a potent ER stress eraser in pancreatic β-cells may open a fresh avenue for natural food-based approaches toward the prevention and treatment of type 2 diabetes in humans.

Acknowledgments

We thank M. Takaki (University of the Ryukyus) and J. Yamakawa, M. Okayasu, S. Okayasu (Okayasu shouten Co, Ltd, Saitama, Japan) for technical help. We also thank M. Hirata, I. Asato, and C. Noguchi (University of the Ryukyus) for assistance. C.K. is a Research Fellow of the Japan Society for the Promotion of Science.

Address all correspondence and requests for reprints to: Hiroaki Masuzaki, MD, PhD, Division of Endocrinology, Diabetes and Metabolism, Hematology, Rheumatology (Second Department of Internal Medicine), Graduate School of Medicine, University of the Ryukyus, 207 Uehara, Nishihara, Nakagami-gun, Okinawa 903-0215, Japan. E-mail: hiroaki@med.u-ryukyu.ac.jp.

This work was supported in part by Grants-in-Aid from Japan Society for the Promotion of Science (JSPS KAKENHI Grant Numbers 24591338 and 25·9668), Takeda Science Foundation (Specified Research Grant), Society for Woman's Health Science Research (13-A1-001), Leave a Nest grants, Metabolic Syndrome Foundation, Specified Project "Establishing a research hub toward the development of an intellectual cluster in Okinawa Prefecture" (2011–2014), and Council for Science Technology and Innovation, Cross-ministerial Strategic Innovation Promotion Program, "Technologies for creating next-generation agriculture, forestry and fisheries."

Disclosure Summary: The authors have nothing to disclose.

References

1. **Lerma-Garcia MJ, Herrero-Martinez JM, Simo-Alfonso EF, Mendonca CRB, Ramis-Ramos G.** Composition, industrial processing and applications of rice bran γ-oryzanol. *Food Chem*. 2009;115(2):389–404.
2. **Kozuka C, Yabiku K, Takayama C, Matsushita M, Shimabukuro M.** Natural food science based novel approach toward prevention and treatment of obesity and type 2 diabetes: recent studies on brown rice and γ-oryzanol. *Obesity Research, Clinical Practice*. 2013;7(3):e165–e172.
3. **Kozuka C, Yabiku K, Sunagawa S, et al.** Brown rice and its component, γ-oryzanol, attenuate the preference for high-fat diet by decreasing hypothalamic endoplasmic reticulum stress in mice. *Diabetes*. 2012;61(12):3084–3093.
4. **Shimabukuro M, Higa M, Kinjo R, et al.** Effects of the brown rice diet on visceral obesity and endothelial function: the BRAVO study. *Br J Nutr*. 2014;111(2):310–320.
5. **Cnop M, Foufelle F, Velloso LA.** Endoplasmic reticulum stress, obesity and diabetes. *Trends Mol Med*. 2012;18(1):59–68.
6. **Lerner AG, Upton JP, Praveen PV, et al.** IRE1α induces thioredoxin-interacting protein to activate the NLRP3 inflammasome and promote programmed cell death under irremediable ER stress. *Cell Metab*. 2012;16(2):250–264.
7. **Oslowski CM, Hara T, O'Sullivan-Murphy B, et al.** Thioredoxin-interacting protein mediates ER stress-induced β cell death through initiation of the inflammasome. *Cell Metab*. 2012;16(2):265–273.
8. **Mori K.** Tripartite management of unfolded proteins in the endoplasmic reticulum. *Cell*. 2000;101(5):451–454.
9. **Kwon G, Pappan KL, Marshall CA, Schaffer JE, McDaniel ML.** cAMP dose-dependently prevents palmitate-induced apoptosis by both protein kinase A- and cAMP-guanine nucleotide exchange factor-dependent pathways in β-cells. *J Biol Chem*. 2004;279(10):8938–8945.
10. **Xu G, Stoffers DA, Habener JF, Bonner-Weir S.** Exendin-4 stimulates both β-cell replication and neogenesis, resulting in increased β-cell mass and improved glucose tolerance in diabetic rats. *Diabetes*. 1999;48(12):2270–2276.
11. **Ishihara H, Asano T, Tsukuda K, et al.** Pancreatic β cell line MIN6 exhibits characteristics of glucose metabolism and glucose-stimulated insulin secretion similar to those of normal islets. *Diabetologia*. 1993;36(11):1139–1145.
12. **Kusakabe T, Tanioka H, Ebihara K, et al.** Beneficial effects of leptin on glycaemic and lipid control in a mouse model of type 2 diabetes with increased adiposity induced by streptozotocin and a high-fat diet. *Diabetologia*. 2009;52(4):675–683.
13. **Zhang R, Kim JS, Kang KA, Piao MJ, Kim KC, Hyun JW.** Protective mechanism of KIOM-4 in streptozotocin-induced pancreatic β-cells damage is involved in the inhibition of endoplasmic reticulum stress. *Evid Based Complement Alternat Med*. 2011;2011:231938.
14. **Folch J, Lebaron FN.** The isolation from brain tissue of a trypsin-resistant protein fraction containing combined inositol, and its relation to neurokeratin. *J Neurochem*. 1956;1(2):101–108.
15. **Zmuda EJ, Powell CA, Hai TA.** Method for murine islet isolation and subcapsular kidney transplantation. *J Vis Exp*. 2011(50):e2096.
16. **Tanaka T, Masuzaki H, Yasue S, et al.** Central melanocortin signaling restores skeletal muscle AMP-activated protein kinase phosphorylation in mice fed a high-fat diet. *Cell Metab*. 2007;5(5):395–402.
17. **Akerfeldt MC, Howes J, Chan JY, et al.** Cytokine-induced β-cell death is independent of endoplasmic reticulum stress signaling. *Diabetes*. 2008;57(11):3034–3044.
18. **Chakravarthy MV, Zhu Y, Wice MB, et al.** Decreased fetal size is

associated with β-cell hyperfunction in early life and failure with age. *Diabetes*. 2008;57(10):2698–2707.
19. **Lee AH, Heidtman K, Hotamisligil GS, Glimcher LH.** Dual and opposing roles of the unfolded protein response regulated by IRE1α and XBP1 in proinsulin processing and insulin secretion. *Proc Natl Acad Sci USA*. 2011;108(21):8885–8890.
20. **Bergman RN, Finegood DT, Kahn SE.** The evolution of β-cell dysfunction and insulin resistance in type 2 diabetes. *Eur J Clin Invest*. 2002;32(suppl 3):35–45.
21. **Scheuner D, Kaufman RJ.** The unfolded protein response: a pathway that links insulin demand with β-cell failure and diabetes. *Endocr Rev*. 2008;29(3):317–333.
22. **Jourdan T, Godlewski G, Cinar R, et al.** Activation of the Nlrp3 inflammasome in infiltrating macrophages by endocannabinoids mediates β cell loss in type 2 diabetes. *Nat Med*. 2013;19(9):1132–1140.
23. **Volchuk A, Ron D.** The endoplasmic reticulum stress response in the pancreatic β-cell. *Diabetes Obes Metab*. 2010;12(suppl 2):48–57.
24. **Peyot ML, Pepin E, Lamontagne J, et al.** β-Cell failure in diet-induced obese mice stratified according to body weight gain: secretory dysfunction and altered islet lipid metabolism without steatosis or reduced β-cell mass. *Diabetes*. 2010;59(9):2178–2187.
25. **Li L, El-Kholy W, Rhodes CJ, Brubaker PL.** Glucagon-like peptide-1 protects β cells from cytokine-induced apoptosis and necrosis: role of protein kinase B. *Diabetologia*. 2005;48(7):1339–1349.
26. **Jhala US, Canettieri G, Screaton RA, et al.** cAMP promotes pancreatic β-cell survival via CREB-mediated induction of IRS2. *Genes Dev*. 2003;17(13):1575–1580.
27. **Radl DB, Ferraris J, Boti V, Seilicovich A, Sarkar DK, Pisera D.** Dopamine-induced apoptosis of lactotropes is mediated by the short isoform of D2 receptor. *Plos One*. 2011;6(3):e18097.
28. **Bozzi Y, Borrelli E.** Dopamine in neurotoxicity and neuroprotection: what do D2 receptors have to do with it? *Trends Neurosci*. 2006;29(3):167–174.
29. **Oyadomari S, Koizumi A, Takeda K, et al.** Targeted disruption of the Chop gene delays endoplasmic reticulum stress-mediated diabetes. *J Clin Invest*. 2002;109(4):525–532.
30. **Yoshioka M, Kayo T, Ikeda T, Koizumi A.** A novel locus, Mody4, distal to D7Mit189 on chromosome 7 determines early-onset NIDDM in nonobese C57BL/6 (Akita) mutant mice. *Diabetes*. 1997;46(5):887–894.

Review

カルシウム透過性AMPA型グルタミン酸受容体と神経膠芽腫
Ca^{2+}-permeable AMPA -type glutamate receptors and glioblastomas

石内 勝吾
Shogo Ishiuchi

琉球大学大学院 医学研究科脳神経科教授
Professor and Chairman Department of Neurosurgery, University of the Ryukyus, Graduate school of Medicine

略 歴

1985年3月 群馬大学医学部医学科卒業
1999年1月 科学技術振興事業団「脳を知る」(CREST)研究員
1999年7月 群馬大学医学部脳神経外科助手
2002年9月 群馬大学医学部脳神経外科講師
2009年6月 琉球大学医学部脳神経外科教授
2011年1月 琉球大学医学部副医学部長
2012年8月 琉球大学医学部附属病院長特別補佐
2014年1月 琉球大学医学部附属病院長副病院長

そ の 他

時実利彦記念脳研究基金 1992年
第11回日本脳腫瘍学会「星野賞」受賞 2003年
第42回高松宮妃癌研究基金 2013年
President of the 3rd International Society of Radiation Neurobiology conference 2013年

Abstract

Glioblastoma cells release and exploit glutamate for proliferation and migration by autocrine or paracrine loops through Ca^{2+}-permeable･-amino-3-hydroxy-5-methyl-4-isoxazolepropionate -type glutamate receptors (CP-AMPAR). Here we show the molecular mechanism behind glioblastoma cells expressing CP-AMPAR, and refer to its role for gliomagenesis.

Key words : calcium-permeable AMPA type glutamate receptor, glioblastoma, invasive growth behavior, gliomagenesis

received/2015/06/28
accepted/2015/07/07

はじめに

グルタミン酸は、ヒトの認知、知覚、記憶および学習など興奮性シナプス伝達に関与する重要な興奮性伝達物質である。一方、脳虚血、外傷、てんかん、神経変性・代謝疾患など中枢系の様々な疾患において、細胞外に過剰放出されたグルタミン酸は、興奮毒性という共通の現象を引き起こし病勢の根幹に関与することが古くから知られている。これらの現象の背景に重要な役割を果すのがグルタミン酸受容体の中のイオンチャネル型受容体(ionotropic glutamate receptor; iGluR)に分類されるNMDA(N-methyl-D-aspartic acid)型　と　AMPA(α-amino-3-hydroxy-5-methyl-4-isoxazolepropionate)型受容体である。NMDA型受容体を介するカルシウムの急速な細胞内流入が病態生理としてよく知られている一方でAMPA型グルタミン酸受容体は一般的に不透過型として理解されてきた。近年、カルシウム透過性(calcium permeable)AMPA(CP-AMPA)型受容体の存在が認識され、このチャネルが多彩な疾患の病態生理に重要な役割を果たす事が判明し注目されている。本稿では脳腫瘍ことに神経膠芽腫における役割について概説する。

グルタミン酸受容体

1）グルタミン酸受容体の分類

グルタミン酸受容体は、イオンチャネル型受容体(ionotropic glutamate receptor; iGluR)と代謝調節型受容体(metabotropic glutamate receptor; mGluR)の２種類に大別される。イオンチャンネル型受容体(iGluR)はさらにアゴニスト特異性により、NMDA型、AMPA型とカイニン酸型の３つのサブタイプに分類され、リガンドが同定されていないOrphan型もその分子構造の相同性からこの中に入る。AMPA型受容体はGluA1-4の４つのサブユニットから形成され、受容体はこれらのサブユニットの単独または様々な組み合わせからなる４量体で形成されている。カルシウム透過性という機能的観点からはGRIA2遺伝子にコードされるGluA2サブユニットの発現の有無が重要である。すなわち、GluA2発現の無い場合は、カルシウム透過性を示し、逆にGluA2が発現しているとカルシウム不透過性となる。GluA2の変異体はGluA2(Q)と呼ばれている。野生型または編集型GluA2はイオン透過性に関わる細胞膜のM2部(Q/R部位)がアルギニンで陽性に帯電しているため細胞外のカルシウムをほとんど通さないが、変異型または未編集型GluA2(Q)はグルタミンで中性であるために、陽イオンであるカルシウムとは反撥せずチャネルは強いカルシウム透過性を示すことになる(Table. 1)。AMPA型受容体のチャネルの透過性を考える上でGRIA1遺伝子にコードされるGluA1受容体の細胞膜への trafficking機構も重要である。これはcGMP-dependent kinase II(cGKII)依存性にGluA1のリン酸化が促進されることにより生じる。

Table. 1 The size of four AMPA receptor subunits including GluA1,GluA2, GluA3, and GluA4 are similar in approximate 900 amino acids, and they share high amino acid sequence identity. Importantly, receptor permeability for calcium is depend upon a transmembrane portion of the AMPA receptor GluA2 subunit called Q/Rsite. A glutamine residue (Q; CGA) in M2 is encoded in the genes for GluRA1, A3, and GluA4, however, GluA2 contains an arginine (R; CGG) at this position termed the Q/R site indicating by voxel in the figure. This codon change due to the adenosine (A)-to-guanosine (G) alteration is generated by site-directed nuclear RNA editing, and mature brain contained abundant edited form of GluA2, and the unedited immature GluA2,namely GluA2(Q) was present in fetal brain. A point mutagenesis at the Q/R site from guanosine (G)-to-adenosine (A) transformed GluA2(R) to GluA2(Q), which in contrast induces high calcium permeability.

Amino acid sequences of the M2 segments of AMPA receptor subunits.

GluA1 NE-FGIFNSLWFSLGAFMQQGC-DIS
GluA2 NE-FGIFNSLWFSLGAFMRQGC-DIS
GluA3 NE-FGIFNSLWFSLGAFMQQGC-DIS
GluA4 NE-FGIFNSLWFSLGAFMQQGC-DIS

Q/R site

以上まとめると従来カルシウム透過性を示すイオン型グルタミン酸受容体はもっぱらNMDA型受容体と考えられAMPA型受容体は不透過とされてきたがカルシウム透過性を示すCP-AMPA型受容体の存在が近年確認された。その分子機構として1)GRIA2遺伝子のサイレンシングによるGluA2発現が欠落した場合2)mRNA翻訳機構の異常からGluA2(Q)が発現する場合3)GluA1の細胞膜へのtraffickingが促進された場合の3型が認められる。CP-AMPA型受容体と脳腫瘍ことに神経膠芽腫との関連について次項で述べてみたい。

2）脳腫瘍細胞での発現様式とその機能

1990年代から、新鮮な手術摘出腫瘍より準備された初代培養系においてグルタミン酸やカイニン酸の投与により電気生理学的応答や細胞内カルシウムの上昇の現象が捉えられ[1]、これらの応答はAMPA型グルタミン酸受容体の拮抗薬CNQXにより抑制されるという知見が報告された。2001年には神経細胞に豊富に認められるNMDA受容体遺伝子サブユニットNR1、NR2A、NR2B、NR2CやAMPA型受容体GluA2サブユニットは神経膠芽腫においては、神経細胞に比較して著しくその発現が低下しているという報告がなされた[2]。2002年に著者らは、手術にて摘出した腫瘍細胞の初代培養とその樹立株の解析からAMPA型グルタミン酸受容体が神経膠芽腫に発現していることを報告した[3]。解析した16例中12例症例でGluA2の蛋白発現がないこと、またカルシウム測光による解析から腫瘍細胞は100 μMのAMPA agonistにて細胞内カルシウムの上昇を認めAMPA型受容体拮抗薬NBQXでこの反応が完全に遮断される事から機能的にカルシウム透過性であることを示した。また独自に樹立したヒトグリオーマ細胞を用いたin vitroおよびin vivo疾患モデルにおいて、編集型GluA2の強制導入により腫瘍の移動性と増殖性が阻害され、逆に変異型GluA2(Q)を強制発現させると遊走性の亢進と細胞死の抑制が認められたことより、このチャネルを介するカルシウムの流入によって引き起こされる緩徐な細胞内カルシウムの上昇が腫瘍細胞の浸潤と増殖に関与していることをはじめて明らかにした(Fig. 1 & Fig. 2)。16症例中4例、2割の症例でmRNAレベルでの未編集型と編集型の共発現が見られた。このように神経膠腫細胞が発現するAMPA型受容体はGluA2サブユニットを欠くものと、GluA2の変異体GluA2(Q)を発現するもの[4]とがありいずれもその受容体の機能はカルシウム透過型である。さらに摘出腫瘍から培養され樹立された培養株ではGluA2が消失しGluA1の発現が有意となる。これはbFGF(basic fibroblast growth factor)やPDGF(platelet derived growth factor)などの様々なenvironmental cueによりGluA1のtraffickingが促進された事によると考えられている。

神経膠芽腫の浸潤性増殖に対する治療への応用

1）グルタミン酸/カルシウム透過性AMPA型受容体/Aktシグナリング

グリオーマに対する分子標的治療としては上皮増殖因子受容体(EGFR)[5]、血管内皮増殖因子(VEGF)、血小板増殖因子受容体(PDGFR)[6]などに対する拮抗薬や中和抗体が臨床応用されている[7]。成長因子(GF)を介するチロシンキナーゼの活性化は最終的にはAktのリン酸化を促進する[8), 9), 10)]。分子標的剤は成長因子(GF)を介するチロシンキナーゼの活性化を抑制することによりAktの脱リン酸化を目指すものである。神経膠芽腫細胞に発現するカルシウム透過性AMPA型グルタミン酸受容体は、Aktのリン酸化に関与しglutamate-AMPA受容体-Akt pathwayを通じて新たな増殖と浸潤を促進する[11)]。神経膠芽腫では、EGFRからのシグナルがphosphatidylinositol-3-OH kinase (PI3K)を活性化しphosphatidylinositol(4,5)-biphosphate(PIP2)はphosphatidylinositol(3,4,5)-triphosphate(PIP3)に変換され、phosphatase/tensin homolog on chromosome 10(PTEN)欠失がさらにこの変換を促進する[12), 13), 14), 15)]。PIP3はAktをリン酸化する。Aktのリン酸化はkinase domainにあるThr-308とC-terminal regulatory alignmentのSer-473部位により制御され、それぞれPDK-1、PDK-2[16)]がそのリン酸化にかかわる。神経膠芽腫では、通常PDK-1は常時リン酸化されており、GF-PI3K-PDK1-Akt signalingはグリオーマの浸潤性増殖に関与している。PI3K阻害剤であるwortmanninやLY294002を高濃度で投与するとAktのリン酸化は抑制される。著者らは高濃度のPI3K阻害剤下でも、AMPA受容体を刺激するとAktのリン酸化が認められることを見出し、glutamate-AMPA型受容体-Akt pathwayという新たなcascadeを突き止めた。このpathwayは現在分子標的の主たる対象となっているtyrosine kinaseを介するPI3K-PDK1[17)]を介してAktを活性化する経路の側副路と考えている。tyrosine kinaseを標的とした各種拮抗薬を用いた治療では短期間で大多数の症例で治療不応、薬剤耐性が認められ[18)]、その一因を説明するものと思われる。実際にAMPA型受容体に対する拮抗薬YM872と増殖因子PDGFR, c-kitに対する拮抗薬AG1296を併用して使用するとヒト

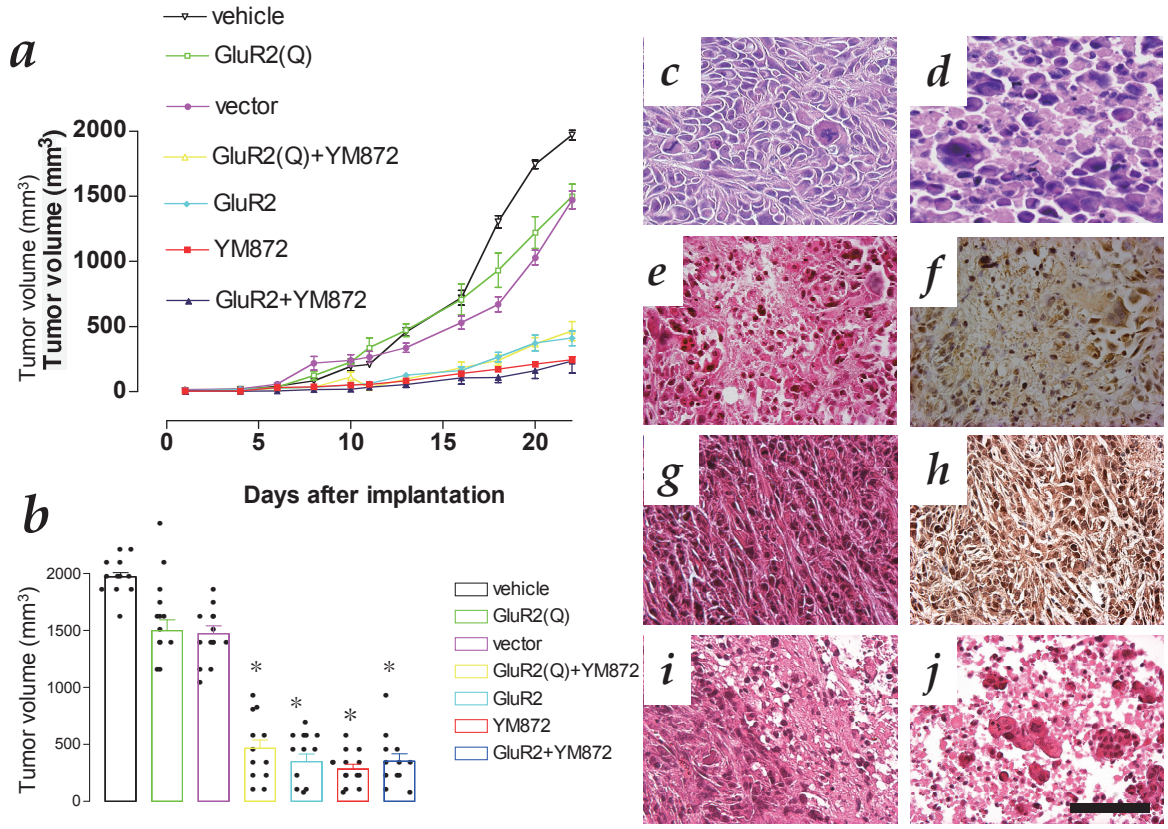

Fig. 1　Effects of manipulation of AMPA receptors on tumor growth. ***a,*** Effects of various treatments on growth rate of tumors grafted into the subcutaneous tissue of nude mice: injection of PBS (vehicle as control for application of YM872, a non-competitive AMPAR antagonist, inverted triangles); expression of GluA2(Q) (open squares); injection of AxCALNLGluA2 without AxCANCre (vector as control for expression of GluA2 and GluA2(Q), filled circles); expression of GluA2(Q) plus application of YM872 (open triangles); expression of GluA2 (filled diamonds); application of YM872 (filled squares); and expression of GluA2 plus application of YM872 (filled triangles). For each treatment, 12 animals were used. Each plot represents the mean ± s.e.m. (n = 12) of the tumor volume. ***b,*** Plots of tumor volumes measured 22 days after inoculation. For each treatment, raw data obtained from 12 animals are plotted. * indicates significant difference at $p<0.001$ relative to control (either vehicle or vector). ***c-f,*** Histology of tumor tissues treated with the vehicle (***c***) and YM872 (***d***), and of those to which the GluR2 gene was delivered (***e, f***). ***c, d and e***, HE staining. f, Immunostaining with anti-GluA2 antibody. ***g-h,*** HE staining (***g***) and immunostaining with anti-GluA2 antibody (***h***) in tumor tissues to which the GluA2(Q) gene was delivered. ***i,*** HE staining of tumor tissues expressing GluA2(Q) and treated with YM872. ***j,*** HE staining of tumor tissues expressing GluA2 and treated with YM872. The tissues in ***c-j*** were taken 22 days after tumor inoculation. Scale bar in ***j*** 50 μm for ***c-j.*** Note in ***a*** & ***b,*** GluR2 equally means GluA2.

glioblastoma の動物モデルで効果的に増殖抑制が達成された[19]。

2）グルタミン酸産生の機序

神経伝達物質であるグルタミン酸は神経細胞のシナプス前極から分泌され、シナプス後極のグルタミン酸受容体を興奮させる。余剰のグルタミン酸は先に述べたように強い興奮毒性をもたらすため、正常星細胞のグルタミン酸トランスポーターによって厳密に排除される。実際グリオーマ細胞はグルタミンからグルタミン酸を de novo で産生する事が出来る。樹立培養株では、グルタミン酸を透析することでグルタミンおよびグルタミン酸を含まない培養液中で発育させると、数日で培養液中のグルタミン酸とグルタミンはともに 100 μM 以上の濃度に達する[11]。またアミノ酸がなくともブドウ糖があればTCA サイクルを回してグルタミン酸を産生すること

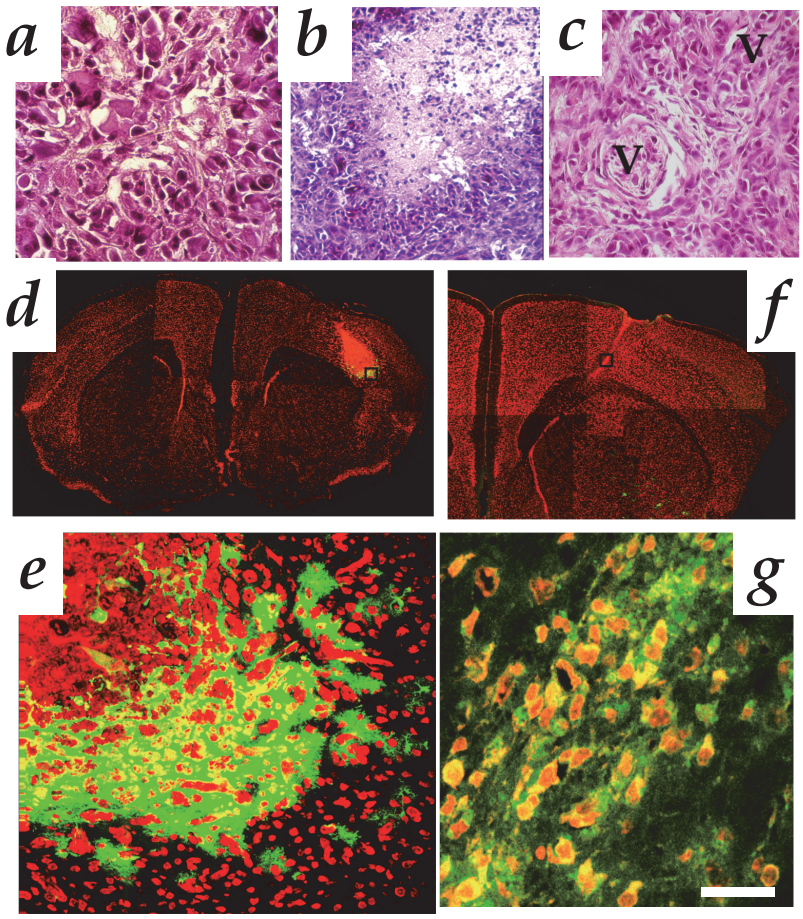

Fig. 2 Effects of GluA2 expression on tumor transplantation. ***a-c,*** Histopathology of the tumor formed by transplantation of cultured glioblastoma cells into the nude mouse. The tumor was characterized by pleomorphism (***a***), necrosis with pseudopalisading (***b***), and microvascular proliferation (***c***). 'v' indicates tumor vessels (HE staining). ***d,*** Tumor formation at 9 days after transplantation of 2×10^5 cultured glioblastoma cells into the subcortical area of the nude mouse cerebrum. The cultured cells had been infected with AxCAGFP and AxCALNLGluA2 each at MOI 5 for expression of GFP (green) two days before transplantation, and stained by PI(red). ***e,*** Higher magnification view of the boxed area in ***d. f,*** Cells at 14 days after transplantation of 2×10^5 cultured glioblastoma cells. The cultured cells had been infected with AxCAGFP and AxCALNLGluR2 together with AxCANCre each at MOI 5 for expression of both GFP and GluR2 two days before transplantation. ***g,*** Higher magnification view of the boxed area in ***f.*** Note apoptotic nuclear morphology caused by expression of GluR2. Scale bar in ***g*** represents 50 μm for ***a, e*** and ***g,*** 100 μm for ***b,*** 75 μm for ***c,*** 1500 μm for ***d,*** and 1000 μm for ***f.***

ができる。細胞外シスチンを投与すると細胞外グルタミン酸濃度が上昇する事から腫瘍細胞膜に存在するシスチン・グルタミン酸エクスチェンジャーの関与も指摘されている[20]。このチャネルの拮抗薬は潰瘍性大腸炎やクローン病の治療薬であるサラゾピリンであり、脳腫瘍動物モデルで抗腫瘍効果が確認されている[21]。Glutamate transporter 1(GLT1)[22]や excitatory amino acid transporter 2(EAAT-2)[23]などのグルタミン酸トランスポーターの発現低下が悪性度の高いグリオーマでは認められており、細胞外グルタミン酸の過剰状態に拍車をかけることになる。実験的に GLT1 や EAAT-2 を強制発現させると腫瘍増殖が抑制される。以上より、グリオーマ細胞は細胞外にグルタミン酸を放出して周囲の脳組織を興奮性神経細胞死させることで空間拡大に利用するだけでなく、グルタミン酸をリガンドとして自ら受容体を賦活化しオートクラインおよびパラクラインに増殖と浸潤に悪用する事で浸潤性増殖を促進することが判明した[11]。神経細胞体の中には mM 単位のグルタミン酸が存在するため興奮性神経細胞死に陥った細胞から細胞外にこぼれ落ちるグルタミン酸を利用してグリオーマはさ

らに脳深部へと浸潤する。最近，シナプス間隙から分泌される Neuroligin-3 も PI3-K-mTOR を活性化することで glutamate 同様にグリオーマの増殖を促進することが報告されている[24]。

発生母細胞に関する研究

以上概説したように、我々はイオン共役型グルタミン酸受容体の一つであるカルシウム透過性 AMPA 型受容体が悪性神経膠腫の増殖と遊走に重要な役割を担うことを解明してきた[3), 11), 25)]。最終項では、グリオーマの発生母細胞及び gliomagenesis に関する我々の仮説に言及したい。悪性グリオーマの発生母細胞に関しては文献的に神経幹細胞およびグリア前駆細胞が提示されている。神経幹細胞からがん幹細胞への逸脱を惹起する最初の分子メカニズムの正体が何かが解明されれば根治療法の樹立につながるはずである。先に述べた AMPA 型受容体のカルシウム透過性に重要な役割を担う GluA2 受容体は正常細胞では胎生初期に RNA editing により CAG:glutamine(Q)codon が CGG:arginine(R)codon に変化することで受容体膜様部(Q/R site)における中性のグルタミンから陽電荷のアルギニンへの変換により同じく陽イオンを有するカルシウムを不透過にさせるという分子機構により制御されていることを述べた。すなわち正常細胞では胎生初期には未編集型 GluA2Q であるが誕生後には RNA editing により全て GluA2R の翻訳型となるわけである。またヒト生検材料を用いた解析からは神経膠芽腫がカルシウム透過性を獲得する分子機構については GluA2(Q)を保有するものが 2 割、残り 8 割は GRIA2 の pre-mRNA level での epigenetic なサイレンシングにより GluA2 を欠く AMPA 受容体が形成される場合である。これ等の変化は腫瘍内で起こるわけであるが、腫瘍の階層的構築を考慮すると、本来カルシウム不透過型の AMPA 型受容体を有する正常神経幹細胞が機能的な変容を引き起こし CP-AMPA 型に改変する事で増殖と遊走の亢進を来たした細胞群がグリオーマ幹細胞ではないかと思われる。さらにこの GluA2 のサイレンシングの機序に関しては REST(Repressor element-1 silencing transcription factor)が重要である。REST は同時にミトコンドリアの電子輸送に重要な cytochrome C oxidase が GRIA2 同様に抑制される事が判明している[26]。エネルギー代謝経路とグルタミン酸受容体遺伝子双方に共通の repressor の同定は発生母細胞レベルにおけるがん化のメカニズムの理解を促進し今後根本治療の理論的背景の形成につながる可能性を秘めており大変興味深い。

終わりに

AMPA 受容体拮抗薬は、てんかん、パーキンソン病などの神経疾患ですでに臨床治験が施行されているので安全性が確認されている薬剤が複数存在し臨床応用が可能である。実際 AMPA 型受容体拮抗薬は前臨床試験で抗腫瘍効果を持つことが判明しており[3), 11)]、神経膠芽腫治療剤として有望であることが認識され、より安全性が高く治療効果の高い薬剤の開発と臨床治験が行われた。AMPA 型受容体拮抗剤はその構造によりキノキサリンジオン型(YM872, NBQX)[27)]、ピリドチアジン型(YM928)[28)]、ベンゾジアゼピン型(GYKI52466, Talampanel)[29)]の 3 系統に分類される。グリオーマに対する抗腫瘍効果は著者らの研究開発からいずれの系統の薬剤でも同等の薬効が確認されている。AMPA 型受容体拮抗薬はまた、競合的拮抗薬と非競合的拮抗薬に分類される。前者では、作用時間が短く多量なグルタミン酸の存在するところでは薬効が低下する。悪性度の高いグリオーマでは、特に浸潤最先端部では、グリオーマ細胞から直接放出されるグルタミン酸と細胞死に陥った神経細胞より漏れ出す過剰なグルタミン酸が高濃度に認められることから、非競合的拮抗薬が浸潤機構の病態生理を考えると有利である。より合理的に CP-AMPA 型受容体を選択的に拮抗する化合物もあるが毒性や安全性から臨床治験にはあがってきておらず現時点での実用化は成功していない。経口非競合的拮抗薬タランパネルについては米国にて 2005 年 12 月から 2007 年 7 月に登録された 72 例の初発神経膠芽腫患者に対して多施設共同による第 2 相試験が行われた[30)]。症例は、平均年齢 60 歳(37 歳 -85 歳)で 70 歳以上が 17% と高齢者が多く、平均 KPS 90(70-100)、生検のみの症例が 23% 含まれているにも拘らず平均生存中央値は 17.9 ヶ月、比較対照群では 14.6 ヶ月と良好な生存期間の延長をもたらした。現行の悪性グリオーマの標準治療剤はいずれもがん幹細胞から派生する多様な clonal progeny を攻撃対象とする薬剤が用いられているが今後はがん幹細胞自体を標的にする、さらに踏み込んで正常幹細胞からがん幹細胞への逸脱を予防する治療剤の創出も望まれる。

引用文献

1. **Labrakis C, Patt S, Hartman J, and Kettenmann H:** Glutamate receptor activation can trigger electrical acivity in human glioma cells.
Eur. J. Neurosci. 10: 2153-62, 1998.

2. **Markert JM, Fuller CM, Gillespire GY, Bubien JK, McLean LA, Hong RL, Lee K, Gullans SR, Mapstone TB, Benos DJ:** Differential gene expression profiling in human brain tumors.
Physiol Genomics. 5: 21-33, 2001.

3. **Ishiuchi S, Tsuzuki K, YoshidaY, Yamada N, Hagimura N, Okado H, Miwa A, Kurihara H, Nakazato Y, Tamura M, Sasaki T, Ozawa S:** Blockage of Ca^{2+}-permeable AMPA receptors suppresses migration and induces apoptosis in human glioblastoma cells. Nat. Med.8 : 971-978, 2002.

4. **Maas, S, Patt S, Schrey M, Rich A:** Undererediting of glutamate receptor GluR-B mRNA in malignant gliomas. Proc Natl Acad Sci USA 98: 14687-92, 2001.

5. **Smith JS, Tachibana I, Passe SM, Huntley BK, Borell TJ, Iturria N, O'Fallon JR, Schaefer PL, Scheithauer BW, James CD, Buckner JC, Jenkins RB:** PTEN mutation, EGFR amplification, and outcome in patients with anaplastic astrocytoma and glioblastoma multiforme. J. Natl. Cancer Inst. 93: 1246-1256, 2001.

6. **Lokker NA, Sullivan CM, Hollenbach SJ, Israel MA, Giese NA:** Platelet-derived growth factor (PDGF) autocrine signaling regulates survival and mitogenic pathways in glioblastoma cells: evidence that the novelPDGF-C and PDGF-D ligands may play a role in the development of brain tumors. Cancer Res. 62: 3729-3735, 2002.

7. **Shawver LK, Salmon D, Ullrich HM: Smart drugs :** tyrosine kinase inhibitors in cancer therapy. Cancer Cell 1: 117-123, 2002.

8. **Datta SR, Brunet A, Greenberg ME:** Cellular survival: a play in three Akts. Genes Dev. 13: 2905-2927, 1999.

9. **Alessi DR, Cohen P:** Mechanism of activation and function of protein kinase B. Curr. Opin. Genet. Dev. 8: 55-62, 1998.

10. **Osaki M, Oshimura M, Ito H:** PI3K-Akt pathway: its functions and alterations in human cancer. Apoptosis 9: 667-676, 2004.

11. **Ishiuchi S, Yoshida Y, Sugawara K, Aihara M, Ohtani T Watanabe T, Saito N, Tsuzuki K, Okado H, Miwa A, Nakazato Y, Ozawa S:** Ca^{2+}-permwable AMPA receptors regulate growth of human glioblastoma via akt activation. J Neurosci 27: 7987-8001, 2007.

12. **Cantley LC, Neel BG:** New insights into tumor suppression: PTEN suppresses tumor formation by restraining the phosphoinositide 3-kinase/AKT pathway. Proc. Natl. Acad. Sci. USA 96: 4240-4245, 1999.

13. **Li J, Yen C, Liaw D, Podsypanina K, Bose S, Want SI, Puc J, Miliaresis C, Rodgers L, McCombie R, Bigner SH, Giovanella BC, Ittmann M, Tycko B, Hibshoosh H, Wigler MH, Parsons R:** PTEN, a putative protein tyrosine phosphatase gene mutated in human brain, breast, and prostate cancer. Science 275: 1943-1947, 1997.

14. **Maehama T, Dixon JE:** The tumor suppressor, PTEN/MMAC1, dephosphorylates the lipid second messenger, phosphatidylinositol 3,4,5-trisphosphate. J. Biol. Chem. 273: 13375-13378, 1998.

15. **Choe G, Horvath S, Cloughesy TF, Crosby K, Seligson D, Palotie A, Inge L, Smith BL, Sawyers CL, Mischel PS:** Analysis of the phosphatidylinositol 3'-kinase signaling pathway in glioblastoma patients in vivo. Cancer Res. 63: 2742-2746, 2003.

16. **Toker A, Newton AC et al:** Akt/protein kinase B is regulated by autophosphorylation at the hypothetical PDK-2 site. J. Biol. Chem. 275: 8271-8274, 2000.

17. **Vanhaesebroeck B, Alessi DR et al:** The PI3K-PDK1 connection: more than just a road to PKB. Biochem. J. 346: 561-576, 2000.

18. **Mellinghoff IK, Wang MD, Vivanco I, Haas-Kogan DA, Zhu S, Dia EQ, Lu KV, Yoshimoto K, Huang JH, Chute DJ, Riggs BL, Horvath S, Liau LM, Cavenee WK, Rao PN, Beroukhim R, Peck TC, Lee JC, Sellers WR, Stokoe D, Prados M, Cloughesy TF, Sawyers CL, Mischel PS:** Molecular determinants of the response of glioblastomas to EGFR kinase inhibitors. N. Engl. J. Med. 353: 2012-2024, 2005.

19. **Watanabe T, Ohtani T, Aihara M, Ishiuchi S:** Enhanced antitumor effect of YM872 and AG1296 combination treatment on human glioblastoma xenograft models.J Neurosurg. 118: 838-45. 2013.

20. **Ye ZC, Rothstein JD, Sontheimer H:** Compromised glutamate transport in human glioma cells: reduction-mislocalization of sodium-dependent glutamate transporters and enhanced activity of cystine-glutamate exchange.J Neurosci. 19: 10767-77, 1999.

21. **Chung WJ, Sontheimer H:** Sulfasalazine inhibits the growth of primary brain tumors independent of nuclear factor-kappaB. J Neurochem. 110: 182-93, 2009.

22. **Vanhoutte** N**, Hermans E:** Glutamate-induced glioma cell proliferation is prevented by functional expression of the glutamate transporter GLT-1. FEBS Letters 582: 1847–1852, 2008.

23. **de Groot JF, Liu TJ, Fuller G, Yung WK:** The excitatory amino acid transporter-2 induces apoptosis and decreases glioma growth in vitro and in vivo. Cancer Res. 65: 1934-40, 2005.

24. **Venkatesh HS, Johung TB, Caretti V, Noll A, Tang Y, Nagaraja S, Gibson EM, Mount CW, Polepalli J, Mitra SS, Woo PJ, Malenka RC, Vogel H, Bredel M, Mallick P, Monje M.** Neuronal Activity Promotes Glioma Growth through Neuroligin-3 Secretion Cell. 7 ; 161: 803-16. 2015.

25. **Ishiuchi S.** New roles of glutamate receptors in glias and gliomas. Brain Nerve. 61: 753-64. 2009.

26. **Priya A, Johar K, Wong-Riley MT.** Nuclear respiratory factor 2 regulates the expression of the same NMDA receptor subunit genes as NRF-1: both factors act by a concurrent and parallel mechanism to couple energy metabolism and synaptic transmission. Biochim Biophys Acta. 1833: 48-58. 2013.

27. **Kohara A. Okada M, Tsutsumi R, Ohno K, Takahashi M, Shimizu-Sasamata M, Shishikura J, Inami H, Sakamoto S, Yamaguchi T:** In vitro characterization of YM872, a selective, potent and highly water-soluble α-amino-3-hydroxy-5-methylisoxazole-4-propionate receptor antagonist. J. Pharm. Pharmacol. 50: 795-801, 1998.

28. **Yamashita H, Ohno K, Amada Y, Imai H, Shishikura J , Sakamoto S, Okada M, Yamaguchi T:** Effect f YM928, a novel AMPA receptorantagonist, on seizures in EL mice and kainite-inducedseizures in rats. Naunyn schmiedebergs Arch Pharmacol 370: 99-105, 2004.

29. **Langan YM, Lucas R, Jewell H,Toublanc N, Schaefer H, Sander JW, Patsalos PN:** Talampanel, a new antiepileptic drug : single- and multi-dose pahrmacokinetics and initial 1-week experience in patients with chronic intractable epilepsy. Epilepsia 44: 46-53, 2003.

30. **Grossman SA, Ye X, Chamberlain MC, Mikkelsen T, Batchelor T, Desideri S, Piantadosi S, Fisher J, Fine HA:** Talampanel With Standard Radiation and Temozolomide in Patients With Newly Diagnosed Glioblastoma:A Multicenter Phase II Trial
J Clin Oncol 27: 4155–4161, 2009.